Development of high spatial resolution acquisition methods for diffusion MRI

Slimane Tounekti

N° d'ordre NNT : 2019LYSE1008

THESE de DOCTORAT DE L'UNIVERSITE DE LYON
opérée au sein de
l'Université Claude Bernard Lyon 1

Ecole Doctorale : **N° ED 476-NSCo**
Neurosciences et Cognition

Spécialité de doctorat : *Imagerie médicale*
Discipline : *Sciences et ingénierie pour la Santé*

Soutenue publiquement le 25/01/2019, par :
Slimane Tounekti

Développements des méthodes d'acquisition à haute résolution spatiale en IRM de diffusion

---

Development of high spatial resolution acquisition methods for diffusion MRI

Devant le jury composé de :

Canet-Soulas Emmanuelle,	PU, UCBL, Lyon	Présidente
Dhenain Marc,	DR, CNRS, Paris	Rapporteur
Tourdias Thomas,	PU-PH, Université de Bordeaux	Rapporteur
Caruyer Emmanuel,	CR, CNRS, Rennes	Examinateur
Ratiney Hélène,	CR, CNRS, Lyon	Examinatrice
Troalen Thomas,	PhD, Siemens Healthineers, Paris	Examinateur
Hiba Bassem,	CR, CNRS, Lyon	Directeur de thèse
Ben Hamed Suliann,	DR, CNRS, Lyon	Co-directrice de thèse
Lepetit-coiffe Matthieu,	PhD, Siemens Healthineers, Paris	Invité

Remerciements

Tout d'abord, je tiens à remercier vivement M. Marc DHENAIN et M. Thomas TOURDIAS d'avoir accepté d'examiner le présent manuscrit. Je tiens à remercier également Mme Emmanuelle CANET-SOULAS, Mme Hélène RATINEY, M. Emmanuel CARUYER, et M. Thomas TROALEN d'avoir accepté d'examiner et évaluer mes travaux de thèse. C'est un grand honneur de les compter comme membres de mon jury.

Je remercie chaleureusement mes directeurs de thèse M. Bassem HIBA d'avoir dirigé mes travaux de thèse et de m'avoir soutenu activement dans les développements méthodologiques de ce projet de thèse. Je tiens à remercier Mme Suliann BEN HAMED de m'avoir accepté dans son équipe et pour sa contribution précieuse dans les aspects neuroscientifiques de ce projet. Je vous remercie pour vos conseils, vos encouragements et pour les bons moments que nous avons partagé.

Je remercie également M. Franck LAMBERTON, Thomas TROALEN et Danielle Ibarrola de m'avoir permis de bénéficier de leurs expériences scientifiques en termes de physique de l'imagerie et de développement de séquences. Merci de m'avoir apporté votre soutien et vos conseils pendant ces trois ans de thèse.

Je tiens à remercier Yann BIHAN-POUDEC pour sa précieuse contribution à ce travail, pour son humour, son énergie inépuisable et son sourire. Merci Yann pour ton aide. Un grand merci à tous mes collègues : Mathilda FROESEL, Maeva GACOIN, Julie NOIRET, Manon DIRHEIMER, et Justine CELERY d'avoir participé et assuré le déroulement de toutes les acquisitions. Je remercie les membres du laboratoire, étudiants, post-doctorants, ingénieurs ou chercheurs, pour les rencontres, les discussions et les retours constructifs. Merci à tous mes amis

Merci à ma famille, mes parents, Saad et Aicha, mon frère Abbes, mes sœurs et en particulier mon cousin Lotfi pour son aide et son soutien durant ces dernière années.

A ma femme, merci de partager ma vie, de me soutenir, de m'aider, et d'être là pour moi.

A tous je dis Merci…

Abbreviations

3

3T *3 Tesla*

A

ACS *: auto-calibration signal*

AD *: Axial Diffusivity*

ADC *: Apparent Diffusion Coefficient*

B

BW *: Bandwidth*

C

CSF *: Cerebrospinal fluid*

D

dMRI *: Diffusion-weighted magnetic resonance imaging*

DTI : Diffusion Tensor Imaging

E

EF *: EPI-Factor*

EPI *: Echo Planar Imaging*

ES *: Echo Spacing*

ETL *: Echo Train Length*

F

FA *: Fractional Anisotropy*

FID *: Free Induction Decay*

FOV *: Field Of View*

G

GE *: Gradient Echo*

GM *: Grey Matter*

GRAPPA *: GeneRalized Autocalibrating Partially Parallel Acquisitions*

I

IR *: Inversion Recovery*

K

k-space *: Fourier Space*

M

MD *: Mean Diffusivity*

MR *: Magnetic Resonance*

MRI *: Magnetic Resonance Imaging*

N

NMR *: Nuclear Magnetic Resonance*

P

PGSE *: Pulsed Gradients Spin Echo*

R

RD *: Radial Diffusivity*

RF *: Radio Frequency*

rsEPI : readout-segmented EPI

S

SE *: Spin Echo*

SE-EPI *: Spin Echo-Planar Imaging*

SENSE *: sensitivity encoding*

T

TE *: echo time*

TR : repetition time

TSE *: Turbo Spin Echo*

U

UHF *: Ultra-High Field*

W

WM *: white matter*

Table of contents

List of Tables

List of Figures

Résumé

L'IRM de diffusion (IRMd) est l'unique technique non invasive qui permet l'exploration de la microstructure cérébrale. En plus d'une large utilisation pour les applications médicales, l'IRMd est aussi utilisée en neuroscience pour comprendre l'organisation et le fonctionnement du cerveau. Toutefois, sa faible résolution spatiale et sa sensibilité aux artéfacts limitent son utilisation chez le primate non humain.

L'objectif de cette étude est de développer une nouvelle approche qui permette d'acquérir des données d'IRMd à très haute résolution spatiale sur des cerveaux de macaques anesthésiés. Cette méthode est basée sur un balayage 3D de l'espace de Fourier avec un module de lecture d'Echo Planar-segmenté.

Cette méthode a été tout d'abord implémentée sur une machine IRM 3 Tesla (Prisma, Siemens), puis validée et optimisée *in-vitro* et *in-vivo*. Par rapport à la méthode d'acquisition classique, un gain de sensibilité de l'ordre de 3 pour la substance grise cérébrale et de 4.7 pour la substance blanche cérébrale a été obtenu grâce à la méthode développée.

Cette méthode a permis de réaliser l'IRMd du cerveau de Macaque avec une résolution spatiale isotrope de 0.5 mm jamais atteinte auparavant. L'intérêt de réaliser des données d'IRMd à une telle résolution pour visualiser et analyser *in-vivo* des structures fines non détectables avec la méthode d'acquisition classique comme les sous-champs de l'hippocampe ou encore la substance blanche superficielle, a été démontré dans cette étude. Des résultats préliminaires très encourageants ont également été obtenus chez l'homme.

Abstract

Diffusion MRI (dMRI) is the unique non-invasive technique that allows exploration of the cerebral microstructure. Besides being widely used for medical applications, dMRI is also employed in neuroscience to understand the brain's organization and connectivity. However, its low spatial resolution and its sensitivity to artifacts limit its application to non-human primates.

This work aims to develop a new approach that allows dMRI acquisition at very high spatial resolution on anesthetized macaque brains. This method is based on 3D sampling of Fourier space with a segmented Echo Planar Imaging readout module. This method was first implemented on a 3 Tesla MR scanner (Prisma, Siemens), validated and optimized *in-vitro* and *in-vivo*. Compared to the conventional acquisition method, a gain of sensitivity of 3 for cerebral grey matter and of 4.7 for white matter was obtained with the proposed approach.

This method allowed our research team to acquire dMRI data on the macaque brain with a spatial isotropic resolution of 0.5 mm, never reached before. This study also illustrates interest in acquiring dMRI data with such a spatial resolution to visualize and analyze *in-vivo* fine structures not detectable with the classical acquisition method, such as sub-fields of the hippocampus and superficial white matter. Finally, very encouraging preliminary results were also obtained in humans.

Introduction

This thesis was conducted at the Institut des Sciences Cognitives Marc Jeannerod, Lyon, France (UMR 5229 CNRS – Université Lyon 1) under the supervision of Dr. Bassem Hiba for the MRI methodological developments and under the co-direction of Dr. Suliann ben Hamed for the neuroscientific aspects. This project has benefited from co-financing and scientific support from Siemens Healthineers, France. All of the MR experiments were carried out using a 3 Tesla Prisma system (Siemens Healthineers, Erlangen, Germany) in "PRIMAGE-CERMEP - imagerie du vivant".

Scientific context:

Diffusion-weighted magnetic resonance imaging (dMRI) is based on the measurement of water molecule diffusion inside biological tissue to probe its underlying structures. Indeed, the measurement of the water molecule pathway provides information about the structure of the surrounding microscopic environment. Based on this principle, dMRI produces images with contrast depending on water molecule diffusivity. The great success of this approach comes from its ability to non-invasively describe the organization of the underlying microstructure tissue by quantifying the diffusion anisotropy, e.g., the brain white matter.

More than thirty years have passed since the first *in-vivo* dMRI acquisition on the *in-vivo* human brain was performed (Le Bihan et al., 1986) using the gold standard Stejskal et al. pulse sequence (Stejskal and Tanner, 1965). In the last two decades, advanced acquisition schemes such as the diffusion tensor (Basser et al., 1994; Basser and Pierpaoli, 1998; Pierpaoli and Basser, 1996) have been introduced and used in many applications.

Therefore, interest in the scientific community in dMRI has grown due to its success in clinical applications (e.g., brain lesion, stroke and tumor detection) and neurosciences applications such as study of the normal and pathological states of the central nervous system, as well as for understanding the brain's complex anatomical architecture and connectivity network (Basser et al., 2000; Pajevic and Pierpaoli, 2000).

However, dMRI suffers from several drawbacks. First, dMRI is known for its inherently low signal-to-noise ratio (SNR) due to the low sensitivity of Magnetic Resonance Imaging (MRI) and to the weighting of the magnetic resonance signal by the water molecules diffusivity. Second,

therefore, *in-vivo* cerebral dMRI is usually carried out with relatively low spatial resolution, e.g., 1.2 mm and 2 mm, respectively, for macaque and human scans. To overcome these issues, there are mainly two ways: 1) the use of appropriate materials (more sensitive magnetic resonance coils and/or the use of a high magnetic field (e.g., 3 Tesla, 7 Tesla, etc.); 2) the use of high-sensitivity dMRI pulse sequences.

The other limitation of dMRI is its high sensitivity to subject motion. Even microscopic physiologic motion, such as that induced by cardiac pulsation, can be amplified in the presence of high diffusion-sensitizing gradients. This induces non-linear phase variation of the received signal, resulting in ghosting artifacts in the final images (Chang et al., 2015a; Miller and Pauly, 2003; Ordidge et al., 1994). This sensitivity is exacerbated when high-resolution dMRI data are required.

Aim

The main purpose of this work is to develop and validate a dMRI methods based on a dMRI pulse sequence with a three-dimensional Echo Planar Imaging (3D-EPI) module of Fourier-space sampling for human and non-human primate applications. The goal of this development is to provide an acquisition strategy that allows us to improve the spatial resolution and the quality of dMRI data acquired from the *in-vivo* brain using a standard clinical MR scanner e.g., 3 Tesla. The specifications of the desired pulse sequences can be summarized in the following points:

- The ability to improve the SNR of *in-vivo* dMRI acquisition on human and monkey brains.
- The ability to achieve high-quality cerebral dMRI data with a significantly higher isotropic spatial resolution compared to the standard resolution reported in the literature.
- The ability to maintain the non-invasive aspect of the dMRI acquisition.

Manuscript introduction

This manuscript provides a detailed description of the methodological developments carried out during this thesis research. It is divided into four chapters in order to emphasize the state-of-the-art, this study's major findings and the advancements it contributes to the field.

Chapter 1 provides a description of the basic principles of nuclear magnetic resonance (NMR) at the microscopic and macroscopic levels and explains the mechanisms of the spatial encoding of the MR signal for imaging, so-called magnetic resonance imaging (MRI). In addition, it presents

the basic pulse sequences routinely used. The second part of this chapter focuses on molecular diffusion physics and reviews the fundamental pulse sequences and acquisition strategies, as well as the main applications of dMRI.

Chapter 2 begins with a presentation of the overall context of this work and highlights the major challenges that need to be addressed. Then, it reviews the main methodological developments performed in order to improve the spatial resolution of dMRI acquisition in human and macaque brains. Therefore, this section points out the specificity of different studies and the significant achievements that were demonstrated. Finally, an overview of the main objectives of this study was described at the end.

Chapter 3 is divided into two sections. The first section presents the description of the EPI pulse sequence and discusses its limits specifically when it is used for dMRI scans. Then, the second section demonstrates the developments realized as follows:

- Description of the pulse sequences development.
- Optimization of the experimental protocol for human and macaque examination.
- Illustration of the obtained results, and demonstrating the added value of the developed method on the *in-vivo* macaque brain.
- Illustration of the preliminary results obtained on the human brain.

Finally, Chapter 4 is the original research article our team published in the journal *NeuroImage* in 2018 (Tounekti et al., 2018). This paper presents an experimental study performed on four *anesthetized* macaque monkey brains in order to illustrate the validity of the proposed acquisition pulse sequence to achieve high spatial resolution and high SNR dMRI data.

This study has shown that, in comparison with the conventional acquisition method, a gain of sensitivity of 3 for cerebral grey matter and of 4.7 for white matter was obtained with the proposed approach. This method allowed us to acquire dMRI data on the macaque brain with a spatial isotropic resolution of 0.5 mm, never reached before. Interest in acquiring dMRI data with such a spatial resolution, to visualize and analyze *in-vivo* fine structures not detectable with the classical acquisition method, such as the subfields of the hippocampus and superficial white matter, was demonstrated in this experimental study. The benefits of high-resolution dMRI to improve tractography results were also illustrated here.

Chapter I. MR Imaging Basics and dMRI

Introduction

In nature, all atoms are made up of electrons and nuclei. The electrons are charged negatively, whereas the nucleus has a net positive charge and contains protons and neutrons. In addition, the nucleus is characterized by its intrinsic spin angular momentum, which depends on the number of protons and neutrons.

Nuclear Magnetic Resonance (NMR) is the study of the magnetic properties of nuclei and it is based upon the interaction between nuclei and an external magnetic field at their resonance frequency.

Nuclear Magnetic Resonance

I.1. Description

Atomic nuclei are characterized by a nuclear spin quantum number, *I*. *I* can be zero, half-integral values (any multiple of ½), and integral values (e.g., 1, 2, 3). Basically, *I* depends on atomic mass and the charge number of particles. For nuclei with an odd mass number such as ^{1}H, ^{13}C, and ^{15}N, *I* is half-integral (1/2, 3/2, 5/2, etc.). Whereas, for nuclei with an even mass number and an odd charge number such as ^{2}H and ^{14}N, *I* has an integer value (1, 2, 3, etc.). Finally, for nuclei with both an even mass number and an even charge number, *I* is zero (e.g., ^{12}C, ^{16}O, and ^{32}S).

The hydrogen (^{1}H) nucleus consists of a single proton and it contributes mainly to the NMR signal for two reasons. First, the ^{1}H nucleus possesses a non-zero spin number (spin=½). Second, it is highly represented in biological tissues, >70%. Table I.1 provides an extensive list of commonly used nuclei and their characteristics at a magnetic field of 3 Tesla (3T).

An elementary proton has a spin (I≠0) in self-rotation about an axis at a distance r with a constant linear speed $\mathbb{v}$ and induces an angular momentum $\vec{L}$, according to the following expression (Fig.I.1):

$$\vec{L} = m\,\vec{\mathbb{v}}\,\vec{r} \qquad (1.1)$$

Where m is the particle mass.

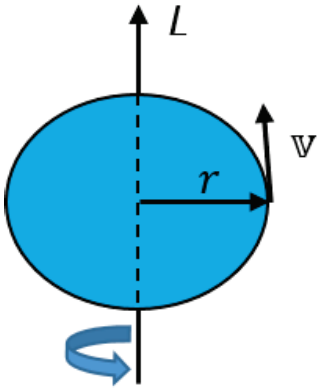

Figure I.1: An elementary proton is in self-rotation about an axis at a distance r with a constant linear speed $\mathbb{V}$ and induces in angular momentum L.

In addition, the proton has a positive charge q. This induces a local magnetic field, known as the magnetic moment $\vec{\mu}$ oriented parallel to the axis of rotation (Fig.I.2). Therefore, a proton acts as a tiny bar magnet oriented along the rotation axis.

$$\vec{\mu} = \vec{s}.I \tag{1.2}$$

where $\vec{s}$ is the apparent surface and I is the current magnitude.

$$\vec{\mu} = \frac{q\,\vec{\mathbb{V}}\vec{r}}{2} \tag{1.3}$$

The magnetic moment $\vec{\mu}$ can be expressed as a function of $\vec{L}$ according to the Einstein-de Haas effect, and Equation 1.3 can be written as follows:

$$\vec{\mu} = \gamma.\vec{L} = \frac{q}{2m}\vec{L} \tag{1.4}$$

where γ is the gyromagnetic ratio which depends on the nucleus (Table.I.1).

nucleus	*spin*	*gyromagnetic ratio [MHz T^{-1}]*	*Larmor frequency [MHz]*
^{1}H	1/2	42.5774	127.72
^{2}H	1	6.53896	19.06
^{15}N	1/2	4.3173	12.95
^{13}C	1/2	10.7084	32.125
^{31}P	1/2	17.2514	51.754

Table I.1: Constants for Selected Nuclei of Biological Interest

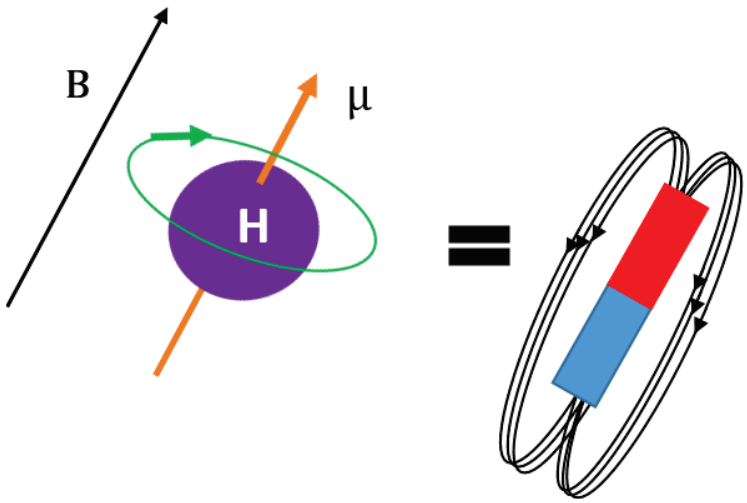

Figure I.2: A hydrogen atom rotates around itself and around an axis. It produces a local magnetic field characterized by its moment $\vec{\mu}$ oriented parallel to the axis of rotation.

In biological tissues containing hydrogen atoms, each proton has a spin vector equal in magnitude; however, the spin vectors of the set of protons are randomly oriented. The sum of all the elementary spin vectors is zero. Hence, there is no magnetization in biological tissue (Fig.I.3).

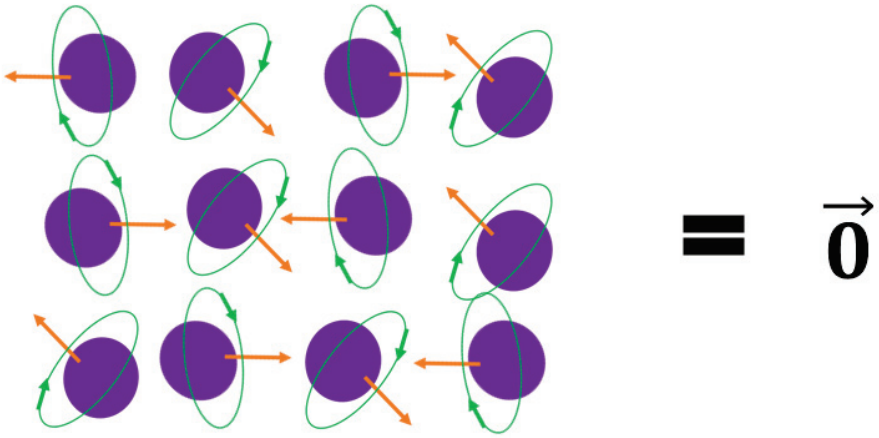

Figure I.3: In the absence of an external magnetic field, the spin vectors of protons are oriented randomly. The vector sum of these spin vectors is zero.

However, in the presence of an external powerful magnetic field $\overrightarrow{B_0}$, the spins are oriented parallel to $\overrightarrow{B_0}$ and precess with a constant rate characterized by its Larmor frequency (υ_0), which is directly proportional to the amplitude of the main magnetic field $\overrightarrow{B_0}$ and the gyromagnetic ratio γ, and it is expressed according to the following equations:

$$\omega_0 = \gamma . B_0 \tag{1.5}$$

and

$$\upsilon_0 = \left(\frac{\gamma}{2\pi}\right) B_0 \tag{1.6}$$

Where ω_0 (in rad.s^{-1}) is the angular frequency, $\upsilon_0 = (\omega_0/2\pi)$ in Hz, for the hydrogen nucleus, the Larmor frequency at magnetic field of 3 Tesla is υ_0= 127.72 MHz (Table I.1).

Under $\overrightarrow{B_0}$, the particles are divided into two energy levels (Fig.I.4):

- Low-energy spins (spin-down) rotate around the main axis of the magnetic field within a cone in the orientation imposed by $\overrightarrow{B_0}$.
- High-energy spins (spin-up), also named anti-parallel spins, are oriented in the opposite direction of $\overrightarrow{B_0}$.

The energy difference, ΔE, between the two states is given by the following equation:

$$\Delta E = h\left(\frac{\gamma}{2\pi}\right) B_0 = h\upsilon_0 \qquad (1.7)$$

The number of the low-energy spins is slightly higher than that of high-energy spins. The ratio of high-energy spins to low-energy spins is governed by a distribution known as the Boltzmann distribution:

$$\frac{N^{up}}{N^{down}} = e^{-\frac{\Delta E}{kT}} \qquad (1.8)$$

where N^{up} and N^{down} are respectively the number of antiparallel and parallel spins, k is the Boltzmann constant, k = 1.38 10^{-23} J/K and T is the temperature in Kelvin.

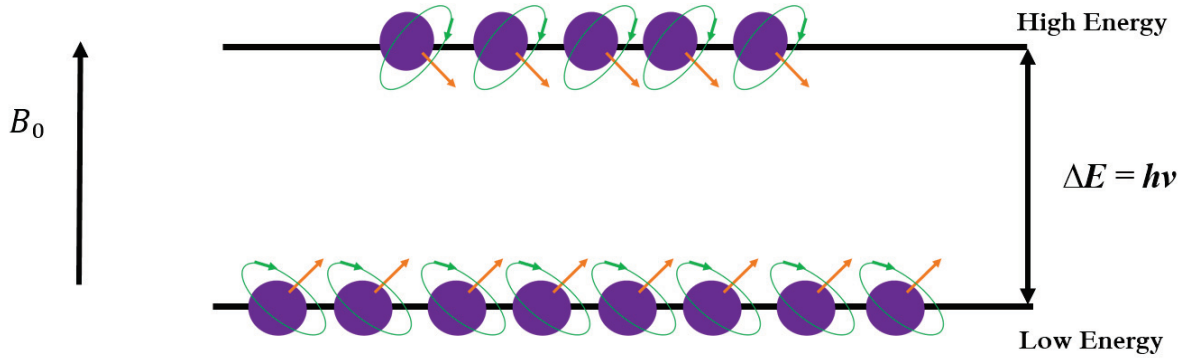

Figure I.4: The particles are divided into two energy levels as a function of the external magnetic field strength B_0. The low energy level corresponds to spins parallel with B_0, while spins in the higher energy level have an antiparallel alignment with B_0. The energy level difference between the two spin states can be calculated through the equation $\Delta E = h\upsilon_0$.

I.2. Macroscopic magnetization

The spins placed in a strong external magnetic field precess around the magnetic field vector with the Larmor frequency υ_0, whereas the axis of rotation is oriented of the z direction of the conventional Cartesian coordinate system. The magnetic moment $\vec{\mu}$ consists in a longitudinal component or the amplitude $\vec{\mu_z}$ (along the z-axis) parallel to $\vec{B_0}$ and constant in time, and a nonzero perpendicular or transverse component $\vec{\mu_{xy}}$ (in the (x, y) plane) which varies in time as the proton precesses (Figure I.5).

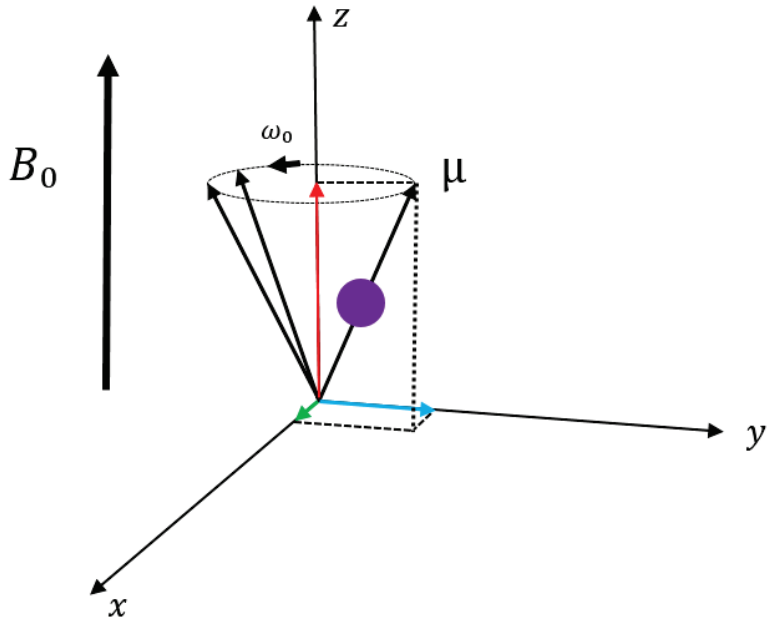

Figure I.5: Under an external magnetic field, a proton precesses about the magnetic field with an angular frequency ω_0. The longitudinal component or the amplitude of the spin magnetic moment $\vec{\mu}$ (projection onto the z axis: red arrow) is constant in time. However, the x (green arrow) and y (blue arrow) components change in time due to the precession motion.

In a macroscopic ensemble of nuclei, according to the Boltzmann distribution equation (1.8), the spins are distributed into two possible states: parallel and anti-parallel spins. The difference between the two energy levels, ΔE, creates a non-zero macroscopic magnetization $\overrightarrow{M_0}$, which is the sum of all the individual magnetic moments. Similarly to the behavior of the magnetic moment $\vec{\mu}$, the resulting net magnetization is composed of two components, the longitudinal component $\overrightarrow{M_z}$ which is parallel to $\overrightarrow{B_0}$ and the transversal component $\overrightarrow{M_{xy}}$ perpendicular to $\overrightarrow{B_0}$. At the equilibrium state, the transversal is infinitely small compared to the longitudinal component $\overrightarrow{M_{xy}} \approx \vec{0}$, whereas the net magnetization $\overrightarrow{M_z} = \overrightarrow{M_0}$ depends on the strength of the external field $\overrightarrow{B_0}$ and on the temperature T and is given by the following equation:

$$\overrightarrow{M_0} = \sum \overrightarrow{\mu_i} = \frac{N.\gamma^2 h^2 \overrightarrow{B_0}}{4KT} \qquad (1.9)$$

where N is the total number of spins, k is the Boltzmann constant and h is the Planck constant.

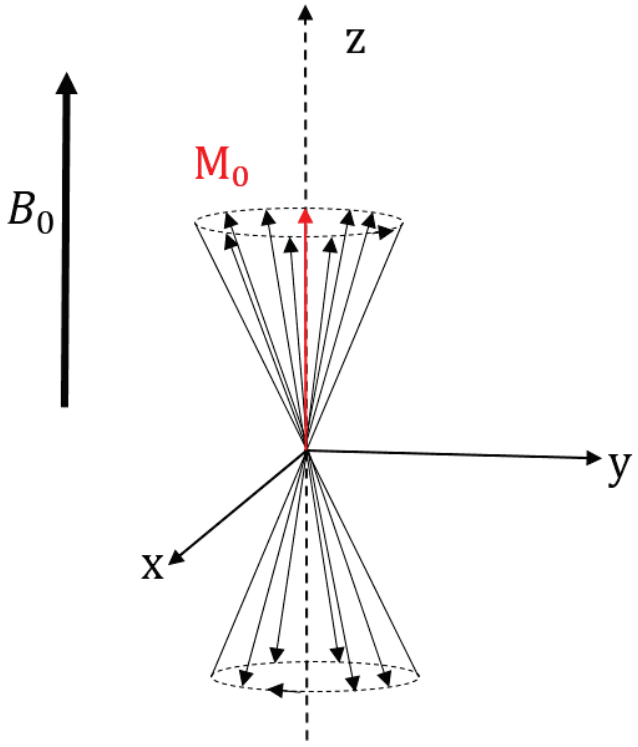

Figure I.6: In an ensemble of nuclei exposed to a strong magnetic field, the ½ spins are distributed according to the Boltzmann distribution into low-energy spins, also called also parallel, and high-energy spins, or anti-parallel spins. The difference between the two energy levels, ΔE, creates a non-zero m magnetization M_0, which is the sum of all the individual magnetic moments

I.3. Radio frequency excitation pulse

At the equilibrium state, it is impossible to measure the vector $\overrightarrow{M_0}$ because it is infinitely small compared to $\overrightarrow{B_0}$. However, the net magnetization $\overrightarrow{M_0}$ can be measured only in the perpendicular to z-direction. Indeed, an external oscillating electromagnetic magnetic field $\overrightarrow{B_1}$ with an angular frequency $\omega_1 = \omega_0$ and orthogonal to the main field, also called the radiofrequency pulse (RF pulse), is applied. This allows the spins to absorb energy and move from the low-energy state towards the higher. In the presence of $\overrightarrow{B_1}$, the individual magnetic moments $\vec{\mu}$ experience a torque:

$$\frac{d\vec{\mu}}{dt} = \gamma\,\vec{\mu} \times \overrightarrow{B_1} \qquad (1.10)$$

Therefore, the net magnetization $\vec{M}$ is disrupted from equilibrium, and it is flipped away from $\overrightarrow{B_0}$ with an angle θ which is proportional to the duration τ of the applied RF pulse (Fig.I.7).

$$\theta = \gamma . \tau . B_1 \qquad (1.11)$$

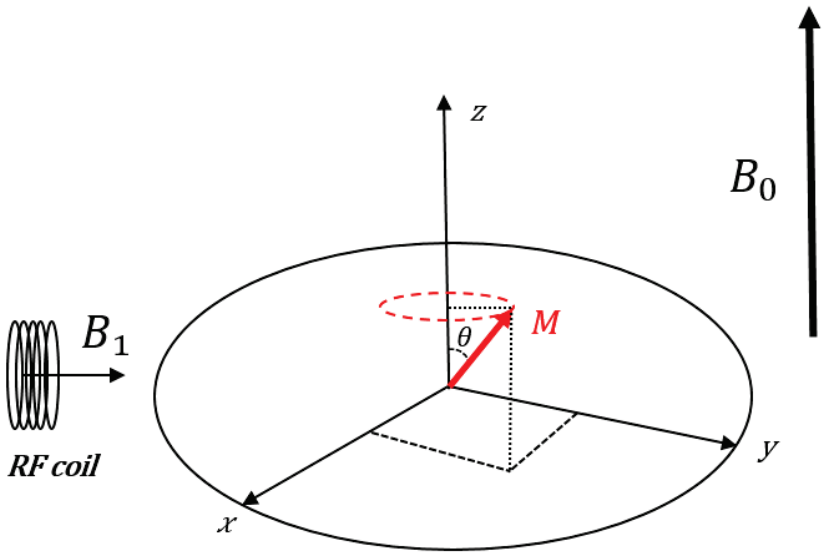

Figure I.7: During the application of the RF pulse, the net magnetization M is flipped away from B_0 with an angle θ which is proportional to the duration τ of the applied RF pulse.

In clinical Magnetic Resonance Imaging (MRI), the RF pulses of 90° and 180° are the most widely used specifically for diffusion-weighting MRI (presented below). The 90° RF pulse brings the magnetization to the transverse plane $\overrightarrow{M_{xy}} = \vec{M}$, and would zero out the longitudinal component $\overrightarrow{M_z} = \vec{0}$. However, the RF pulse of 180° completely inverts the longitudinal component of the net magnetization $\overrightarrow{M_z} = - \overrightarrow{M_z}$.

I.4. Relaxation

As described above, the RF pulse moves the spins away from equilibrium to an excited state (high energy level). Therefore, the excited spins are aligned in the transverse plane in the desired

direction. Once the radiofrequency pulse is turned off, the spins go back to an equilibrium magnetization state, and lose their coherence due to tiny differences in the local magnetic field. The evolution of the net magnetization after the RF excitation, with precession around $\overrightarrow{B_0}$, results in longitudinal and transverse relaxations shown in Figure I.8.

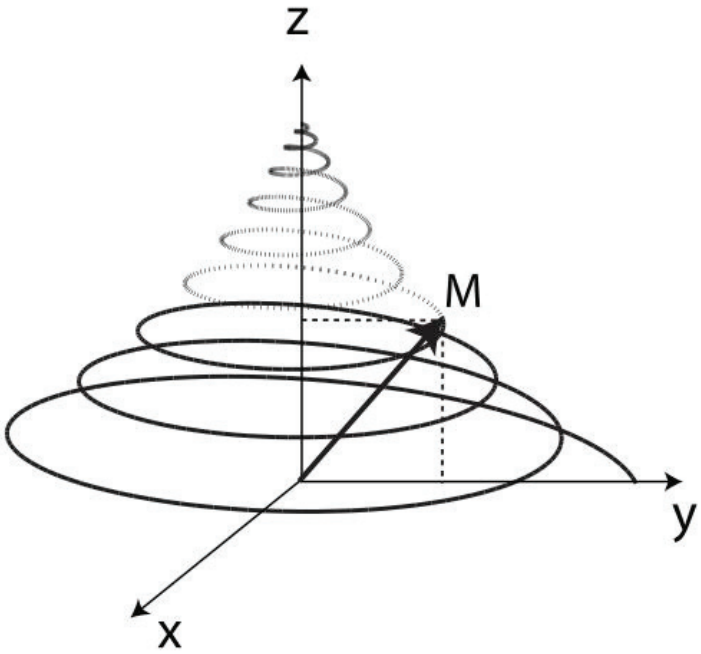

Figure I.8: The RF pulse flips the magnetization to the transverse plane of an angle θ (e.g., 90 degree). Once the radiofrequency pulse is turned off, the spin system eventually goes back to its thermal equilibrium magnetization. This phenomenon is called the relaxation (from Mayure Narsude, 2014).

I.4.1. Longitudinal relaxation

Longitudinal relaxation is characterized by the energy exchange between protons and the surrounding molecules. The evolution of the longitudinal magnetization after an RF pulse is exponential, and it can be expressed by the following equation:

$$\frac{dM_z}{dt} = \frac{M_0 - M_z}{T_1} \qquad (1.12)$$

The relaxation time (T1), also named spin-lattice relaxation, is a time constant needed for the longitudinal magnetization to recover 63% of its equilibrium value. The longitudinal component is considered to be completely restored after 5 T1. The solution of Equation 1.12 is found by integration

$$M_z(t) = M_0 - [\, M_0 - M_0(0)]e^{(-\frac{t}{T_1})} \qquad (1.13)$$

where $M_0\,(0)$ is the longitudinal magnetization right after the RF excitation at t=0. After an RF pulse of 90° $M_0\,(0) = 0$, hence Equation 1.13 can be written as follows:

$$M_z(t) = M_0\,(1 - e^{(-\frac{t}{T_1})}) \qquad (1.14)$$

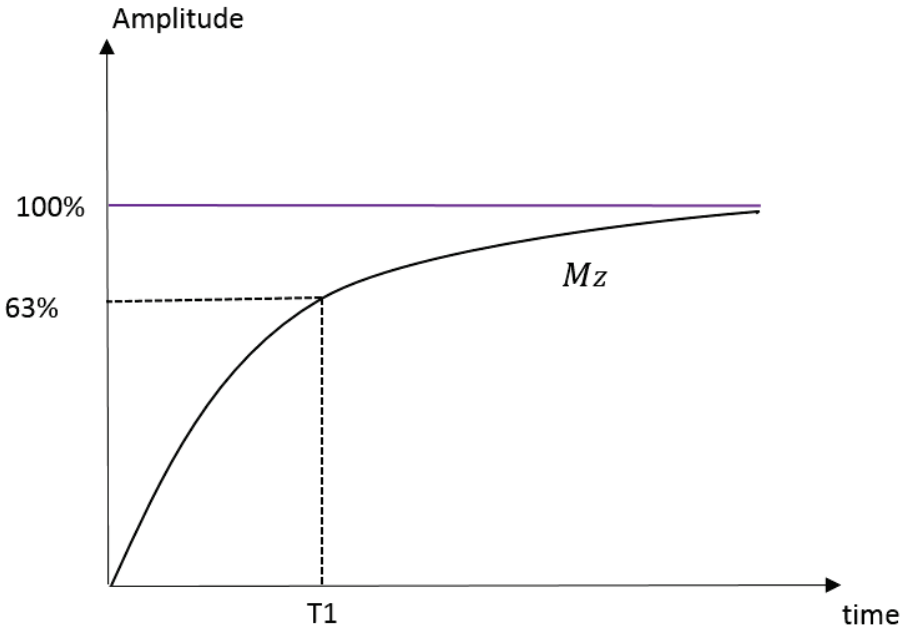

Figure I.9: The restoration of the longitudinal magnetization after the RF pulse of an angle (90 degrees) is characterized by the T1 relaxation time.

I.4.2. Transversal relaxation

Let us consider the transverse component $\overrightarrow{M_T}$ of the magnetization, which describes the magnetization in the transverse plane. After the application of the RF excitation pulse, simultaneously with the $\overrightarrow{M_z}$ recovery characterized by T1 time, the transverse magnetization ($\overrightarrow{M_T}$) gradually decreases due to the spins dephasing by the presence of local magnetic field inhomogeneities. This effect is also known as spin-spin relaxation, which is characterized by the constant time T_2. Indeed, T_2 refers to the time constant needed for the transversal component to lose 63% of its value after the application of the RF pulse. Then, the transversal component is modeled by an exponential function and can be written by the equation:

$$\overrightarrow{M_T} = \overrightarrow{M_x} + \overrightarrow{M_y} = \overrightarrow{M_0}\, e^{\left(-\frac{t}{T_2}\right)} \qquad (1.15)$$

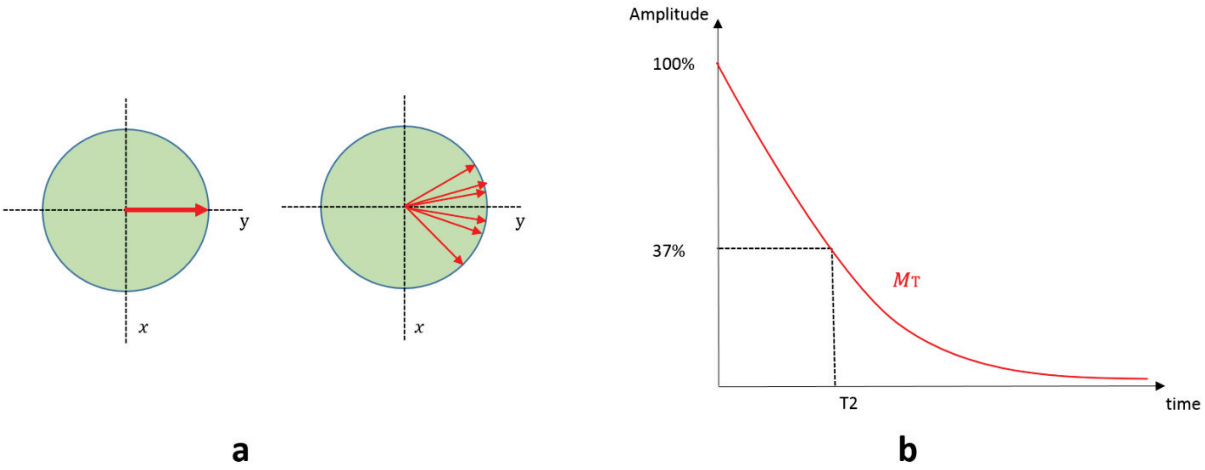

Figure I.10: After the RF excitation pulse, the spins precess at different frequencies, centered around the Larmor frequency, inducing the dephase of spins (a) and the gradual decrease of the transversal magnetization $\overrightarrow{M_T}$ (b).

In the presence of macroscopic field inhomogeneities, the spins precess with different frequencies. Therefore, the spins system dephase quickly, resulting in a gradual decrease of the transversal magnetization $\overrightarrow{M_T}$ with a time slightly different from the theoretical T_2, named T_2^*. If we denote the contribution of this macroscopic magnetic field inhomogeneity as $T_2^{'}$, then the relation between the relaxation T_2 and T_2^* can be written as:

$$\frac{1}{T_2^*} = \frac{1}{T_2} + \frac{1}{T_2^{'}} \qquad (1.16)$$

Therefore, the relation 1.15 can be written as:

$$\overrightarrow{M_T} = \overrightarrow{M_0}\, e^{\left(-\frac{t}{T_2^*}\right)} \tag{1.17}$$

In our bodies, the different biological tissues are characterized by different relaxation times T_1 and T_2, which are basically used to generate contrast in MR images. Table I.2 shows the T_1 and T_2 values of various tissues measured at 3 T (Gold et al., 2004; Wansapura et al., 1999).

Tissue	T1 (ms)	T2 (ms)
White matter	832	80
Grey matter	1331	110
Muscles	1420	35
CSF	4136	2200
Fat	370	133

Table I.2: The time constants T1 and T2 (ms) values in different biological tissues.

Magnetic Resonance Imaging

Magnetic resonance imaging aims to measure the magnetic resonance (MR) signal of spins and generates images with different contrasts (e.g., T1, T2, diffusion-weighted). As explained above, after the application of the RF pulse, the transversal magnetization decreases exponentially and precesses around $\overrightarrow{B_0}$, thus inducing a current in the reception coil, which decreases exponentially. The measured MR signal represents the average value of transversal components for the entire sample. In order to spatially localize the MR signal since the Larmor frequency depends on the magnetic field, some magnetic field gradients are applied temporarily along the different axes (x, y and z), also called gradient pulses.

I.5. Spatial encoding

As demonstrated above in Equations 1.5 and 1.6, the Larmor frequency of the spin depends on the external magnetic field $\overrightarrow{B_0}$. The raw signal acquired using the coil cannot provide spatial

information about the origin of the signal. Therefore, in routine examinations, additional gradient pulses are applied along the z-axis (G_z), x-axis (G_x) and y-axis (G_y) to spatially select the desired region in order to localize the signal in the 2-dimensional plane.

I.5.1. Slice selection

A gradient pulse called the slice selection gradient (G_z) is applied along the z-direction in conjunction with a frequency-selective RF pulse, so that the exact magnetic field along the z-axis is given by:

$$\overrightarrow{B_z} = (B_{0_z} + G_{z_z})\,\vec{z} \tag{1.18}$$

where G_z is the gradient strength. Therefore, the Larmor frequency varies along this direction according to the following equation:

$$\omega_Z = \gamma(B_{0_z} + G_{z_z}) \tag{1.19}$$

To excite just a subset of the frequencies at this direction, a frequency-selective RF pulse is used. It affects only the frequency within a narrow range of frequencies $\Delta\omega$, named bandwidth (BW). In addition, the RF pulse is characterized by its central frequency, which determines the particular location excited when the slice selection gradient is turned on.

$$\Delta\omega = \gamma G_z \Delta_z \tag{1.20}$$

where Δz, the slice thickness, depends on the gradient pulse strength as well as the bandwidth of the RF pulse. In multi-slice imaging, widely used in MRI examination, various slices can be selected using the same RF pulse and with the same G_z gradient strength, but with a different central frequency.

During excitation, the precession frequencies of the spins vary across the selected slice due to the slice-selection gradient Gz, inducing phase differences accumulation besides the intended Gz-effect. To avoid resulting signal loss, the selected spins sample should be “re-phased” using a slice-refocusing gradient. Assuming that the Gz has a rectangular shape and is characterized by amplitude (A) and a duration (τ), the slice-refocusing gradient lobe has the same amplitude but with opposite polarity compared to Gz as well as half the duration ($\tau/2$) (Fig.I.12).

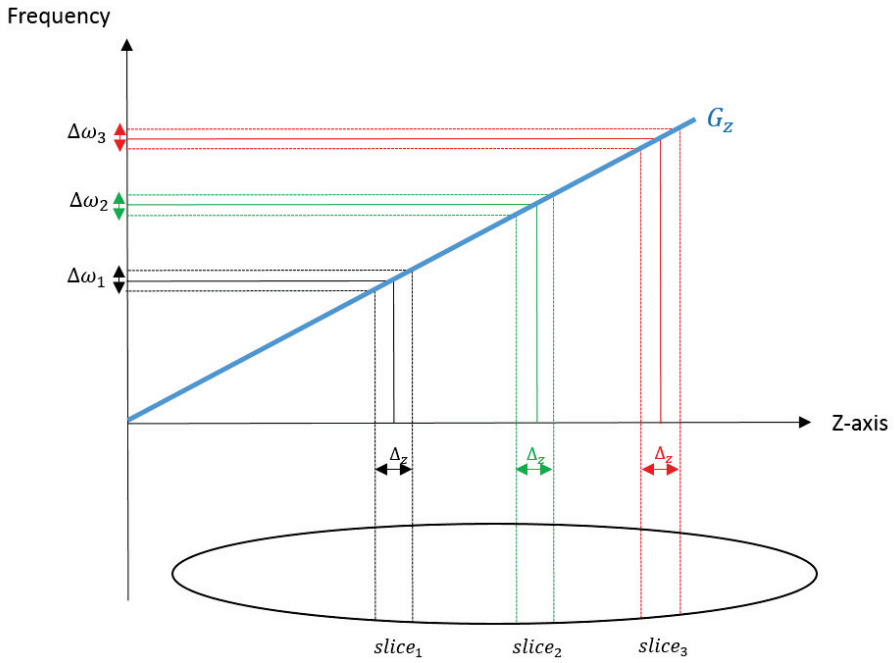

Figure I.11: The Gz gradient creates a linear variation of the Larmor frequency along the z-axis. Then, the slice thickness Δz can be selected using the frequency-selective RF pulse, which affects only the frequency within its bandwidth Δω.

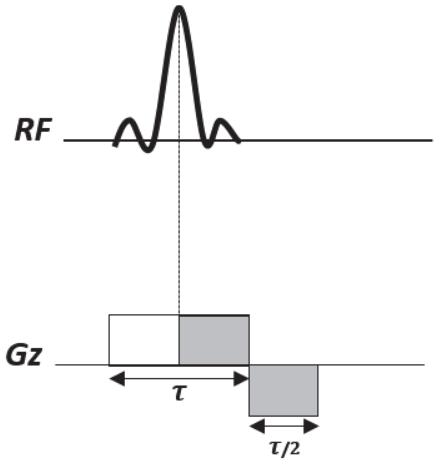

Figure I.12: To avoid signal loss induced by the accumulation of phase differences, the selected slice should be "re-phased" using a slice-refocusing gradient with opposite polarity compared to Gz as well as half the duration (τ/2).

I.5.2. Frequency encoding

The frequency encoding or the readout is the MR signal detection using a second gradient pulse G_x which is applied in the x-direction and is perpendicular to G_z. The application of the readout gradient pulse G_x induces a frequency precession variation along the axis in accordance with Equation 1.20. The position of the spin can be determined through the detected frequency and the gradient pulse magnitude. Actually, the gradient pulse amplitude is proportional to the total Field Of View in the readout direction (FOV_{RO}). The total range of frequencies, also known as receiver bandwidth ($\Delta\omega_{RO}$) is determined according to Equation 1.21. Therefore, the frequency resolution called bandwidth per pixel can be expressed as shown in Equation 1.22:

$$\omega_x = \gamma(B_{0_x} + G_x x) \tag{1.20}$$

$$\Delta\omega_{RO} = \gamma * G_{RO} * \Delta_{FOV_{RO}} \tag{1.21}$$

$$\Delta\omega_{pp} = \frac{\Delta\omega_{RO}}{N_P} \tag{1.22}$$

where N_P is the total number of sample points in the readout direction. In addition, the spatial resolution (pixel width $\Delta\eta$) in the readout direction can be calculated using the following relationship:

$$\Delta\eta = \frac{FOV_{RO}}{N_P} \tag{1.23}$$

Under the Gx gradient, the signal received in coil can expressed as:

$$s(t) = \int_x p(x) e^{-i\gamma G_x \Delta_x x} dx \tag{1.24}$$

The $p\ (x)$ is the spin densities on the readout direction and Δx is the duration of the Gx gradient pulse.

I.5.3. Phase encoding

The phase encoding gradient G_y is applied along the y-axis and is perpendicular to the x- and z-axes. As presented above, the spins in the selected slice precess at the Larmor frequency ω_0. The G_y gradient pulse is turned on after the RF excitation pulse and the slice selection gradient but

before the readout gradient. In the presence of G_y, the precession frequency of spins is temporarily increased or decreased according to the following equation:

$$\omega_y = \gamma(B_{0_y} + G_y y) \tag{1.25}$$

Once the G_y gradient is turned off, the spins return to their base frequencies ω_0 but ahead or behind in phase relative to their initial phase state prior to the application of the G_y gradient. This leads to a linear phase shift along the y-direction, and the frequency is y-position dependent: this is the phase encoding. The phase shift ($\Delta\varphi$) of the proton depends actually on the spin location, the amplitude (G_y) and the duration (δ_y) of the gradient pulse. Thereby, the spins from different positions in the y-axis are subject to the same G_y gradient pulse; they will experience a different amount of phase shift. This is can expressed mathematically as follows:

$$\Delta\varphi = \gamma * G_y * \delta_y * y \tag{1.26}$$

This can also be expressed as the mathematical description of the acquired signal which can be written as:

$$\mathrm{s(t)} = \int_y \int_x p(x,y) e^{-i\gamma(G_x \Delta_x x + G_y \delta_y y)} dx\, dy \tag{1.27}$$

For MRI experience, the sequence looping consists of repeating the RF pulse excitation, slice selection gradient pulse and MR signal detection with different amplitude of the G_y gradient pulse. For a selected slice, the phase and frequency encoding are repeated until the acquisition of the entire points and phase position (lines) in the frequency space, also called Fourier space (k-space).

I.5.4. 3D-imaging

As described above for the 2D sampling of k-space, only the desired slice is excited among the volume of interest using the slice-selection RF pulse, whereas, in the 3D sampling scheme, the whole volume, also called the "slab", is excited using slab-selection RF pulse. Often, a gradient pulse is applied in the z-axis simultaneously with the RF pulse. In addition to the frequency and phase-encoding of data presented above, the data are encoded in the z-dimension using a second phase-encoding gradient pulse applied along the z-axis. After each RF excitation pulse, the gradient pulse is applied to select at each time a specific slice, so-called "partition". Basically, the 3D-MRI

is typically used to improve the overall SNR of the MR data. This allows improvement of the reached spatial resolution along the three axes (x, y, and z).

The resulting MR signal in 3D MRI can be writing as follows:

$$s(t) = \int_z \int_y \int_x p(x,y,z) e^{-i\gamma\left(G_x \Delta_x x + G_y \delta_y y + G_z \beta_z z\right)} dx\, dy\, dz \qquad (1.28)$$

where β_z is the duration of the applied the gradient pulse Gz along the z-axis.

I.5.5. K-space

For each slice, the acquired data required for MR image reconstruction are contained within a data matrix, called k-space. The maximum of the signal corresponding to low frequencies is focused on the k-space center portion, determining overall image contrast, brightness and general shape. The outer portion of the k-space contains the high frequencies information, providing mainly the edge definition and details. The data in the k-space are displayed on a two-dimensional rectangular grid with principal axes k_x and k_y.

$$k_x = \gamma G_x \tau \qquad (1.29)$$

The k_x-axis represents the frequency information along the x-direction of the image, and the k_y-axis contains the phase component along the y-direction. Actually, each k-space point is influenced by the combination of the readout and the phase encoding gradient. Hence, each cell of the k-space (k_x, k_y) represents the frequency and phase information of each pixel in the reconstructed image. The relationship between each k-space point and the readout and phase gradient pulses is given by the following equation:

$$k_y = \gamma G_y \delta \qquad (1.30)$$

where τ and δ are respectively the duration of the application of the frequency and phase gradient pulses. On the other hand, the distance between two respective points in the k_x-axis (Δx) and two successive lines in the k_y-axis (Δy) is inversely related to the FOV of the reconstructed image through the following equations:

$$\Delta k_x = \frac{1}{FOV_{RO}} \qquad (1.31)$$

$$\Delta k_y = \frac{1}{FOV_y} \qquad (1.32)$$

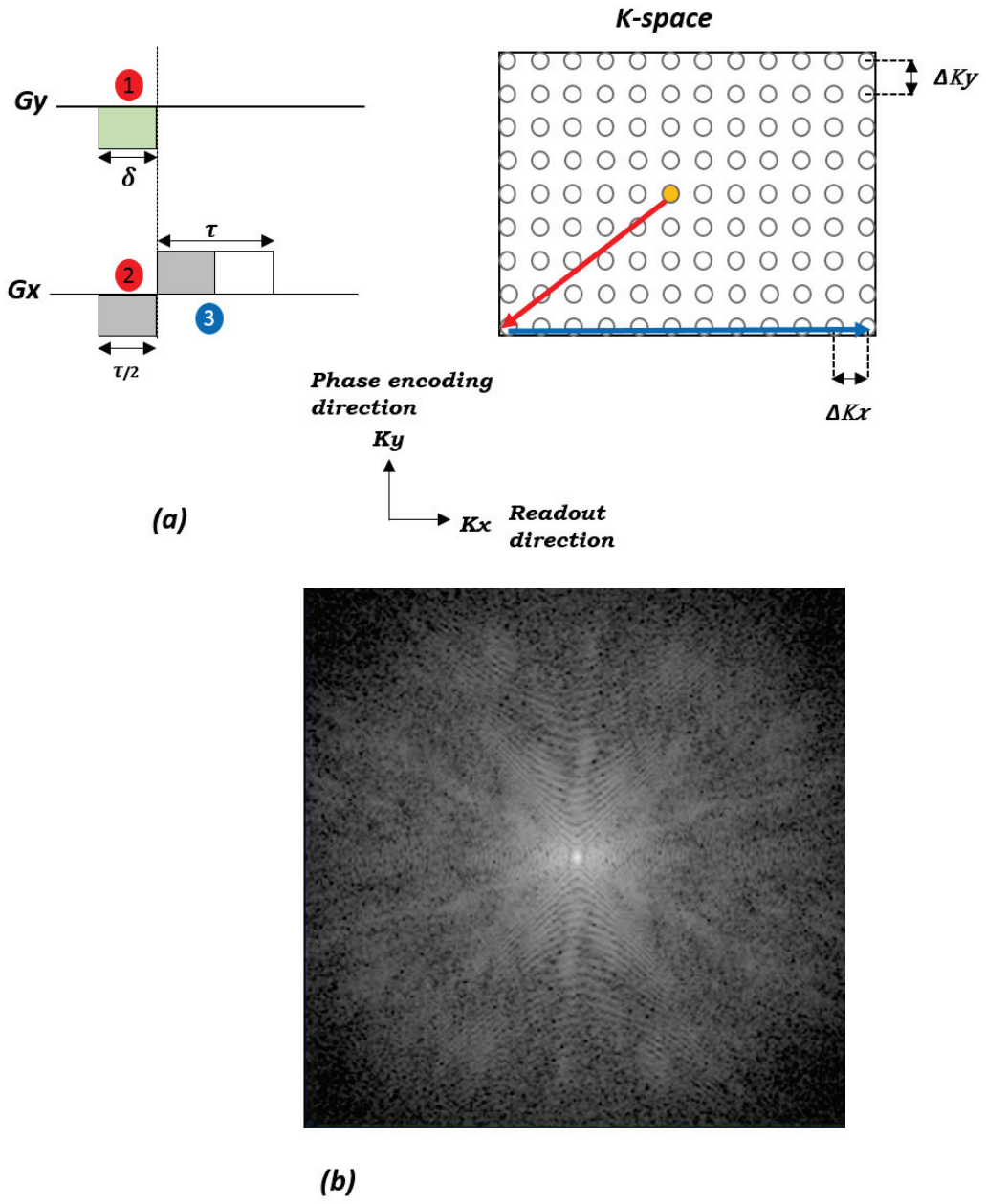

Figure I.13: The Cartesian k-space sampling: (a) the phase encoding gradients pulse allows the displacement between the k-space lines and decides which k-space line to be sampled (1). The pre-phasing gradient (number 2) shifts the sampling position to the edge of the k-space. The red arrow at the right presents the displacement results from the two gradients (1 and 2). The readout gradient (3) samples the k-space point in the x-direction (blue arrow). (b) Example of a fully sampled k-space.

The acquired MR signal is then digitized and used for sampling point-to-point the k-space. The frequency- and phase-encoding gradients allow travelling in the k-space and filling each cell with different complex values (real and imaginary). The entire k-space points in the kx-direction are fully filled when the Gx gradient is turned on. The change from line-to-line is performed using the Gy gradient pulse. In MRI exams, various trajectory schemes exist to fill the k-space. The Cartesian sampling scheme is the most used technique in MRI. All the points in the readout direction are swept before going to the next line. Figure I.13 illustrates the Cartesian method for travelling in the k-space using the readout and phase encoding gradients pulses.

I.6. MR pulse sequence

The MR pulse sequence consists of a series of RF pulses and gradient pulses. It is performed onto a sample to generate an MR signal. In addition, using the MR pulse sequence, various contrasts can be obtained by adjusting the sequence parameters such as the "repetition time" (TR) and the "echo time" (TE), where TR is the delay between two similar RF pulses and TE refers to the delay between the RF excitation pulse and the echo center. Basically, the MR pulse sequences are commonly based on the three procedures: slice selection with RF pulse, phase encoding, and frequency encoding of data to fill the k-space.

I.6.1. Spin echo pulse sequence

In Spin Echo (SE) pulse sequence, an RF pulse of 90° is used to create an echo. It brings the magnetization to the transverse plane, and would cancel out the longitudinal component. When the RF excitation pulse is turned off, the spins precess with different angular frequencies and lose their phase coherence rapidly, since particles experience a slightly different magnetic field. After a delay t, a second RF pulse of 180° is applied, following by an additional delay t, resulting in echo formation. Indeed, after the 90° RF pulse, a first signal is detected in the coil induced by the transversal component decreasing called Free Induction Decay (FID) and is characterized by time constant T_2^*, according to Equation 1.17.

In the presence of macroscopic field inhomogeneity, the spins dephase quickly with various precession frequencies during the first delay t. Next, the refocusing RF pulse inverts the precession direction of the protons. Hence, it refocuses the transversal magnetization and creates a new echo

at a specific moment called echo time (TE) which is equal to $2t$. This acquisition method is called spin-echo sequence. In addition, the refocusing pulse allows cancelling out of the effects of macroscopic magnetic field inhomogeneities; therefore, the signal decays with a time constant T2 instead T_2^* as expressed in Equation 1.15.

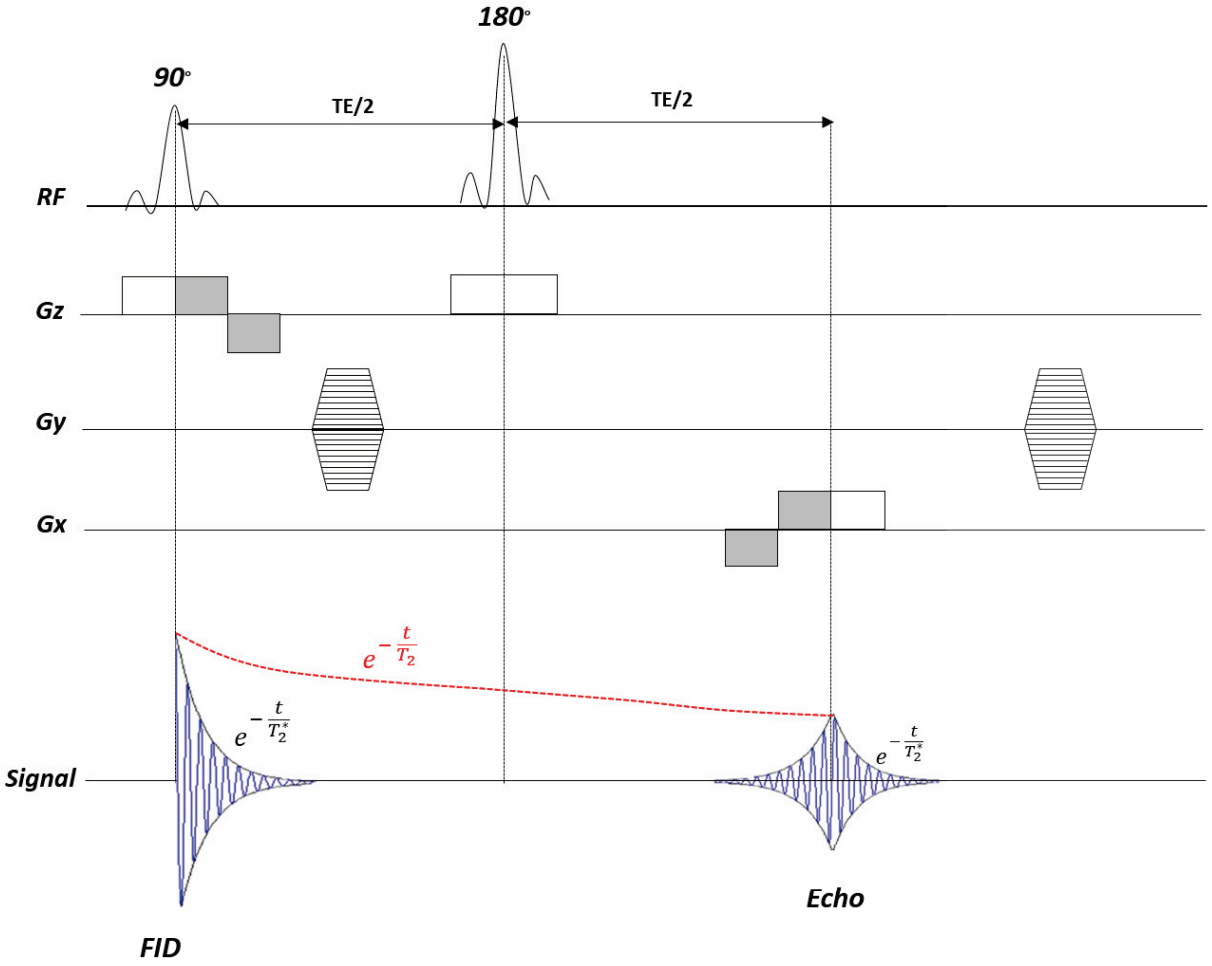

Figure I.14: MR pulse sequence diagram for Spin Echo sequence. After the 90° RF pulse, a first signal is detected in the coil induced by the transversal component decreasing called Free Induction Decay (FID), After a delay t = TE/2, a second RF pulse of 180° is applied followed by an additional delay t = TE/2. It refocuses the transversal magnetization and creates a new echo at a specific moment TE

$$S_{TE} = S_0 \, e^{\left(-\frac{TE}{T_2}\right)} \tag{1.33}$$

where S_{TE} is the maximum of the echo measured at TE time and S_0 is the maximum of signal FID. Figure I.14 and Figure I.15 illustrate the diagram of the SE pulse sequence.

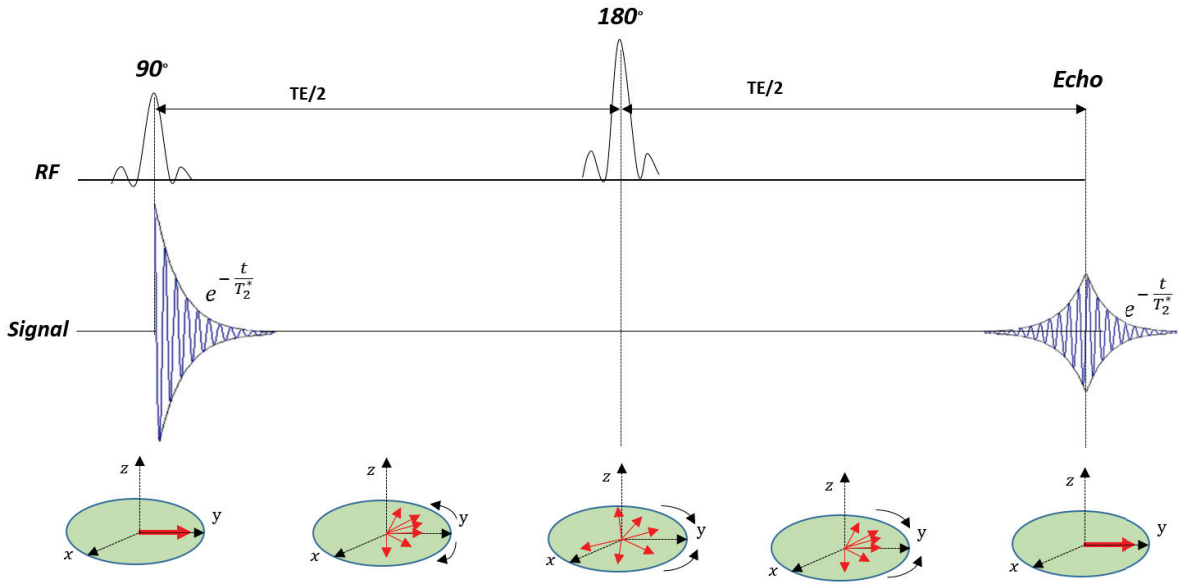

Figure I.15: When the RF excitation pulse of 90° is turned off, the spins precess with different angular frequencies and lose their phase coherence rapidly due to macroscopic magnetic field inhomogeneity during the first delay t=TE/2. Then, the refocusing RF pulse of 180° inverts the precession direction of the protons and refocuses the transversal magnetization, creating a new echo at t= TE.

I.6.2. Gradient echo pulse sequence

Instead of the refocusing RF pulse in the SE pulse sequence, the Gradient Echo (GE) pulse sequence uses a pair of readout gradients to dephase and rephase spins to create an echo. As described above for the SE pulse sequence, the GE follows the same preparation scheme: an RF excitation pulse in conjunction with a slice selection gradient pulse G_z, followed by a phase encoding gradient G_y.

However, during the signal FID decaying, a negative gradient pulse is applied in the readout direction in order to dephase the spin in the transverse plane.

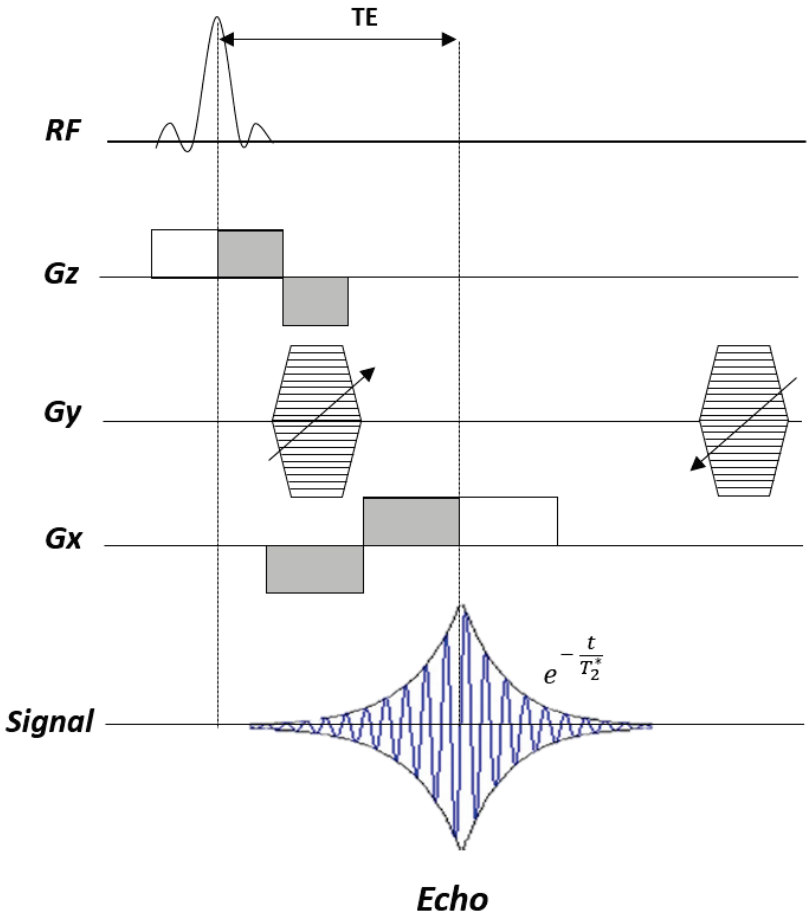

Figure I.16: MR pulse diagram of a gradient echo pulse sequence GE. The GE follows the same preparation scheme: an RF excitation pulse in conjunction with a slice selection gradient pulse Gz, followed by a phase encoding gradient Gy. During the signal FID decaying, a negative gradient pulse is applied in the readout direction in order to induce spins dephasing. Then a positive gradient pulse with twice the area of the negative gradient is applied to refocus the magnetization and create an echo at time TE.

Unlike the SE pulse sequence, the GE uses a positive gradient pulse with twice the area of the negative gradient to refocus the magnetization and create an echo at time TE. The signal decaying in GE pulse sequence is characterized by a time constant T_2^*, according to the following expression:

$$S_{TE} = S_0 \, e^{\left(-\frac{TE}{T_2^*}\right)} \tag{1.34}$$

Due to the quick decaying of the MR signal, the GE pulse sequence is used in routine examinations with short TE as well as a low RF flip angle for fast imaging (Frahm et al., 1986). Figure I.16 illustrates the diagram of the GE pulse sequence.

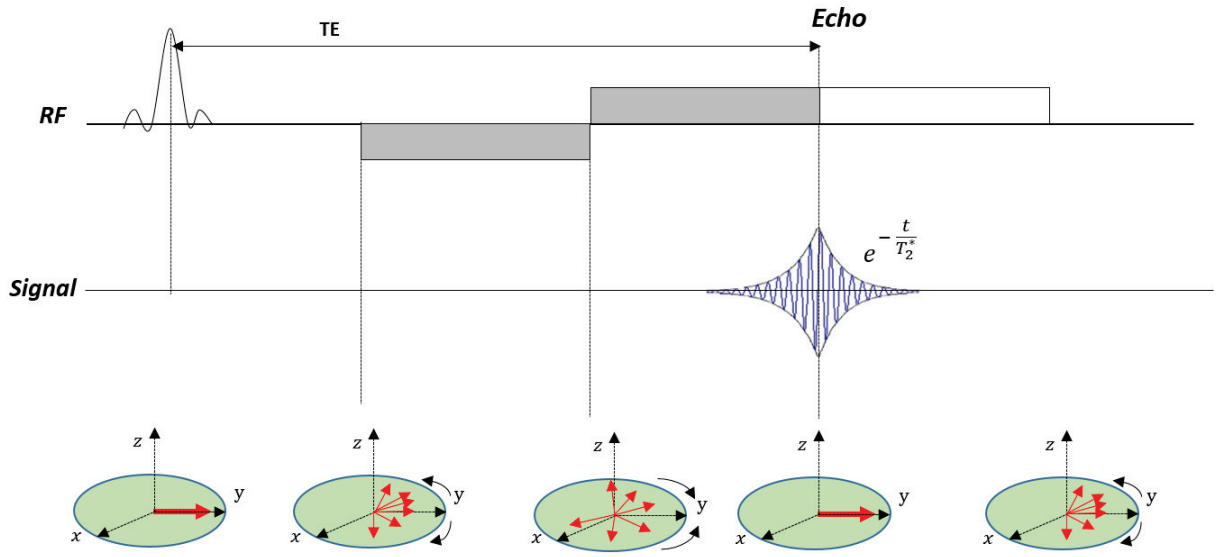

Figure I.17: After the RF pulse, the spins precess with different frequencies due to the field inhomogeneities. The dephasing gradient pulse allows accelerating the spins' dephasing by increasing the precession frequencies according to Equation 1.25, resulting in a quick loss of coherence. Therefore, using a positive gradient pulse with twice the area, the spins are refocused and create an echo at time TE.

I.6.3. Inversion Recovery pulse sequence

The Inversion Recovery (IR) pulse sequence, also known as the Magnetization-Prepared pulse sequence, is a variation of the spin echo pulse sequence. The IR pulse sequence is widely used to enhance the T1-contrast of the MR images. Indeed, an additional RF pulse of 180° is added prior to the main RF excitation pulse to invert the magnetization $\vec{M}$ to point along the z-axis.

A delay called the inversion time (TI) is played out between the 180° RF pulse and the excitation RF pulse. The delay determines the amount of the T1-weighting of the pulse sequence. After the inversion RF pulse, the longitudinal magnetization of tissues regrows under their different intrinsic T1 relaxation toward the +*z*-direction. In fact, the IR provides enhanced T1-contrast images by displaying the RF excitation pulse of 90° when the longitudinal magnetizations of different tissues are well separated.

The TI determines the amount of contrasts in the images. In addition, the IR could be used for signal suppression or "nulled" by carrying out the 90° RF pulse when the longitudinal magnetization of the unwanted tissue reaches zero. For tissue suppression, typically $TI \approx 0.69 \times T1$.

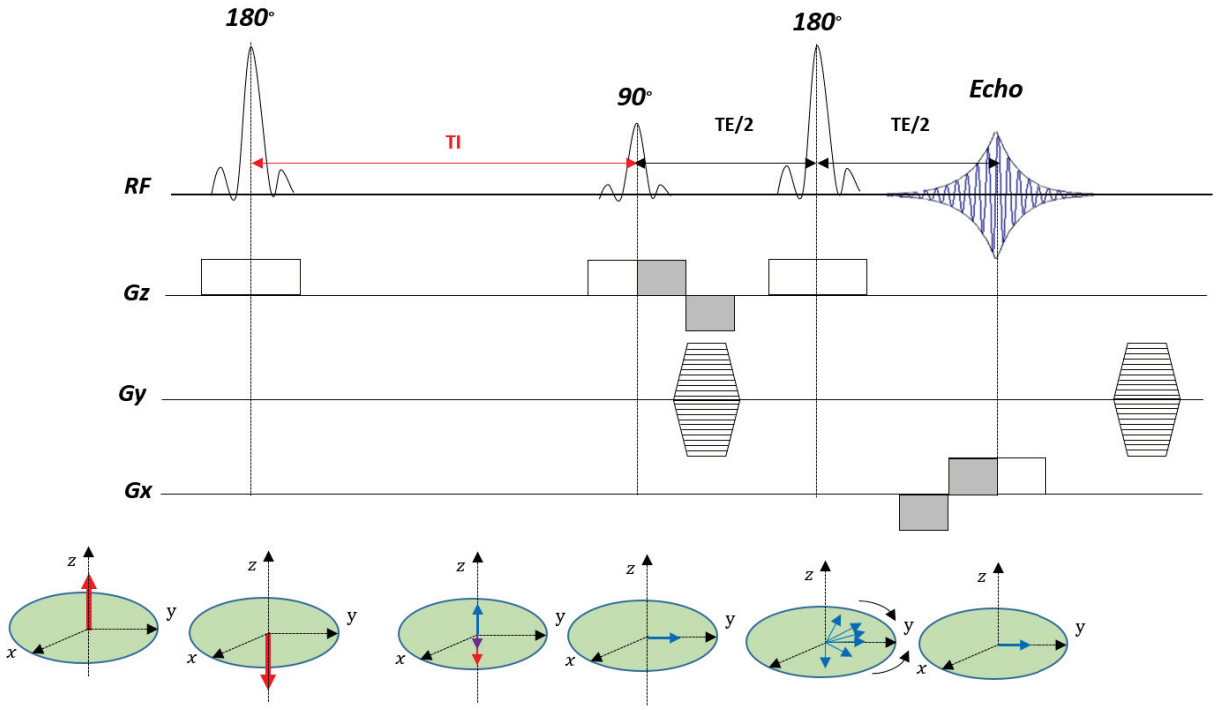

Figure I.18: Inversion Recovery pulse sequence diagram. The first RF pulse of 180° inverts the magnetization M to point along the -z-axis. The TI time is played out between the 180° RF pulse and the excitation RF pulse. After the inversion RF pulse, the magnetization of tissues regrows under their different intrinsic T1 relaxation toward the +z-direction.

I.6.4. Echo Planar Imaging pulse sequence

Various acquisition approaches have been introduced in order to accelerate the acquisition pulse sequence, such as the Turbo Spin Echo pulse sequence (TSE), which uses a train of 180° RF pulses to generate successive echoes (Hennig, 1988; Hennig et al., 1986).

On the other hand, Peter Mansfield has introduced a new acquisition approach based on a train of gradient echoes generated by a series of bipolar gradient pulses to sample the entire (or portion of) k-space (Mansfield, 1977), so called Echo Planar Imaging (EPI). The EPI module could be used with different pulse sequences such as SE and GE. Thanks to its high temporal resolution, the EPI is widely adopted for *in-vivo* clinical and preclinical scans such as for diffusion-weighted imaging or functional MRI. A detailed description of the EPI-based pulse sequences as well as the timing diagrams are provided in Chapter III and Chapter IV.

Diffusion MRI

Diffusion-weighted magnetic resonance imaging (dMRI) allows to study the diffusion of water molecules within biological tissue using a dedicated pulse sequence. Despite the fact that the first diffusion-weighted pulse sequence was introduced a long time ago by Stejskal and Tanner (Stejskal and Tanner, 1965), Le Bihan et al. have introduced the first diffusion-weighted image of the human brain (Le Bihan et al., 1986).

Over the years, it has been demonstrated that dMRI is a powerful tool for clinical application such as for detecting strokes (Moseley et al., 1990b). In addition, dMRI has been widely used to non-invasively delineate brain microstructure for a better understanding of the brain's functions and connectivity and its abnormalities due to certain pathologies, specifically those affecting the white matter such as white matter demyelinating and dysmyelinating diseases (Moseley et al., 1990a).

Therefore, there is an increased interest among the neuroscientific community in this modality since it demonstrates the ability to non-invasively provide information on the organization of brain tissue and to model microstructure (Le Bihan and Johansen-Berg, 2012).

I.7. Physics principles

I.7.1. Principles of diffusion

It has been demonstrated that, in nature, molecules tend to move from a region of high concentration to one of low concentration. Fick's first law explains this phenomenon through the following equation:

$$J = -D\nabla\zeta(\mathrm{r},\mathrm{t}) \tag{1.35}$$

where J is the net particle flux, D is the diffusion coefficient, and ζ is the concentration of the particle at position r at time t.

The rate of changing the particle is related to the local diffusion flux according to the conservation of mass law:

$$\frac{\partial\zeta}{\partial\mathrm{t}} = -\nabla J \tag{1.36}$$

Then, if we use Equation 1.35, Fick's second law is given by the following statement:

$$\frac{\partial\zeta}{\partial\mathrm{t}} = -D\nabla^2\zeta \tag{1.37}$$

The probability that a particle displaces from an initial position (r) to another position (r') in a time t can be defined in a function of the particle concentration according to the Einstein law (Albert Einstein, 1905):

$$\zeta(r',\mathrm{t}) = \int \zeta(r,0)P(r|r',t)dr \tag{1.38}$$

where the probability function can be expressed as follows:

$$p(r|r',t) = \frac{1}{\sqrt{(4\pi Dt)^3}} e^{\left(-\frac{(r-r')^2}{4Dt}\right)} \tag{1.39}$$

Therefore, using Equation 1.39, the displacement of the molecules can be characterized by the diffusion coefficient, D, which is related to the displacement, (r-r'), of the molecules over a given time, t, via the Einstein equation (Fig.I.19).

$$\langle(r-r')^2\rangle = 6Dt \tag{1.40}$$

Robert Brown has demonstrated that at ambient temperature, molecules such as pollen are in permanent motion and collide with each other (Brown, 1828); this is therefore true for molecules in biological tissue.

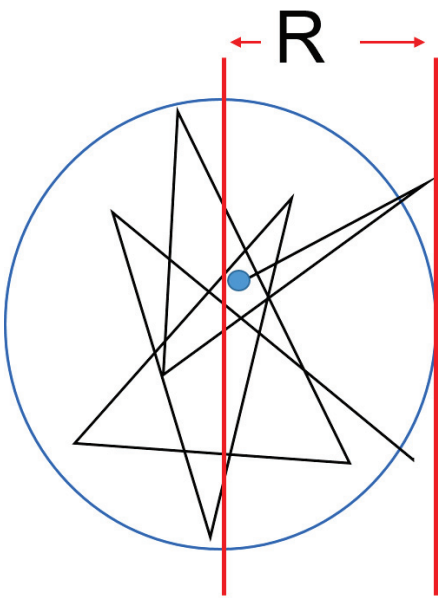

Figure I.19: The Brownian motion of a molecule. According to the Einstein equation, the displacement of molecule (R) is related to the diffusion coefficient, D, and the diffusion time t.

I.7.2. Isotropic diffusion

The mobility of a molecule can be further influenced by several factors, such as the molecular environment (tissue, liquid), molecular weight, intramolecular interaction (velocity) and temperature. In fact, the diffusion of molecules in a liquid environment (e.g., cerebrospinal fluid (CSF)) is similar in any direction in the space, so-called isotropic diffusion.

Hence, the diffusion of the molecule could be modeled by a sphere characterized by its eigenvalues (λ_1, λ_2, λ_3), where $\lambda_1 \simeq \lambda_2 \simeq \lambda_3$ (Fig.I.20.a). However, in biological tissue, i.e., grey matter (GM), the particle bounces and interacts with tissue components, such as the cell membrane and macromolecules. Therefore, the diffusion distance could be reduced and the displacement distribution is no longer Gaussian (Fig.I.20.b).

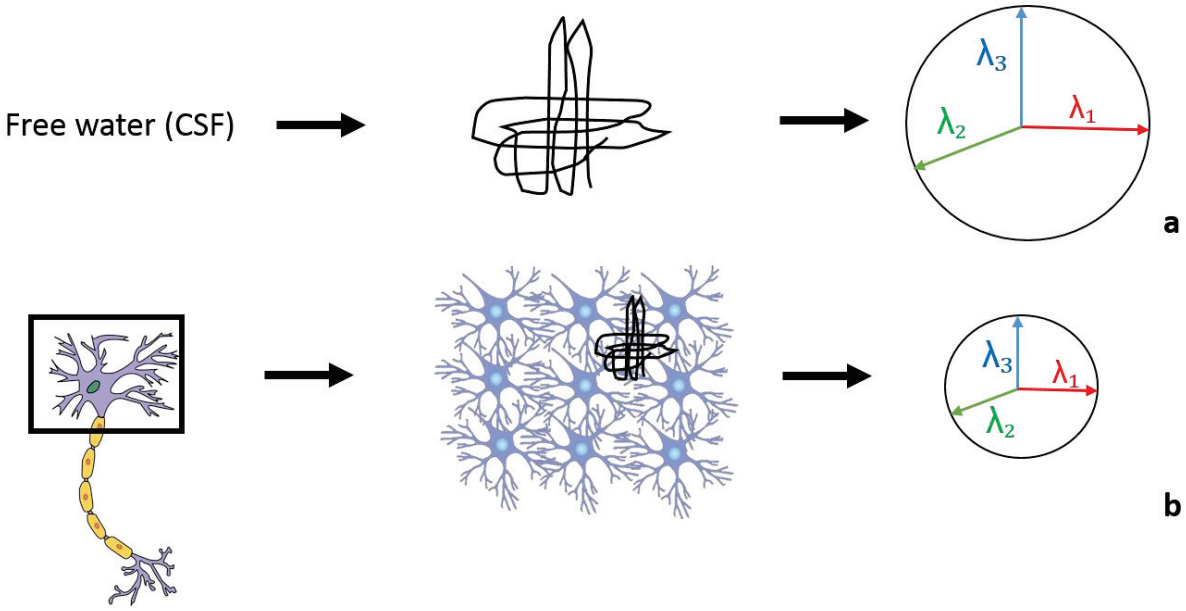

Figure I.20: The isotropic diffusion of a molecule in a pure liquid environment (CSF) (a) and the reduced displacement of a molecule in biological tissue such as grey matter (GM) (b).

I.7.3. Anisotropic diffusion

Furthermore, in more organized tissue such as the white matter (WM), the diffusion of the molecule is allowed in the direction parallel to the fibers and restricted in the perpendicular direction. This is the anisotropic diffusion, which can be modeled by an ellipsoid characterized by its eigenvalues (λ_1, λ_2, λ_3) where $\lambda_1 >> \lambda_2 \simeq \lambda_3$ (Fig.I.21).

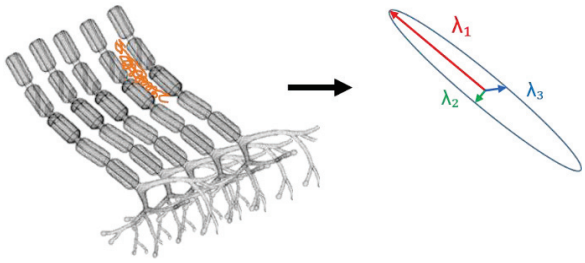

Figure I.21: The anisotropic diffusion of a molecule in pure white matter (WM). The diffusion is higher in the parallel direction of axons than in the perpendicular direction. Diffusion can be modeled by an ellipsoid characterized by its eigenvalues (λ_1, λ_2, λ_3) where $\lambda_1 >> \lambda_2 \simeq \lambda_3$.

I.8. Diffusion-weighted imaging

I.8.1. Pulse sequence

DMRI refers to sensitizing the MR signal to water diffusion in order to measure and map the distribution of the diffusion coefficient. Actually, the measurement of the diffusion of water molecules along a direction is performed using the Stejskal and Tanner-based MR pulse sequence. Indeed, the Stejskal and Tanner scheme uses two extra gradient pulses which are placed before and after the refocusing RF pulse 180° in the pulsed gradients spin echo PGSE pulse sequence (Stejskal and Tanner, 1965). Moreover, the used diffusion sensitizing gradient pulses have the same amplitude and duration time. The phase shift induced by the first diffusion gradient can be written as follows:

$$\phi_{G1} = -\gamma(\delta G)x_1 \tag{1.41}$$

where γ is the gyromagnetic ratio, G is the magnitude of the diffusion gradient pulses, δ is the width of the gradient G, and x_1 is the position of the particle when the first gradient G_1 is applied. Similarly for the second gradient pulse:

$$\phi_{G2} = -\gamma(\delta G)x_2 \tag{1.42}$$

Therefore, the net phase change between the two gradient pulses can be estimated according to the following expression:

$$\phi_{G1} - \phi_{G2} = -\gamma(\delta G)(x_1 - x_2) \tag{1.43}$$

Stejskal et al. have demonstrated that the diffusion of molecules could be characterized by measuring the signal attenuation due to the dephasing of protons under the diffusion gradient pulses. In fact, the resultant signal intensity $I\ (p)$ in an image voxel is calculated as a function of the diffusion parameters via the following equation:

$$I(p) = I_0 e^{(-\gamma^2 ||G||^2 \delta^2 \left(\Delta - \frac{\delta}{3}\right) D)} \tag{1.44}$$

where I_0 is the initial MR signal before applying the diffusion gradients and Δ is the separate time between the two gradients lobes. In dMRI acquisition, Le Bihan et al. (Le Bihan et al., 1986) have coined the term “b-value” to express the amount of the diffusion sensitizing which characterizes

the diffusion gradient pulses (amplitude, shape and timing). The b-value can be written as the following equation and expressed by (sec/mm^2).

$$b = \gamma^2 G^2 \delta^2 (\Delta - \frac{\delta}{3}) \quad (1.45)$$

Therefore, Equation 1.42 can be simplified as:

$$I(p) = I_0 e^{-bD} \quad (1.46)$$

The diagram of the Stejskal et al. dMRI pulse sequence is illustrated in Figure.I.22.

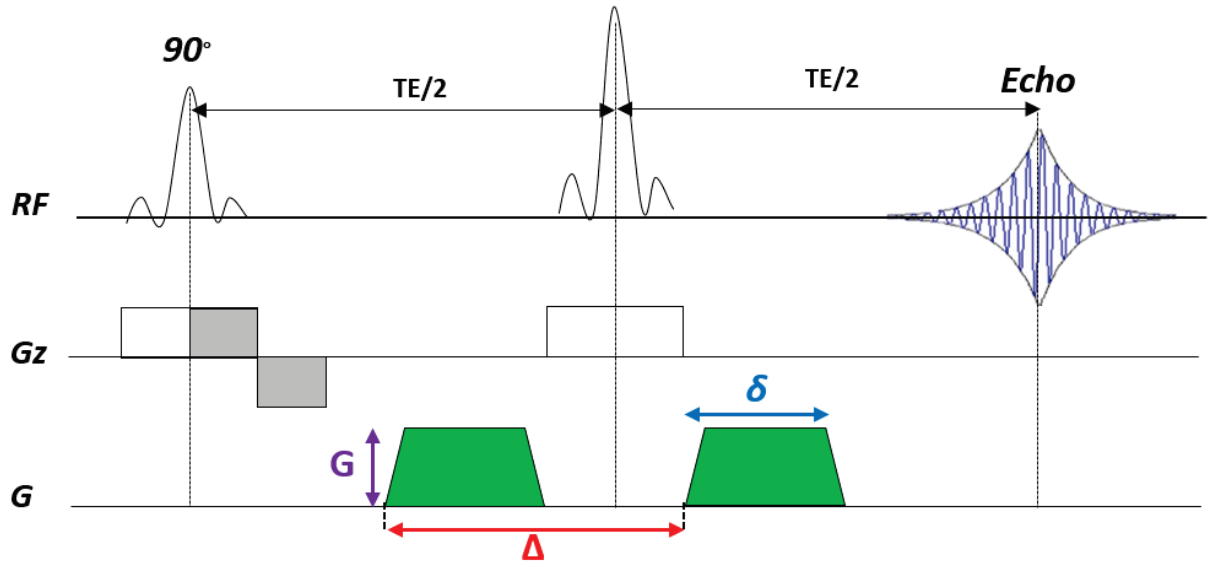

Figure I.22: The schematic of the Stejskal and Tanner-based MR pulse sequence. G is the magnitude of the diffusion gradient pulses; δ and Δ are, respectively, the width and the separate time between the two gradient lobes.

I.8.2. Apparent diffusion coefficient and trace imaging

DMRI, dependent on the motion of water molecules, provides information regarding tissue integrity. However, the diffusion of molecules could be restricted by the surrounding molecules and tissues. The impedance of water molecules can be quantitatively assessed using the Apparent Diffusion Coefficient (ADC) values. Using Equation 1.44, the diffusion coefficient can be calculated as:

$$D = -\frac{1}{b}\ln(\frac{I(p)}{I_0}) \quad (1.47)$$

Using two or more dMRI images with different b-values, the ADC map is computed on a pixel-by-pixel basis. By convention, a region with high diffusivity which corresponds to high ADC values will be displayed as a high-intensity signal region, whereas a restricted diffusivity region or low ADC values will be displayed as low-signal regions.

The trace image, also called the isotropic diffusion, is a computed map derived from diffusion images acquired with different diffusion encoding directions. The trace map is calculated by averaging pixel-by-pixel the signal intensities. Unlike the ADC map, the region with high diffusivity such as the CSF appears with a low-intensity signal due to the signal loss induced by the application of diffusion gradients.

Assuming the diffusion is performed along the x-, y-, and z- axis, the resulting MR signal can be written as:

$$I_x(p) = I_0 e^{-bD_{xx}}$$

$$I_y(p) = I_0 e^{-bD_{yy}}$$

$$I_z(p) = I_0 e^{-bD_{zz}} \quad (1.48)$$

The trace image signal can be then computed as follows:

$$I(p) = I_0 e^{-b(D_{xx}+D_{yy}+D_{zz})/3} \quad (1.49)$$

Figure I.23 illustrates an example of ADC and Trace images.

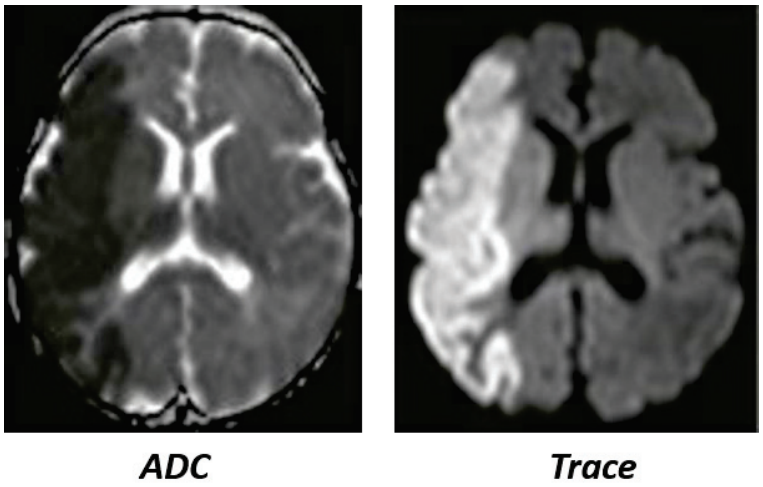

Figure I.23: Example of Trace maps and apparent diffusion coefficient (ADC) maps computed from diffusion-weighted (DW) images acquired in a 3-week-old neonate with an acute stroke (From Jessica L. Wisnowski et al. 2015).

I.9. Diffusion Tensor Imaging

I.9.1. Description

The gold standard spin-echo Stejskal and Tanner-based MR pulse sequence allows measuring the diffusion of the water molecule along one axis using the diffusion-sensitizing gradient pulses. In isotropic regions such as in CSF, the displacement of particles can be simply characterized by the ADC or the trace using Equation 1.39. However, for anisotropic areas such as white matter, the measurement should be repeated and varying in the direction of diffusion-sensitizing gradient pulses, since a higher number of encoding directions are required to characterize the diffusion of water molecules in more complex tissues.

$$D = \begin{pmatrix} D_{xx} & D_{xy} & D_{xz} \\ D_{yx} & D_{yy} & D_{yz} \\ D_{zx} & D_{zy} & D_{zz} \end{pmatrix} \tag{1.50}$$

Therefore, the diffusion of the water molecule is no longer characterized by a single scalar coefficient; however, it requires a mathematic model termed tensor, D, which describes the

molecular diffusion through many directions. The Diffusion Tensor is calculated as in Equation 1.50.

Using the Tensor model, Equation 1.39 can be resolved as follows:

$$p(r|r',t) = \frac{1}{\sqrt{(4\pi|D|t)^3}} e^{(-\frac{(r-r')^2}{4Dt})} \quad (1.51)$$

where |D| is the determinant of the diffusion coefficient.

The diagonal terms D_{xx}, D_{yy}, and D_{zz} characterize the molecular diffusion along the three axes (x, y, and z); however, the other terms are equal due to the symmetry of the tensor ($D_{xy} = D_{yx}$, $D_{xz} = D_{zx}$, and $D_{yz} = D_{zy}$). By applying the diffusion-sensitizing gradients in at least six non-collinear directions, the tensor models the displacement of water molecules in each image voxel by an ellipsoid (Basser et al., 1994). In fact, tensor parameters allow characterization of the diffusion (i.e., the main orientation, the anisotropy degree) by characterizing the diffusion ellipsoid associated with the microstructure at an image voxel. The elements of the resulting tensor could be reduced to 3 elements by a mathematical procedure called matrix diagonalization or matrix rotation.

This results in a 3-dimensional information matrix of the three eigenvalues of each image voxel as shown in Figure I.24. Indeed, the eigenvalues (λ_1, λ_2, λ_3) associated with the computed eigenvectors of the diffusion ellipsoid are useful in characterizing the anisotropy in white matter tissues.

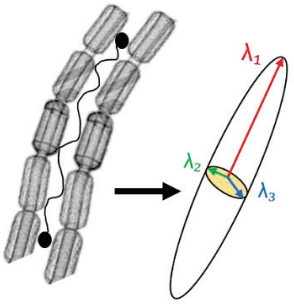

$$\mathbf{D} = \begin{bmatrix} D_{xx} & D_{xy} & D_{xz} \\ 0 & D_{yy} & D_{yz} \\ 0 & 0 & D_{zz} \end{bmatrix} \qquad \Lambda = \begin{bmatrix} \lambda_1 & 0 & 0 \\ 0 & \lambda_2 & 0 \\ 0 & 0 & \lambda_3 \end{bmatrix}$$

Figure I.24: The 6-elements of the tensor D could be reduced to a 3-elements matrix (Λ) by a mathematic process called diagonalization. The obtained eigenvalues (λ_1, λ_2, λ_3) are useful in characterizing the anisotropy in white matter tissue.

I.9.2. DTI-metrics

After the tensor fitting process, the computed eigenvalues (λ1, λ2, and λ3), as well as the eigenvectors (v1, v2, v3) provide information about the diffusion anisotropy and tensor orientation at each image voxel. Various DTI-metrics such as the fractional anisotropy (FA), the mean diffusivity (MD), the axial diffusivity (AD), and the radial diffusivity (RD) can be computed to characterize the diffusivity (Pierpaoli and Basser, 1996). The FA is the most widely used DTI-derived parameter, and it allows quantifying the degree of directionality of diffusion. The FA is calculated as follows:

$$FA = \sqrt{\frac{1}{2}}\frac{\sqrt{(\lambda_1-\lambda_2)^2(\lambda_1-\lambda_3)^2(\lambda_2-\lambda_3)^2}}{\sqrt{(\lambda_1{}^2+\lambda_2{}^2+\lambda_3{}^2)}} \quad (1.52)$$

The FA has a value in the range of 0, for the isotropic diffusion such as in CSF, to 1, for the high anisotropic tissue such as in the corpus callosum. In addition, the mean diffusivity allows quantifying the magnitude of diffusivity along the three main directions, and it is calculated as the average of the three eigenvalues:

$$MD = \frac{1}{3}(\lambda_1 + \lambda_2 + \lambda_3) \quad (1.53)$$

The axial diffusivity characterizes the diffusivity along the main direction of axons and it is equal to the main eigenvalues of the ellipsoid:

$$AD = \lambda_1 \quad (1.54)$$

However, the radial diffusivity describes the diffusivity in the perpendicular directions and it is calculated as follows:

$$RD = \frac{1}{2}(\lambda_2 + \lambda_3) \quad (1.55)$$

All of these DTI-derived metrics can be jointly or separately computed and used to characterize diffusion anisotropy and to provide further information about the tensor in each image voxel. The combination of these metrics reflects the physical properties of the biological tissues and allows the non-invasive detection of microstructural changes related to neuronal degeneration.

Moreover, an additional color-coded FA map could be computed and used to visualize the orientation and the organization of the white matter fibers according to the coordinate of their main direction (left-right= red, anterior-posterior= green, and inferior-superior= blue plus intensity proportional to the FA) (Pajevic and Pierpaoli, 2000).(See Figure I.25)

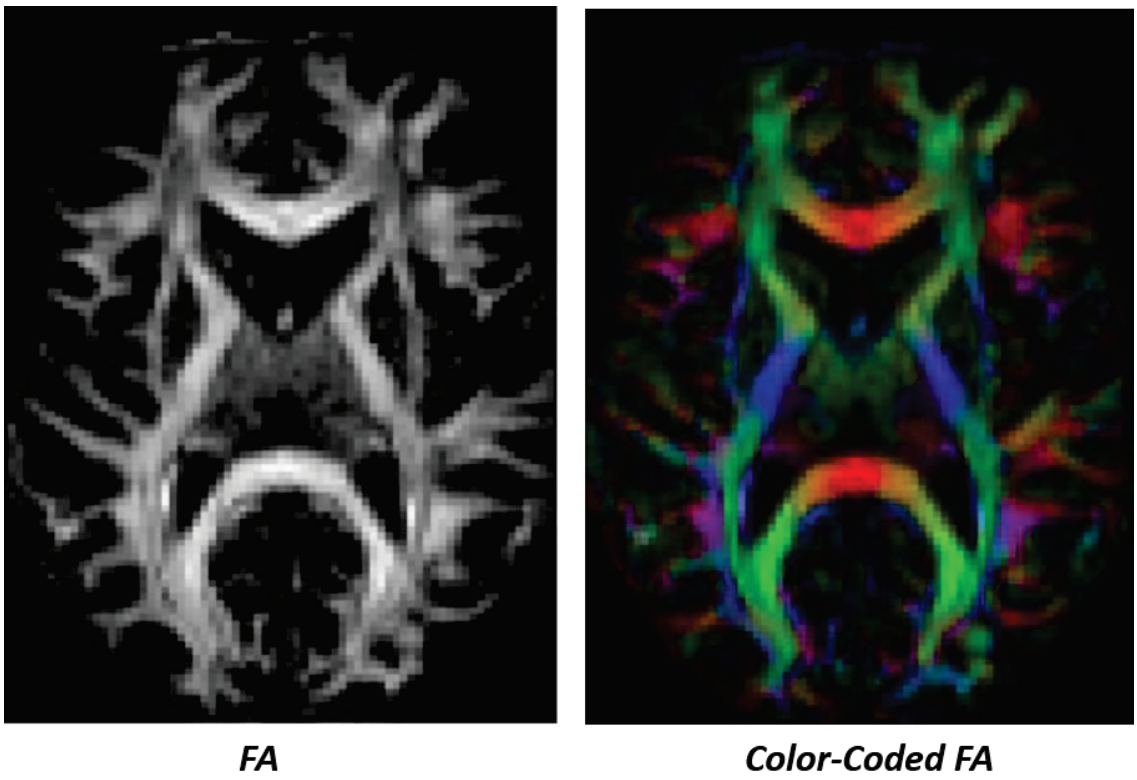

Figure I.25: Example of fractional anisotropy (FA) map and color-coded FA map derived from DT data. The colored FA map defines the orientation and the organization of the white matter fibers according to their main direction (left-right= red, anterior-posterior= green, and inferior-superior= blue) (from (Descoteaux, 2008)).

I.9.3. Acquisition strategies

The advanced dMRI scheme such as for DT imaging (DTI) requires an accelerated acquisition to produce diffusion-weighted images through multiple directions (>6) in clinically acceptable scan time (~30 min). The basic sequences such as the PGSE presented above are not a suitable approach for DTI acquisition due to their long scan duration. Therefore, various acquisition pulse sequences have been designed and used in the last two decades to demonstrate the feasibility of performing DTI acquisition within clinical conditions.

- **Cartesian approach**

The EPI pulse sequence is presented above and detailed in Chapter III. This acquisition approach has been used typically for dMRI acquisition due to its scan speed and its low sensitivity to motion. Although various forms of image artifacts corrupt the dMRI data, the EPI pulse sequence still remains the suitable choice for most dMRI applications. Advanced approaches such as parallel imaging techniques (Griswold et al., 2002; Pruessmann et al., 1999) have been introduced and used with the EPI method in order to improve the temporal and spatial resolution as well as to reduce the images artifacts.

- **Non-Cartesian approach**

Several acquisition methods based on non-Cartesian sampling of k-space have been used in dMRI examinations. For example, interest in the Radial methods has grown mainly due to its high robustness to motion artifacts (Li et al., 2011). In addition, with radial trajectory the central k-space is highly oversampled since all k-space lines pass through this region. Unlike the classic method, the radial sampling scheme generates data points that do not fall into a rectangular matrix. Therefore, for data reconstruction, the acquired k-space points should be transformed into a Cartesian format; this is called the "*gridding*".

The Periodically rotated overlapping parallel lines with enhanced reconstruction, termed PROPELLER (Wang et al., 2005) is the commonly used radial method for dMRI acquisition. Instead of a single radial line, PROPELLER uses a rotated radial strip.

Last, the spiral trajectory could be also used such, as SNAIL introduced by Liu et al. (Liu et al., 2004). The k-space sampling is performed using continuously oscillating gradient pulses. Figure

I.26 illustrates an example of the Cartesian EPI-based sampling scheme and non-Cartesian trajectory.

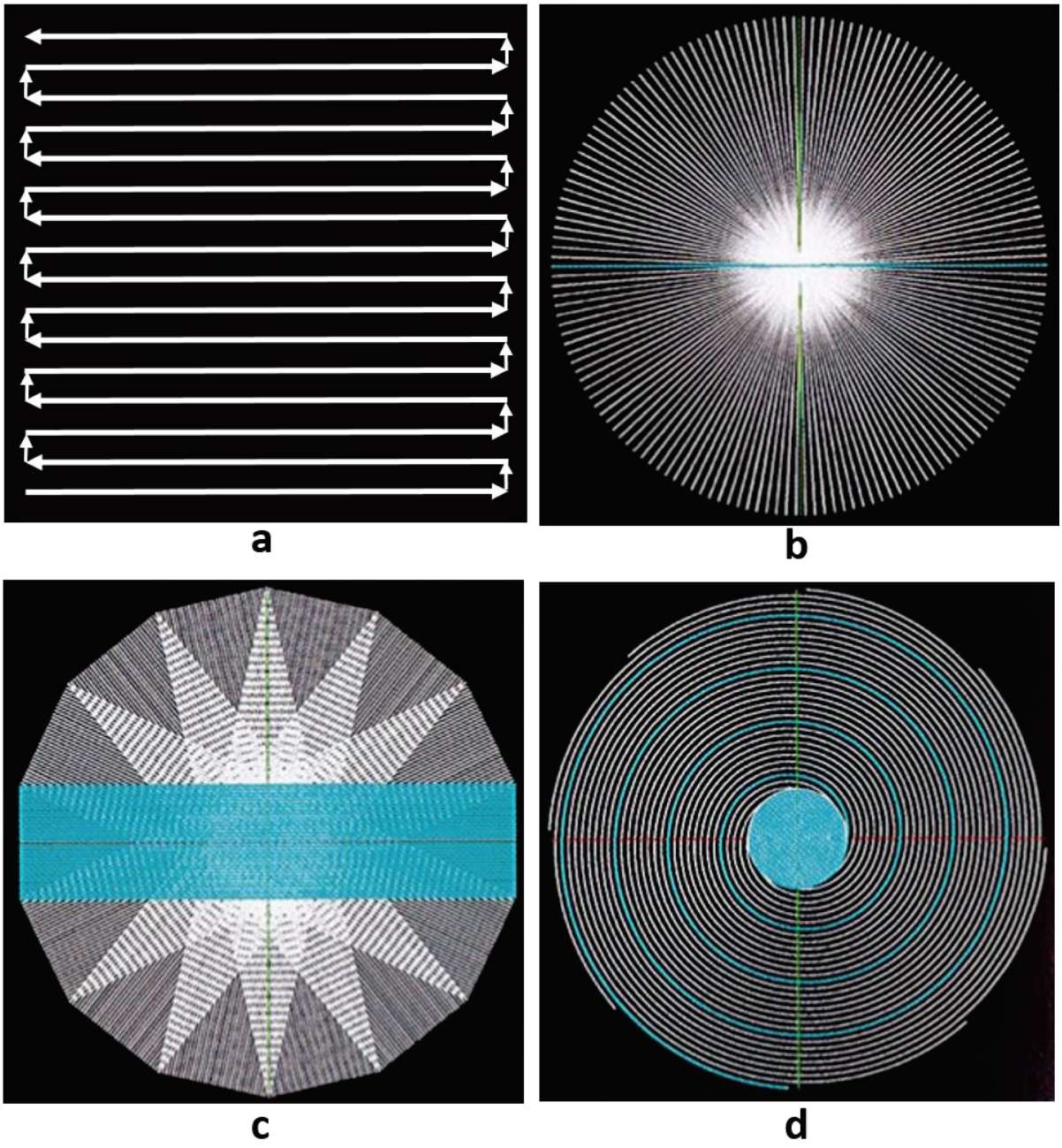

Figure I.26: Cartesian (a) and Non-Cartesian k−space trajectories: (b) radial, (c) PROPELLER, (d) spiral sampling schemes. (From (Gupta, 2015)).

I.10. Tractography

Tractography is one of the most promising applications of dMRI. In the last decades, it has been widely used to tract and to non-invasively visualize anatomical bundles from the features of the diffusion profile. Indeed, the tractography algorithms allow performing a virtual dissection of white matter fibers using dMRI data acquired in various directions on living brains (DTI data). Actually, the anisotropic diffusion profile within each voxel is taken as a basis for deducing the local fiber orientation distribution. In each image voxel, the dMRI-based tractography defines the fiber pathways by following the main eigenvector or orientation of the ellipsoid, in the simplest case described as a tensor model with a single principal axis (Fig.I.27).

Although attractive in its simplicity, the dMRI-based data may oversimplify the underlying neuroanatomy and the connectivity. In fact, the tensor model has been demonstrated to be unsuitable in complex brain regions that contain termed “crossing fibers”, and it has been further criticized for possible false negatives and positives (Tournier et al., 2011).

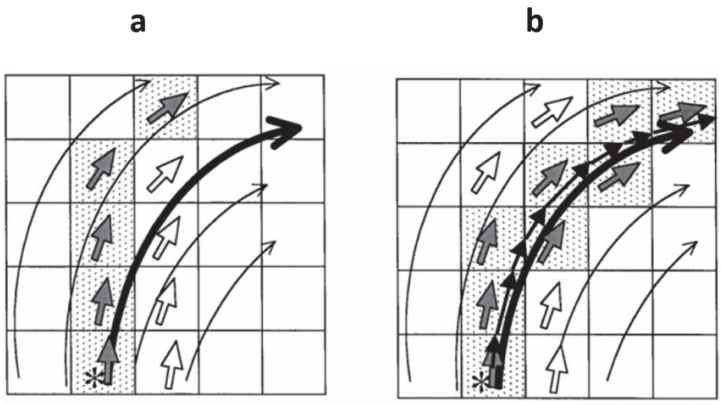

Figure I.27: The actual fibers are indicated by curved arrows, and the average fiber directions in the voxel are displayed as open arrows. The connected voxels resulting from tracking are shaded, using dots. The standard tractography approach leads to deviation from the actual fiber to be

tracked (a), The tractography approach named fiber assignment by continuous tracking (FACT) (b) improves the tractography DTI-based results and to achieves high-resolution three-dimensional tracking of axonal projection (Mori et al., 1999).

Mori et al. have introduced and demonstrated an approach named fiber assignment by continuous tracking (FACT) to improve the tractography DTI-based results and to achieve high-resolution three-dimensional tracking of axonal projection (Mori et al., 1999) (Fig.I.27).

Recently, numerous advanced acquisition and tractography, such as the Q-ball (Tuch, 2004) and the constrained spherical deconvolution (Tournier et al., 2012) approach have been proposed to further improve the tractography results and to overcome the "crossing fiber" issue and the limitations of the DTI model.

Conclusion

This Chapter describes the physics principles behind nuclear magnetic resonance at microscopic and macroscopic levels, including excitation, transverse and longitudinal magnetization, and relaxation times. In addition, it provides a technical introduction to the precess involved in magnetic resonance imaging as the spatial encoding of the MR signal (e.g., frequency and phase encoding) as well as a general presentation of the typical pulse sequences used in routine examination. Last, this Chapter reviews the basic principles of diffusion magnetic resonance imaging (dMRI) and introduces the main acquisition approaches used as well as the different k-space filling techniques.

Chapter II. State of the Art and Objective

Introduction

In the last two decades, dMRI has become a standard imaging tool to investigate cerebral microstructure and connectivity, and brain abnormalities due to certain pathologies such as multiple sclerosis and Alzheimer's Disease (Douaud et al., 2011; Schuff et al., 2009). Specifically, Diffusion Tensor Imaging (DTI) models the diffusivity of water molecules of each brain voxel with a Gaussian ellipsoid and provides quantitative information on the microstructure contained in each image voxel (Basser and Pierpaoli, 1998). Several scalar parameters can be derived out and used to characterize the anisotropy of the cerebral tissue (see Chapter I). Tractography is among the main applications of the dMRI in the Neurosciences. It uses the DTI-derived maps in combination with specific algorithms to reveal and visualize white matter fiber pathways (Descoteaux et al., 2007).

The context

Performing MRI on the non-human primate brain plays a crucial role in understanding brain functions and architecture. In addition, non-human primates could also be used to validate several imaging techniques such as functional and structural methods. Within this context, the Rhesus macaque (*Macaca mulatta*) has been widely adopted in many neurobiological studies due to the strong functional (Hutchison et al., 2015; Wey et al., 2014) and structural (Semendeferi et al., 2002) homologies of the macaque brain with the human brain. Therefore, the Rhesus macaque has been amply involved as a key model in many brain dMRI studies to investigate normal and abnormal brain functions and to probe brain connectivity and tissue properties.

One of the major added values of cerebral dMRI on *in-vivo* non-human primates is that this approach can be further validated with complementary invasive processes such as neuronal tracer (Schmahmann and Pandya, 2006) or *ex-vivo* brain imaging. Indeed, the *ex-vivo* approach allows the achievement of high-resolution and high signal-to-noise-ratio (SNR) dMRI data, serving as ground truth microstructural data and a reference for mapping brain anatomical connectivity. Moreover, high-quality *ex-vivo* dMRI data can be used jointly with histological data for comparison and validation. Actually, this is particularly useful for studies that aim to test the legitimacy of dMRI-based tractography measures.

Performing dMRI on the *ex-vivo* brain has several experimental advantages, including longer scanning time as well as the absence of motion-induced artifacts. Several studies have reported the achievement of very high spatial resolution and high SNR dMRI data acquired on *post-mortem* fixed non-human primate brains (Calabrese et al., 2015; Feng et al., 2017; Schilling et al., 2017). For example, recently, Calabrese et al. have demonstrated the achievability of dMRI data on the *post-mortem* fixed macaque monkey brain with an isotropic voxel size of 0.15 mm x 0.15mm x 0.15mm in 46 hours. In fact, dMRI data were collected using an ultra-high MR system of 7T (Calabrese et al., 2015).

I.1. Why dMRI on the in-vivo macaque brain?

Although the *ex-vivo* dMRI approach allows reaching a significant achievement and has brought about important advances in the field, it does not maintain the non-invasive aspect of dMRI, and it excludes a wide range of pharmacological and longitudinal non-human primate studies.

In addition, D'Arceuil et al. have demonstrated that the water diffusivity and core physiological properties of cortex grey and white matter change due to the brain fixation process and to the natural degradation of *ex-vivo* biological tissues (D'Arceuil and de Crespigny, 2007). Therefore, there is a strong need for *in-vivo* high-resolution dMRI of the non-human primate brain.

I.2. dMRI on the in-vivo macaque brain: Challenges and limitations

Certainly, high spatial resolution is highly desired for *in-vivo* cerebral dMRI. However, practical challenges might hinder its achievement. In fact, the major limitations of high-resolution dMRI acquisition are basically the voxel size that can be reached on the *in-vivo* macaque brain. The achievable spatial resolution is constrained by the inherently low SNR of the dMRI acquisition and by its sensitivity to different artifact sources (e.g., magnetic susceptibility, head motions).

Moreover, for large non-human primates like the macaque monkey, dMRI experiments are usually performed using an MR scanner designed for human applications. The spatial resolution commonly achieved in human dMRI studies (about 2 mm) is not sufficient with regard to the small size of the macaque brain. In fact, the macaque brain is between 10 to 15 times volumetrically smaller than the human brain (Yin et al., 2009) (Fig.II.1). Therefore, performing dMRI with sub-millimetric

spatial resolution is increasingly required to delineate the thin white matter tract and to resolve fine-scale cerebral structures.

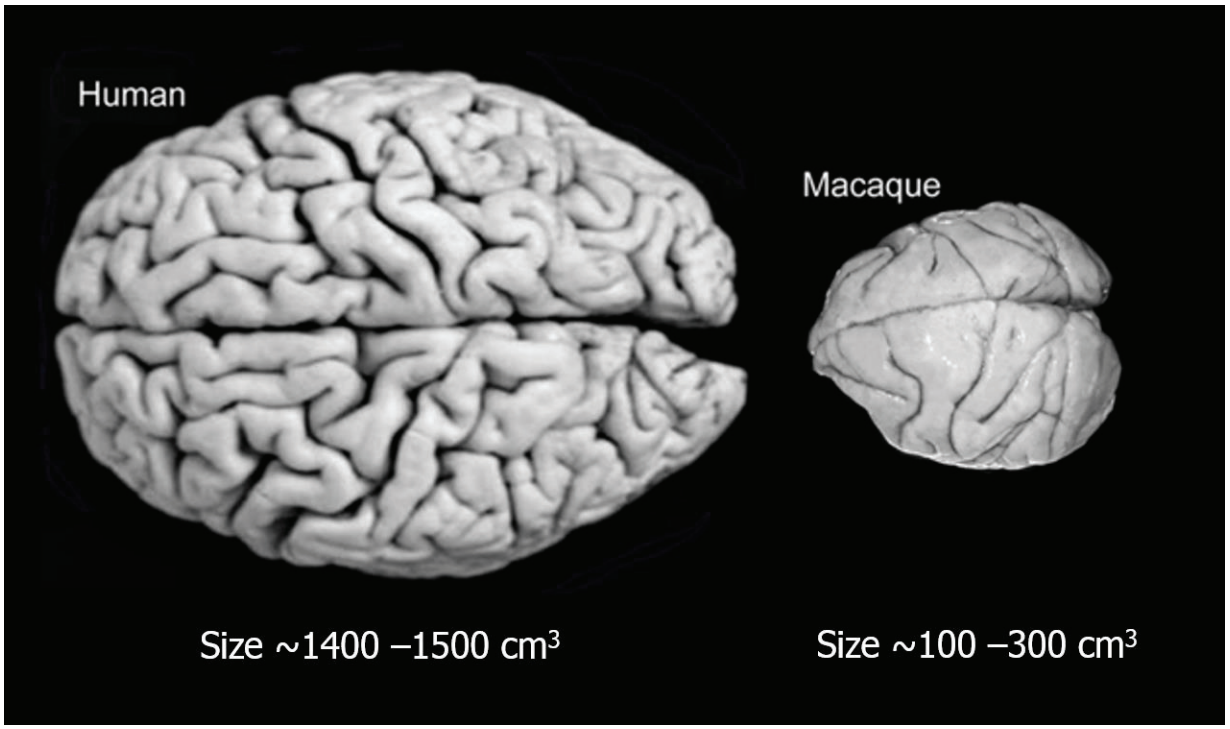

Figure II.1: Comparison between the human brain volume and the macaque brain volume (DeFelipe, 2011)

Furthermore, during dMRI examination the application of high gradient strength and the commutation rate such as for the EPI-based pulse sequence can induce an electric field in the human body, resulting not only in stimulation of peripheral nerves but could also produce cardiac and/or respiratory stimulations (Schaefer et al., 2000). Therefore, to keep the clinical MR scanner fairly safe for human imaging, gradient parameters such as the slew rate, defined as the maximum gradient strength divided by the rise time, should be maintained in an acceptable range. However, a gradient parameters restriction could limit the achievable spatial resolution in cerebral dMRI of the *in-vivo* macaque monkey brain.

Numerous methods exist to improve the low-SNR resulting from the small voxel size, including multiple averages. However, this approach is not efficient because it leads to a large scan time since

the SNR increases by a factor of the square root of the average number. Moreover, for the *in-vivo* dMRI scan, the extended acquisition time is not desirable and is limited by the acceptable anesthesia time.

State of the Art

Currently, dMRI examinations are carried out using the typical single-shot EPI pulse sequence in the standard clinical MR scanner. However, often the collected diffusion-weighted data suffer from low spatial resolution, blurring, and inherently low signal-to-noise ratio (SNR).

Over the last two decades, more advanced dMRI techniques have been developed and used to address these limitations and to improve *in-vivo* cerebral dMRI acquisition.

I.3. Diffusion MRI pulse sequence

Various dMRI acquisition methods have been used to increase the spatial resolution and to improve the efficiency of SNR of the dMRI of the *in-vivo* human brain. Fast Spin Echo (FSE) (Pipe et al., 2002), steady-state *free precession (SSFP)* (Le Bihan, 1988; McNab and Miller, 2010) and STIMS (Bilgic et al., 2017) MR pulse sequences were used to obtain diffusion-weighted images. In this study, we will focus on the dMRI pulse sequence based on the Cartesian EPI sampling scheme of k-space (Mansfield, 1977), which is the more popular method.

I.3.1. 2D Single-shot EPI dMRI pulse sequence

The gold standard multi-slice, two-dimensional, single-shot EPI (2D-ssEPI) acquisition method is widely used in clinical cerebral dMRI studies. In fact, it has been amply involved mainly for two reasons.

First, the 2D-ssEPI pulse sequence is characterized by an acquisition speed of up to ~100 ms per 2D slice and takes a few seconds to scan a whole brain volume. Indeed, this acquisition approach uses a series of bipolar readouts and phase-encoding gradients to fully sample the k-space lines after the RF excitation. This makes it a suitable method for *in-vivo* diffusion-weighting applications, requiring a large number of b-values and/or diffusion directions within the shortest possible scan time.

Second, the 2D-ssEPI-based method is very popular because of its low sensitivity to motion artifacts. Indeed, brain bulk motions, occur during the application of the strength diffusion-sensitizing gradients and introduce large phase variations in MR signals. The fast sampling of the whole k-space during a signal shot significantly reduces these phase variations and then limits the motion effects on DW-images.

Thanks to its rapidity and to its relative robustness against motion effects, the 2D-ssEPI is well established as the method of choice for routine and advanced dMRI protocols. However, this approach is prone to limited spatial resolution as well as to several artifacts such as off-resonance, magnetic field susceptibilities, and eddy-current artifacts. This is mainly due to the large Echo Train Length (ETL) required for covering the totality of Fourier space using variable readout gradients (EPI). For example, for a human data acquisition using the 2D-ssEPI pulse sequence, a field of view of 220 mm is typically used for a spatial resolution of 1.8 mm with an echo spacing of 0.8 ms, resulting in a matrix size of 123 x 123 mm^2. Therefore, the readout time of one line of k-space is about 1 ms, including rise up and down time of readout gradient. Thus, the ETL of 2D-ssEPI is 93 ms (123 lines x 6/8 PF x 1 ms).

The achievability of high-resolution artifact-free dMRI data is a crucial challenge that needs to be faced to push this technique to its limits for *in-vivo* dMRI study. In fact, the commonly reached spatial resolution in human dMRI studies performed at a clinical scanner using the 2D-ssEPI acquisition approach is in the range of 2 mm.

In a recent report, Fan et al. described a framework to improve the spatial resolution of dMRI data on the *in-vivo* human brain (Fan et al., 2017). In this study, the dMRI experiments were carried out using a custom-built 64-channel head coil and a 3T MR scanner equipped with a very performant gradient system capable of producing a maximal gradient field of 300 mT/m compared to 45 mT/m for the standard 3T scanner and up to 80-100 mT/m for the last generation of 3T MRI scanners. Thanks to their customized materials, the team of Fan et al have achieved dMRI data with an isotropic spatial resolution of 1 mm and a b-value of 1500 s/mm^2. Sixty diffusion-weighted volumes, as well as eight non diffusion-weighted volumes, were acquired in 20 minutes. The obtained data were used to investigate the ability to perform an accurate fiber orientation estimation specifically for cortical white-grey matter connectivity.

In addition, various acquisition schemes, including the readout-segmented EPI and phase-segmented-EPI have been proposed as alternative approaches for a standard clinical scanner to overcome the limitations of 2D-ssEPI. In recent years, it has been demonstrated that these methods yield a significant improvement of image quality and dMRI acquisition compared with conventional ssEPI.

I.3.2. 2D readout-segmented EPI (2D-rsEPI) dMRI pulse sequence

The readout-segmented 2D-EPI (2D-rsEPI) diffusion-weighted pulse sequence has been developed and used basically to address the limitations of the 2D-ssEPI acquisition method such as the susceptibility-induced artifacts. In contrast to the 2D-ssEPI method, the 2D-rsEPI acquisition scheme divides the k-space into numerous adjacent 2D-EPI segments along the readout direction (Fig.II.2).

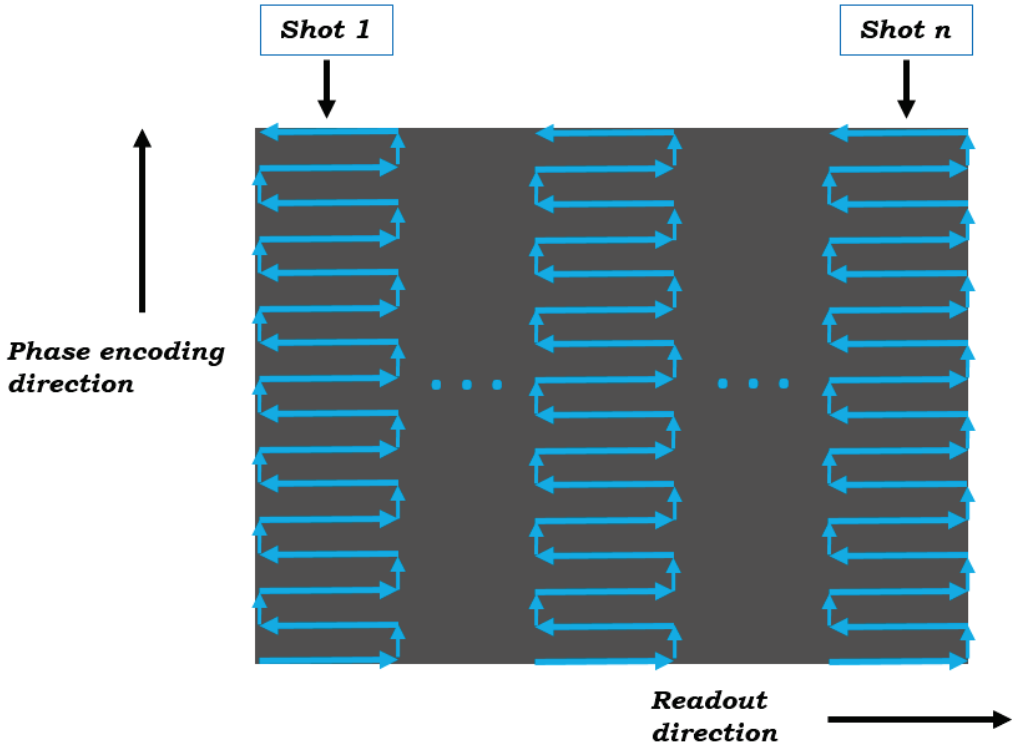

Figure II.2: The 2D-readout-segmented EPI (2D-rsEPI) sampling scheme: the k-space is divided into numerous adjacent EPI segments (1 to n segment) along the readout direction.

The 2D-rsEPI approach has been used in several human studies to further improve the achievable spatial resolution of dMRI acquisition as well as to reduce the artifacts related to the 2D-ssEPI methods such as blurring and geometric distortions (Holdsworth et al., 2008; Porter and Heidemann, 2009).

However, the major drawback of the 2D-rsEPI is the inter-shot phase variations that arise from the cerebrospinal fluid (CSF) pulsation of the brain and from the rigid body motion of the head. In fact, the small brain pulsation is amplified by the diffusion-sensitizing gradients, leading to a spatially dependent phase variation that is different from one segment to another one. This results in high-intensity ghosting artifacts in the diffusion-weighted images, and it induces an erroneous estimation of the diffusion tensor.

The navigator echoes acquisition method is typically used for detection and compensation for the inter-shots phase variations. The additional low-resolution data set was usually acquired after the imaging data to perform phase correction of data. Porter et al. used a 2D-navigator echoes reacquisition method combined with the 2D-rsEPI pulse sequence to perform dMRI on the *in-vivo* human brain. The 2D-navigator echo reacquisition approach aims to detect and remove in real time unusable data corrupted by ghosting artifacts and to reacquire a new dataset (Porter and Heidemann, 2009).

The effectiveness of the proposed acquisition scheme was demonstrated by performing dMRI data with a reduced motion-induced artifact at a 3T MR scanner. Nineteen diffusion-weighted slices encoded along three orthogonal diffusion directions as well as one volume-wise without diffusion-weighting were acquired with an in-plane spatial resolution of 0.9 mm x 0.9 mm. The k-space was divided into 11 EPI segments to further reduce the susceptibility-induced artifact, resulting in an acquisition time of 3 minutes. However, to compensate for signal loss due to the small voxel size in the slice direction, the slice thickness was set to 5 mm.

The added value of the proposed 2D-rsEPI acquisition approach in comparison with the classic 2D-ssEPI method was demonstrated in two ways: First, the ability to improve the achieved spatial resolution (1 mm x 1 mm x 5 mm) of human brain dMRI in feasible scan time (Holdsworth et al., 2008; Porter and Heidemann, 2009); second, the feasibility to achieve dMRI images with reduced

motion-induced artifacts on regions highly affected by the CSF pulsation (Frost et al., 2015; Porter and Heidemann, 2009) (Fig.II.3).

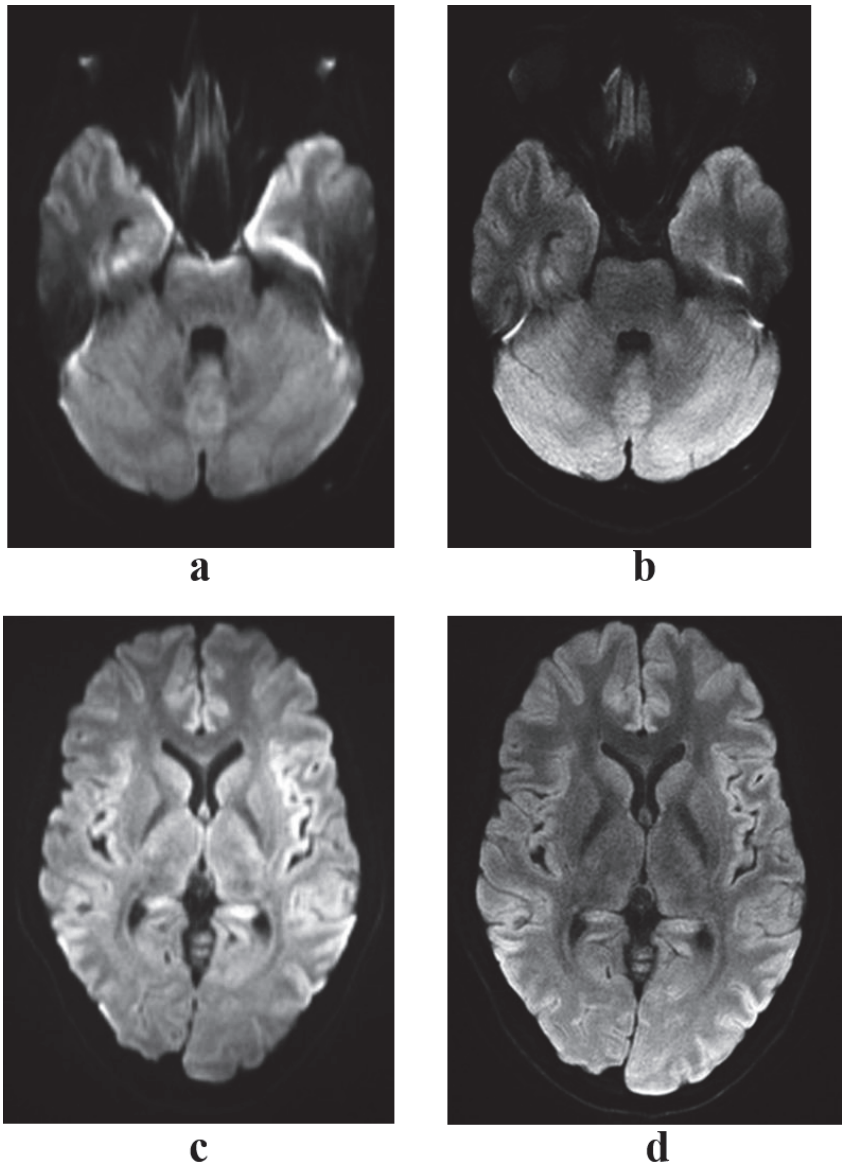

Figure II.3: Direct comparison of trace-weighted images acquired on the human brain at b-value = 1000 s/mm2 using the gold standard 2D single-shot EPI dMRI pulse sequence with a spatial resolution of 1.2mm x 1.2mm x 5mm (a and c), and the 2D readout segmented EPI dMRI pulse sequence (b and d) with a spatial resolution of 1 mm x 1 mm x 5mm (From: (Porter and Heidemann, 2009)*).*

The acquisition of all in-plane EPI segments of each k-space as well as the navigator data and the additional time required for reacquiring the removed data lead to a large total acquisition duration of 2D-rsEPI dMRI. Therefore, several acquisition strategies were developed and implemented to accelerate the acquisition of data and to improve the SNR efficiency.

First, parallel imaging techniques have been introduced to reduce the acquisition duration and minimize the geometric distortions (Griswold et al., 2002; Pruessmann et al., 1999). The effectiveness of this technique was demonstrated through several studies in clinical and preclinical studies where the coil sensitivity could partially compensate for the SNR decrease induced by acquisition acceleration (Dietrich et al., 2007; Jaermann et al., 2006; Wang, 2012).

Second, the simultaneous multi-slice (SMS) acceleration approach is a powerful way to reduce scan time by simultaneously exciting and acquiring data from multiple slices.

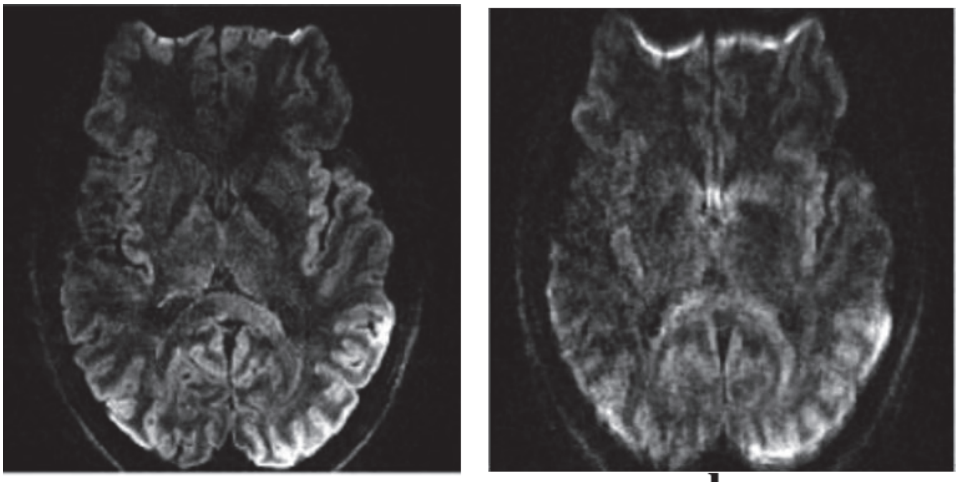

Figure II.4 : Direct comparison of diffusion MR data acquired using the 2D-readout-segmented EPI pulse sequence with simultaneous multi-slice acquisition (a), and the gold standard single-shot EPI pulse sequence (b) at 7 T ((Frost et al., 2015).

Frost et al. have implemented and used the simultaneous multi-slice (SMS) acceleration method in conjunction with the 2D-rsEPI pulse sequence to perform dMRI with reduced scan time as well as to minimize distortion and blurring artifacts (Frost et al., 2015). Diffusion-weighted DW-images

of 30 slices were encoded in three diffusion directions as well as one volume without diffusion-weighting. The dMRI data were acquired at a 3T scanner with a spatial resolution of 0.9mm x 0.9mm x 4mm and 11 in-plane 2D-rsEPI segments in 3 minutes.

In addition, the potential of a 2D-rsEPI dMRI pulse sequence with SMS to perform high-quality DW images with an isotropic spatial resolution of 1.2 mm was demonstrated at an ultra-high field of 7T (Frost et al., 2015). The obtained data show improvement in anatomical detail and a low level of distortion and blurring compared with the classic 2D-ssEPI method. Figure.II.4 shows an example of the obtained data at a b-value of 1000 s/mm^2.

I.3.3. 2D Multi-Shot EPI (2D-msEPI) dMRI pulse sequence

Similar to 2D-rsEPI dMRI method, the 2D phase-segmented EPI, also called the 2D multishot-EPI (2D-msEPI) dMRI pulse sequence, has been widely used for *in-vivo* dMRI studies. Basically, the 2D-msEPI has been proposed to alleviate the issues of the classic 2D-ssEPI pulse sequence and to improve the quality of the dMRI data. In fact, the 2D-msEPI acquisition scheme segments the k-space in multiple shots in the phase encoding direction, thus minimizing the TE and the ETL and then image distortions as well as enhancing the SNR and the spatial resolution.

However, the 2D-msEPI approach requires a long scan duration to fully complete the k-space lines sampling. Furthermore, the 2D-msEPI suffers from ghosting artifacts induced by the shot-to-shot phase variations mainly due to head rigid body motion and to CSF pulsation.

Several studies have investigated the motion-induced ghosting artifacts in 2D-msEPI and have proposed various acquisition schemes with embedded low-resolution navigator echo to address and minimize the inter-shot phase variations (Bammer et al., 1999; Butts et al., 1996; Ordidge et al., 1994). However, the navigator echo-based correction method could fail if the motion differs between the navigation and the imaging MR data.

On the other hand, an alternative correction method based on a computation algorithm in post-processing without a navigator echo has been proposed to estimate and correct the linear and nonlinear phase variations (Miller and Pauly, 2003). In addition, Chen et al. proposed a reconstruction algorithm, called multiplexed sensitivity encoding (MUSE), to inherently correct

and address the motion-induced shot-to-shot phase variation without using the navigator echo (Chen et al., 2013).

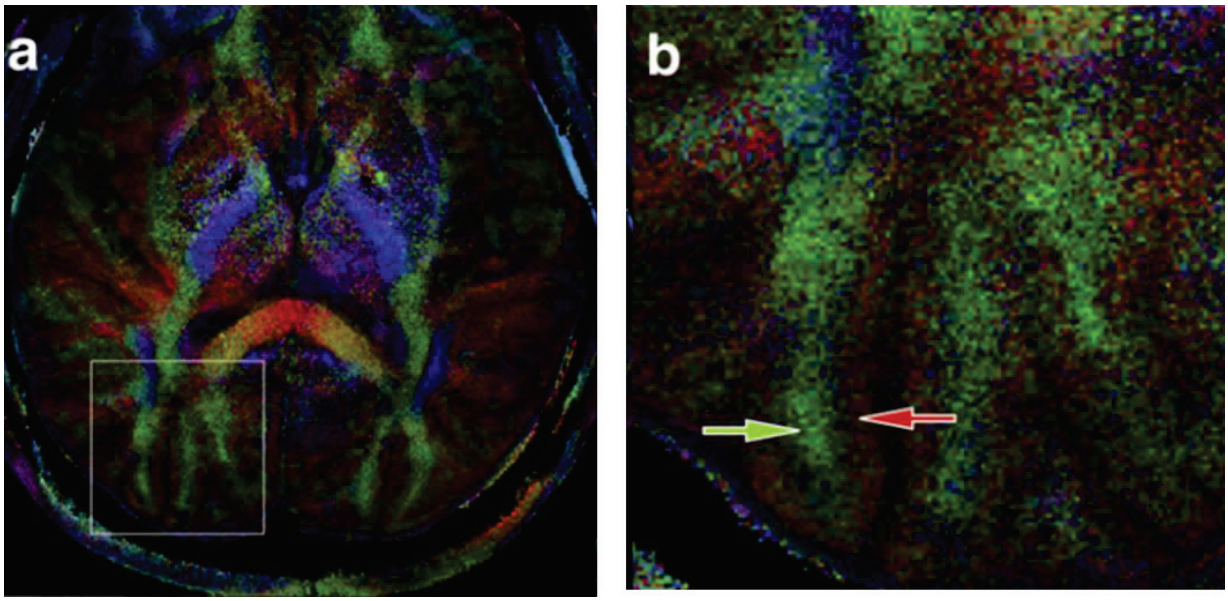

Figure II.5: The data with an in-plane spatial resolution of 0.3mm x 0.3mm, acquired with the 2D-msEPI and reconstructed with MUSE (Chen et al., 2013).

The performance of the proposed method was demonstrated by the capability to improve the spatial resolution and reduce the motion-induced artifacts in cerebral dMRI data. The acquired data set consisting of 15 diffusion-weighted images at a b-value of 500 s/mm^2 and 4 baseline volume at a b-value of 0 s/mm^2. The in-plane spatial resolution was set to 0.3 mm x 0.57 mm; however, the slice thickness was set to 8 mm (Fig.II.5). The k-space was sampled through four 2D-EPI segments. The dMRI experiments were performed using a 3T scanner and an 8-channel coil.

In addition, Liu et al. proposed to combining 2D-msEPI with parallel imaging-based reconstruction method to increase the spatial resolution and to address the inter-shot phase variation effects (Liu et al., 2016). *In-vivo* cerebral dMRI data were acquired at a 1.5 T scanner and using an 8-channel head coil with the in-plane spatial resolution of 0.93 mm x 0.93 mm, whereas the slice thickness was set to 6 mm. The proposed acquisition and reconstruction pipeline allows generation of cerebral dMRI images with visibly reduced ghosting artifacts compared to data reconstructed using the classic Fourier Transform method (Fig.II.6).

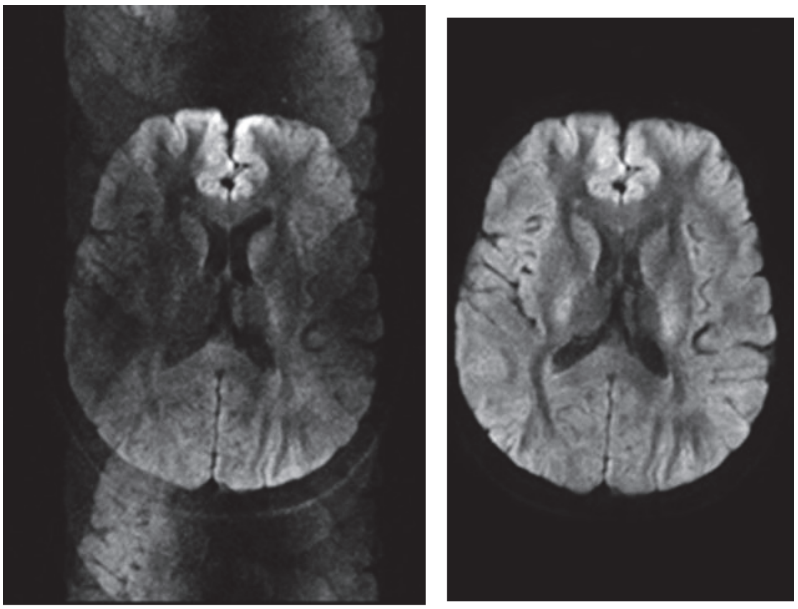

Figure II.6: Direct comparison of dMRI data acquired using the 2D-msEPI acquisition method and reconstructed with (a) the classic Fourier transform and (b) the proposed parallel imaging-based reconstruction method (Liu et al., 2016).

I.3.4. 3D-ssEPI dMRI pulse sequence

Numerous studies have presented the three-dimensional single-shot EPI (3D-ssEPI) sampling scheme of Fourier space as an alternative approach for obtaining high-quality cerebral dMRI data. In fact, the 3D-encoding of the Fourier space allows enhancement of the sensitivity of the diffusion MRI acquisition, leading to an increase in the SNR efficiency. The validity of the 3D-dMRI approach to perform high resolution with high SNR has been demonstrated previously on small animal brains such as those of mice (Xue et al., 2001) and on the *post-mortem* macaque brain (Feng et al., 2017).

Golay et al. used for the first time the 3D-ssEPI acquisition method to perform dMRI data on the *in-vivo* human brain (Golay et al., 2002). In comparison with the 2D-ssEPI dMRI pulse sequence, Golay's study shows that the 3D-ssEPI allows improvement of the spatial resolution and the obtained SNR of cerebral dMRI. An isotropic spatial resolution of 1.5mm x 1.5mm x 1.5mm was

achieved before applying the zero-filling, resulting in an isotropic voxel size of 0.8 mm x 0.8mm x 0.8mm. Six diffusion-weighted images as well as a reference image were acquired in ~8 minutes. The dMRI experiment was performed using a 1.5T MR scanner and a receive-only surface coil. Figure II.7 shows the obtained diffusion-weighted 3D-ssEPI data of the dorsolateral parietal cortex.

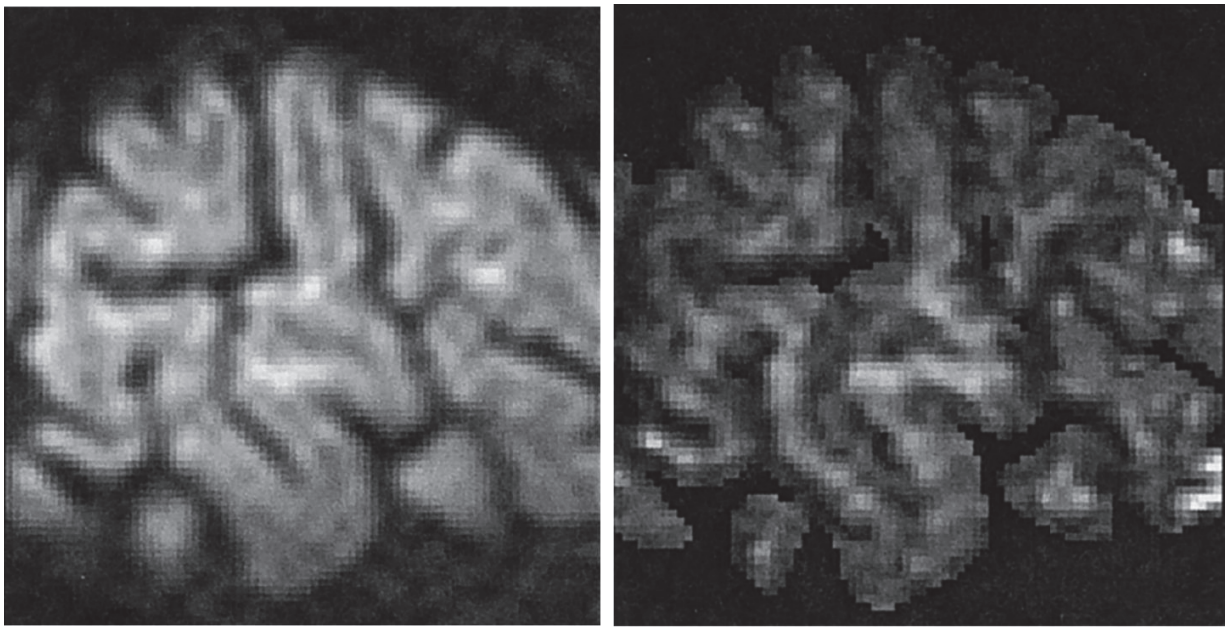

a **b**

Figure II.7: Diffusion MRI data of the dorsolateral parietal cortex acquired with the 3D-ssEPI method at a 3T scanner (Golay et al., 2002).

Other studies have demonstrated that the use of the 3D-ssEPI sampling scheme is strongly beneficial to achieve a higher spatial resolution and to significantly improve the SNR of cerebral dMRI in comparison with the typical 2D-ssEPI dMRI method (Engström and Skare, 2013). However, practical considerations should be given with regard to the needed scan duration, which remains incompatible with the typical examination time for a clinical condition. Therefore, this makes it challenging to perform dMRI data with a higher number of diffusion encoding directions and/or to perform multi-shell dMRI data. Thereby, several acquisition schemes have been proposed recently to shorten the scan time of 3D-ssEPI dMRI acquisition.

The multislab method has been widely used for dMRI human studies in order to accelerate acquisition time, enabling achievement of higher spatial and angular resolution in acceptable time.

Engström et al. have used the 3D multislab-ssEPI pulse sequence for acquiring dMRI data on the *in-vivo* human brain (Engström and Skare, 2013). In this work, they demonstrated that the 3D multislab approach provides high dMRI data quality in acceptable scan time. Indeed, an isotropic spatial resolution of 1.3mm x 1.3mm x 1.3mm was achieved as well as a good SNR level using a 3T MRI scanner and an 8-channel head coil. The diffusion-weighted data were encoded along 45 directions in 40 minutes (Fig. II.8).

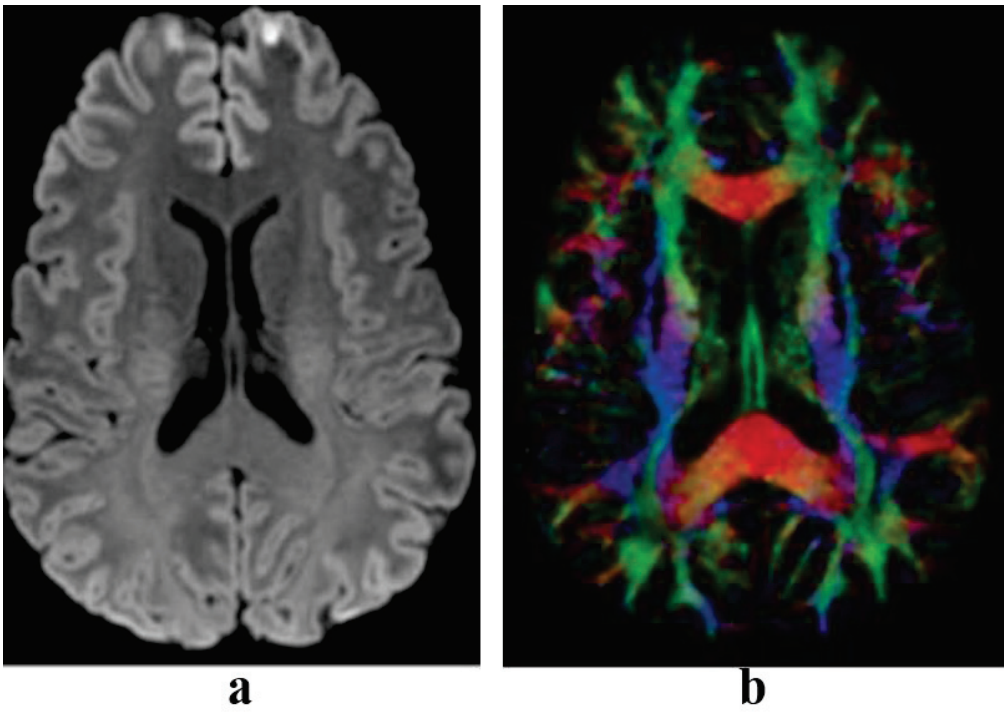

Figure II.8: 3D multislab-ssEPI dMRI data acquired with isotropic resolution of 1.3mm (a): axial diffusion weighted, (b): color-coded FA map (Engström and Skare, 2013).

In addition, to push the 3D multislab-ssEPI approach to its limits, it was combined with an ultra-high field, i.e. 7T, to further improve the SNR without increasing the scan time. Wu et al. described the achievement of an isotropic spatial resolution of 1 mm^3 of dMRI data acquired on the *in-vivo* human brain. Eight non-diffusion-weighted images as well as 64 diffusion-weighted images with a b-value of 1500 s/mm^2 were acquired in 35 min (Wu et al., 2016b) (Fig.II.9).

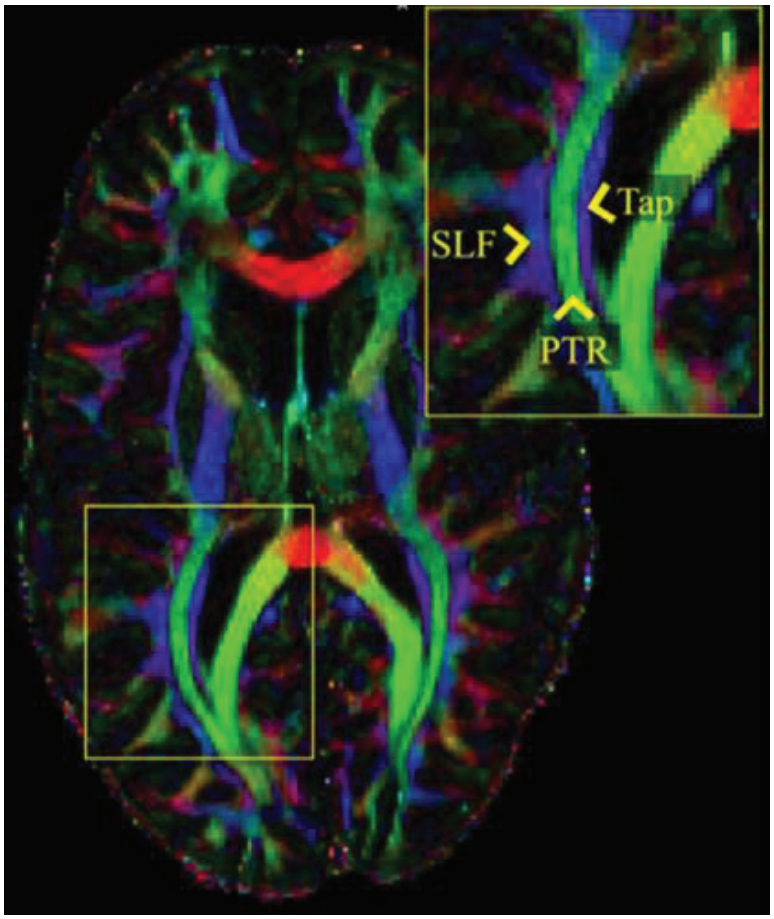

Figure II.9: Color-coded FA map, obtained using 3D multislab-ssEPI dMRI pulse sequence with an isotropic spatial resolution of 1 mm^3, allows delineation of the fine-scale anatomical structures as shown in the zoomed box (Wu et al., 2016).

I.3.5. 3D-msEPI dMRI pulse sequences

Recently, Chang et al. reported the achievement of an isotropic spatial resolution of 0.85 × 0.85 × 0.85 mm of *in-vivo* dMRI on the human brain at a 3 T clinical scanner and used an 8-channel head coil (Chang et al., 2015b) (Fig.II.10). The Chang et al. study demonstrated that such resolution could be reached by combining the 3D-msEPI encoding of the Fourier space in order to enhance the SNR and the sensitivity of the dMRI acquisition with the multishot sampling scheme to increase the spatial resolution.

In addition, the 2D-navigator echo correction approach has been used to estimate and correct the shot-to-shot phase variation. In this study, twelve diffusion-weighted volumes were acquired with a b-value of 800 s/mm^2 in 96 minutes. The added value of the achieved spatial resolution was assessed by comparison with a dataset with a spatial resolution of 2mm x 2mm x 2mm commonly used for human dMRI (Fig.II.10.b). The low-resolution data were generated by downsampling the high-resolution dataset.

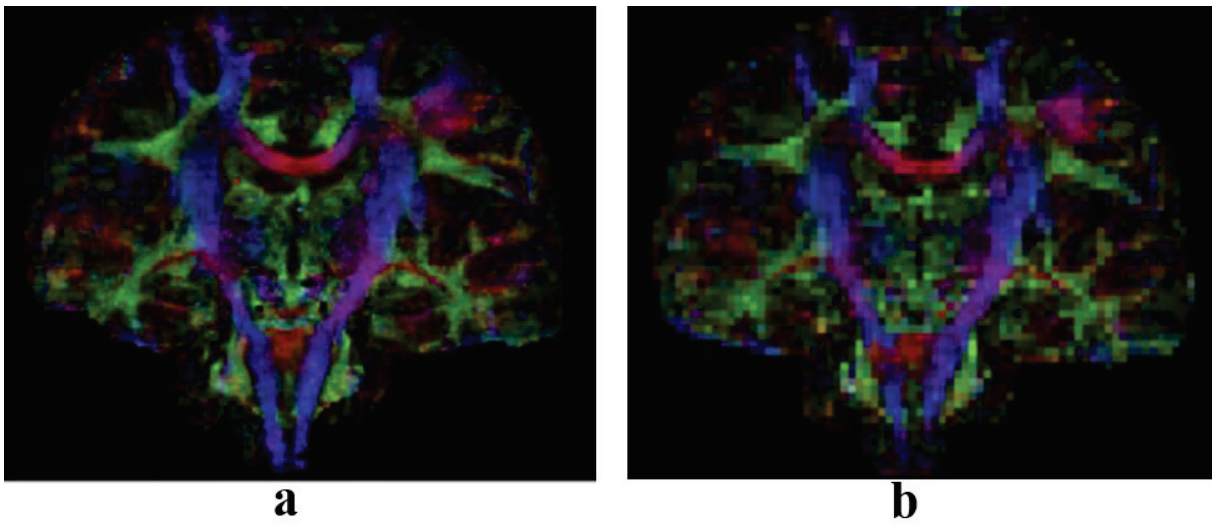

Figure II.10: Direct comparison of color-coded FA-maps with isotropic spatial resolutions of 0.85 mm obtained using 3D-msEPI dMRI pulse sequence (a) and of 2 mm generated by downsampling the high-resolution data (b) (Chang et al., 2015).

Last, to delineate and analyze the fine-scale anatomical features as well as to describe the thin cerebral connectivity such as the cortical white-grey matter fibers, higher spatial resolution is certainly desired. Setsompop et al., demonstrated the achievability of dMRI data with an isotropic spatial resolution of 0.66 mm. This significant achievement was realized by the combination of a zoomed 3D multislab-ssEPI sampling scheme with SMS approach (Setsompop et al., 2018). I*n-vivo* cerebral dMRI data have been collected in a 3T MRI scanner with a maximum gradient strength of 300 mT/m and a custom-built 64-channel head coil. An isotropic spatial resolution of 0.66mm x 0.66mm x 0.66mm was achieved using the following parameters: TE = 80ms; echo spacing 0.32 ms; FOV =220 x 118 x 151.8 mm^3; ETL ~=42 ms (178 lines x 6/8 partial Fourier x

0.32 ms). Four averages of 64 diffusion-weighted volumes with a b-value of 1500 s/mm^2 as well as 6 non-diffusion-weighted volumes were carried out in 100 minutes (Fig.II.11).

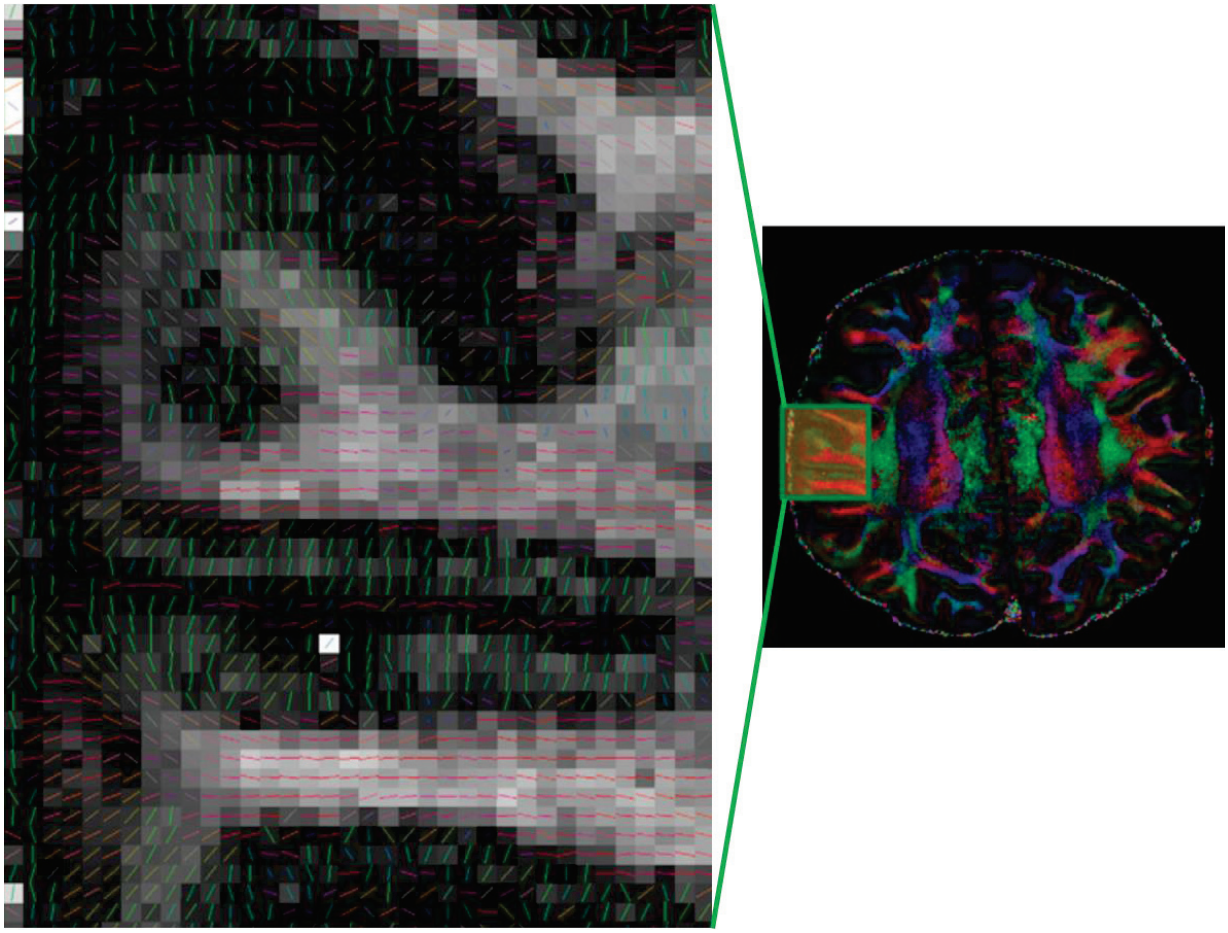

Figure II.11: Color-coded FA map obtained in-vivo at a spatial resolution of 0.66 mm dMRI data shown on the right and the zoom-in of the tensor result shown on the left (Setsompop et al., 2018).

I.4. In-vivo non-human primate brain dMRI

As demonstrated above, the small size of the macaque brain and the low sensitivity of the diffusion MRI acquisition are the major challenges faced to perform high-resolution dMRI on anesthetized macaque brains using a clinical MR scanner. Several methodological developments in the field have been carried out in order to overcome the technical challenges associated with dMRI acquisition and the use of the classic pulse sequence for *in-vivo* dMRI study.

I.4.1. Anesthesia and subject setup

DMRI acquisitions are often performed on anesthetized non-human primates to avoid artifacts induced by random rigid-body motion. The choice and dosage of the anesthetic depend on the physiological status of the NPH and the duration of the dMRI acquisition. The common choices of anesthesia are sevoflurane, propofol and ketamine.

Isoflurane is the anesthetic agent commonly adopted for long *in-vivo* dMRI exams (>1h). The concentration of the volatile inhalation agent is adjusted according to the purpose of the study and to the physiological condition of the subject. Often, isoflurane concentration from 0.5% to 2% mixed with oxygen (O_2) is used in the *in-vivo* MRI exams. The effects of isoflurane on cerebral blood flow (CBF), cerebral blood volume (CBV) and neuron functionality have been investigated in several studies in humans (Oshima et al., 2003) and animals (Kimme et al., 2007; Masamoto et al., 2009). Li et al. have demonstrated that the high concentration of the isoflurane resulted in an increase of global CBF and a decrease of blood pressure in anesthetized macaque monkeys. A significant increase of CBF in the thalamus and the cerebellum respectively 39% and 55%, occured when the concentration of isoflurane changed from 0.75% to 1.5% (Li et al., 2013).

All of the dMRI exams that are carried out under anesthesia require veterinary support to provide care for animals during the MRI experiment and to monitor the physiological parameters include cardiac and respiration rates as well as oxygen saturation level, expired CO_2 and body temperature. These parameters should be continuously monitored and maintained in the normal range (Li et al., 2013). MR-compatible devices that can record physiological signals are available to be used for NHP exams. The equipment should allow reliable monitoring, and should not produce noise or artifacts in MR images.

In addition, a Kopf MR-compatible stereotaxic frame (Kopf Instrument, Tujunga, CA) is generally used in several MRI studies to immobilize the animal head during the scan. The animals are placed in a sphinx position in the frame where the head position is maintained with a plastic mouth bite bar and two ear bars to avoid any motion.

I.4.2. MR scanner

The majority of the cerebral dMRI examinations on non-human primates are carried out using a clinical MR machine, i.e., 3 Tesla MR Scanner. Actually, the human scanner is widely used because it allows scanning small and large non-human primates and it uses common MRI protocols on human and non-human primates for the translational aspects of the imaging protocols. In addition, the large diameter of the scanner tunnel enables placing the animal in the required position and installing the monitoring devices to monitor the physiological status of the animal during the anesthesia.

The animal MR scanner has been proposed as an alternative approach to perform very high-resolution diffusion-weighting MRI data. In fact, the animal MR scanner is characterized by a high magnetic field, i.e., 4.7 T, and high gradients performance that are specifically designed for *in-vivo* imaging of small primates such as squirrels and marmosets monkeys (Konomi et al., 2012; Schilling et al., 2017), and could be used for the *ex-vivo* macaque brain.

I.4.3. MR coils

Instead of the high field animal MR scanner, the use of dedicated coils can be a valuable and cost-effective way to improve sensitivity capabilities in MRI. Various types and forms of custom-built non-human primate coils were introduced and used to enhance the resolution and the sensitivity of cerebral dMRI acquisition on living monkeys.

Liu et al. have described the feasibility of performing dMRI on anesthetized monkeys using a 3T human scanner with an isotropic spatial resolution of 1 mm (Liu et al., 2009). A homemade three-channel phased array coil was built and used for monkey brain scan. Diffusion-weighted data were encoded along 24 diffusion directions with a b-value of 700 s/mm^2. In addition, four baseline images with b-value of 0 s/mm^2 were collected using the 2D-ssEPI dMRI pulse sequence. The acquired data were averaged 12 times, resulting in a total scan time of 36 minutes. This study also illustrated that an increase in the spatial resolution provides better diffusion tensor estimations and improves the DTI-based fiber tractography (Fig.II.12).

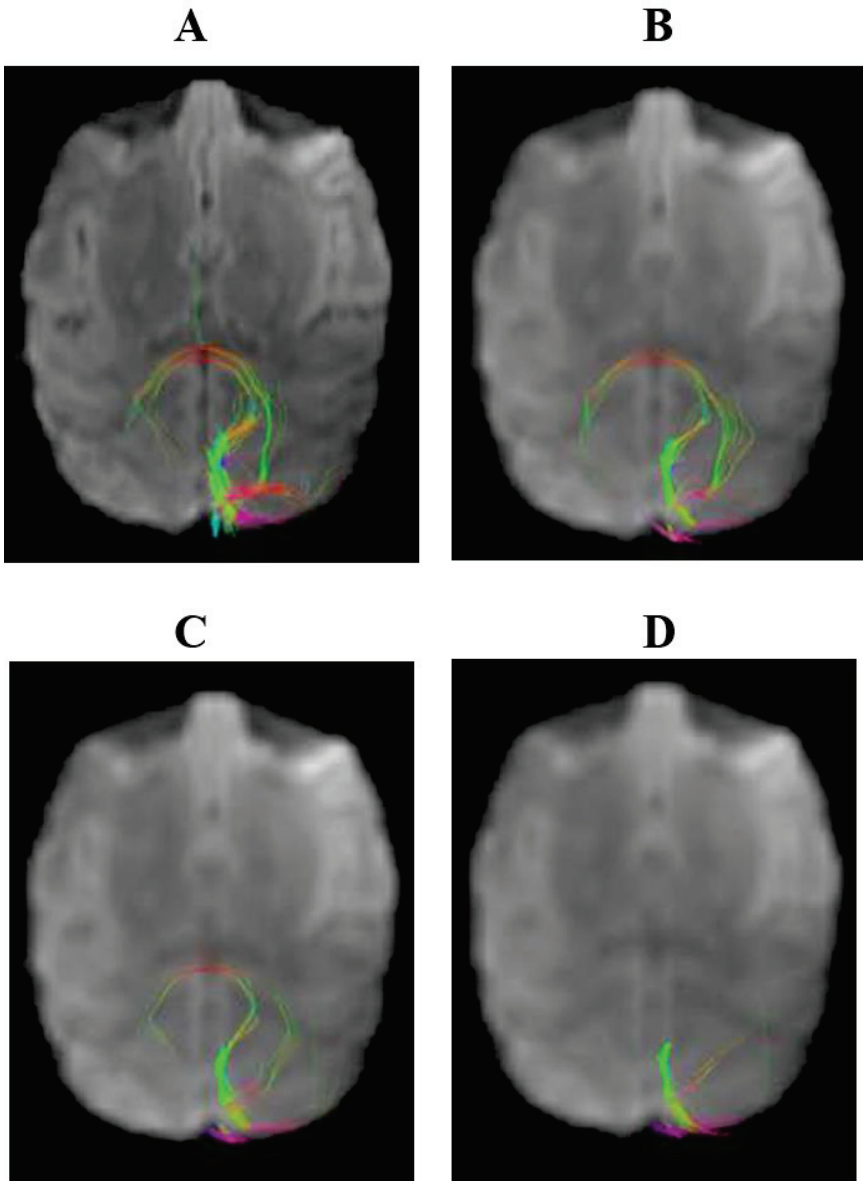

Figure II.12: Results of fiber tracking for the occipital-Callosal pathway in one hemisphere with a high-resolution data of (A) 1 mm, (B) 1.3 mm, (C) 1.5 mm and (D) 1.7 mm, respectively. One can clearly see that with the increase in voxel size, the number of fiber tracts decreases (Liu et al., 2009).

Similarly, Khachaturian introduced a 4-channel phased array coil for dMRI and functional MRI experiments on the *in-vivo* monkey (Khachaturian, 2010). The constructed coil could be used for different Rhesus monkeys because the curvature of the coil fitted the head sizes and the shape of

the monkey head. In addition, a custom-built transmit loop coil was used in conjunction with the 4-channel receive coil (Fig.II.13). A detuning circuit was added to avoid the interference of the transmit coil with the receive coil during the data scan.

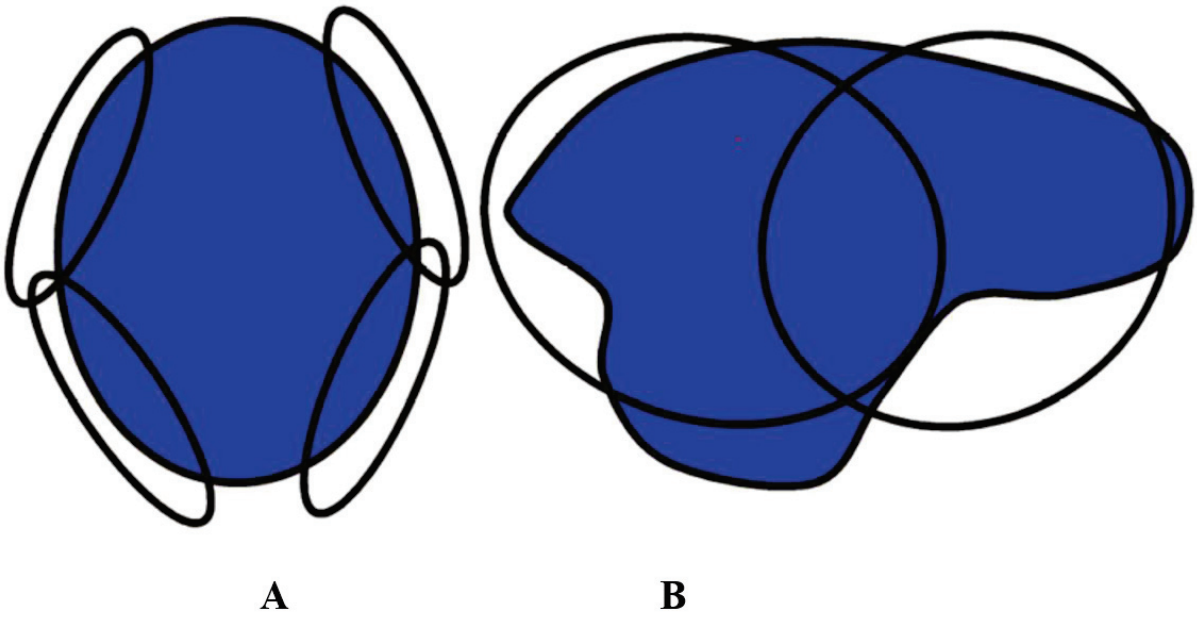

Figure II.13: Schematic of the placement of the 4-channel receive coil relative to the brain from the superior (A) and sagittal (B) views (Khachaturian, 2010).

The proposed coil can provide a signal-to-noise-ratio improvement in the cerebral cortex. Hence, this allows increasing the spatial resolution and achieving an isotropic spatial resolution of 0.9mm x 0.9mm x 0.9mm for dMRI experiments using the 2D-ssEPI method (Fig.II.14). On the other hand, the introduction of the phased array coil enables use of the parallel imaging method, which allows reduction of EPI-related distortions as well as reduction of scan time.

Only one report described the achievement of cerebral dMRI on anesthetized macaque monkeys with a spatial resolution of 0.7 mm isotropic. To achieve this spatial resolution, Janssens et al. have developed an 8-channel array coil, whose loops were surgically implanted directly onto the skull of a macaque monkey to further increase the sensitivity of the diffusion MRI acquisition (Janssens et al., 2012) (Fig.II.15). According to this study, the implemented coil provides an average SNR

gain of ~3 compared to the external 4-, and 8-channel array coil. A significant improvement of SNR was helpful to increase the spatial resolution of dMRI scan up to 0.7 mm × 0.7 mm × 0.7 mm, which corresponds to a voxel size of 0.343 mm^3.

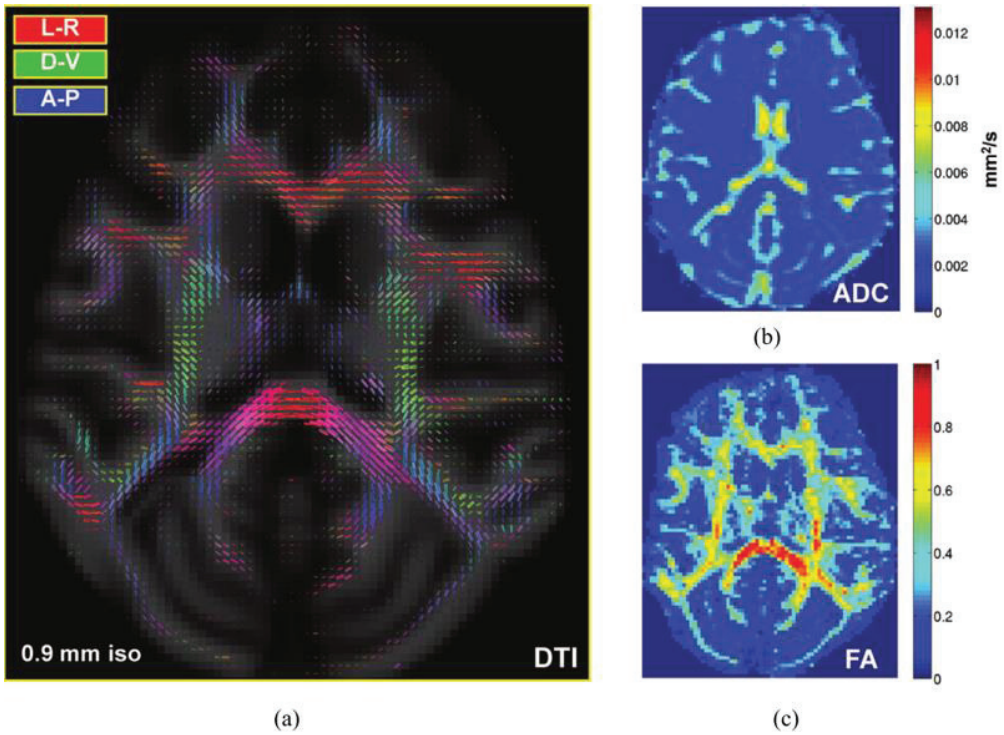

Figure II.14: The obtained (a) DTI, (b) ADC, and (c) FA maps acquired with the phased array coil at 0.9 mm isotropic resolution (Khachaturian, 2010).

The classic 2D-ssEPI dMRI pulse sequence was used with the paralleled imaging technique to accelerate the data acquisition. 256 diffusion-weighted images were collected with such resolution in 3 hours. Figure II.16 shows the axial, coronal and sagittal views of the obtained high resolution FA and color-coded FA map.

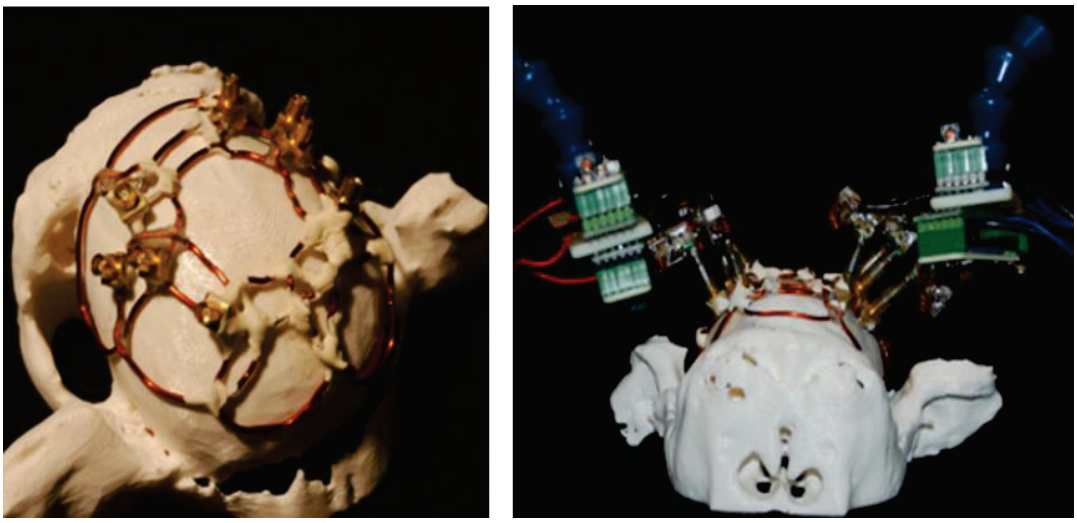

Figure II.15: The implanted 8-channel coil whose loops were implanted directly onto the skull of a macaque monkey (Janssens et al., 2012).

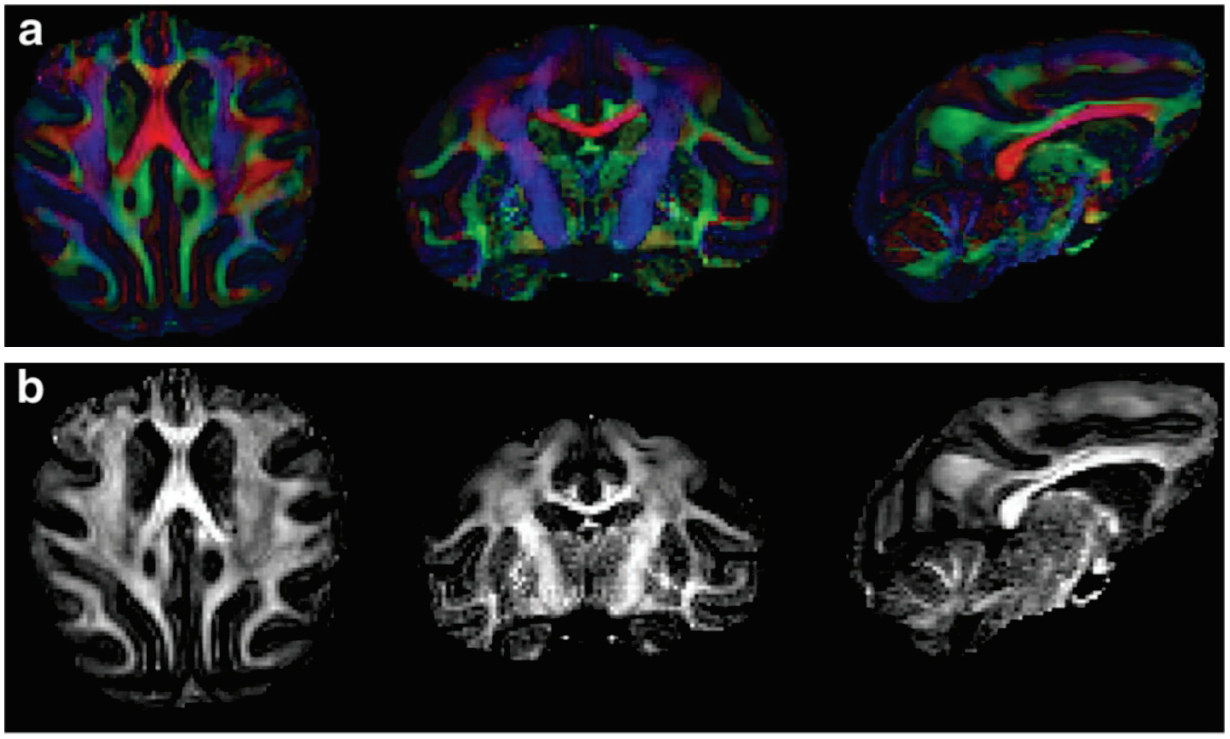

Figure II.16: The axial, coronal and sagittal views of the (a) FA and (b) color-coded FA map acquired with an isotropic spatial resolution of 0.7 mm. The data were acquired invisibly using the implemented 8-channel coil on the macaque monkey in 3 T scanner (Janssens et al., 2012).

The Objective

In this study, a dMRI acquisition approach was developed and used to address the technical challenges related to the use of the classic EPI-based MR pulse sequence under a clinical MR scanner, and to improve the spatial resolution reached for cerebral dMRI data performed on living non-human primates. The main purpose of this work is to demonstrate the non-invasive feasibility of diffusion-weighted images with an isotropic resolution of 0.5 mm on anesthetized macaques at a 3T MR Scanner.

This target resolution is three times higher in term of voxel size (0.5 mm × 0.5 mm × 0.5 mm = 0.125 mm^3) than that achieved invasively by the team of Janssens using an 8-channel coil surgically implanted onto the skull of a macaque monkey (Janssens et al., 2012).

In this context, a homemade dMRI pulse sequence based on three-dimensional multi-shot Echo Planar Imaging (3D-msEPI) was implemented on a 3T human clinical scanner. The proposed Fourier-space sampling scheme was associated with optimal scan parameters to reduce susceptibility artifacts and improve the signal-to-noise-ratio of dMRI data. A full description of the proposed method is available in the next Chapter, "***High Resolution Cerebral DMRI Using 3D-EPI".***

To evaluate the effectiveness of the proposed approach, it was compared to the commonly used 2D-ssEPI dMRI pulse sequence and to the 2D-msEPI dMRI pulse sequence.

Last, the added value of the cubic 0.5 mm spatial resolution of dMRI data compared to more standard resolutions was illustrated by showing the capacity of the high-resolution data to delineate the fine-scale brain structures at anatomical level and by tractography.

Chapter III. High-Resolution Cerebral dMRI Using 3D-EPI

Introduction

As presented in Chapter I, dMRI acquisition is typically conducted using the classic 2D-ssEPI pulse sequence due to its ease of use in human and non-human protocols as well as its wide availability on all clinical scanners.

However, several challenges exist to perform high-resolution cerebral dMRI on *in-vivo* macaque monkeys or on the human brain due mainly to the technical limitations related to the use of the 2D-ssEPI pulse sequence, including its low spatial resolution, off-resonance effects, and susceptibility-induced image distortions.

The goal of this study is to demonstrate the feasibility of performing high spatial resolution cerebral dMRI data on anesthetized macaques and on humans. For that purpose, two acquisition approaches were implemented on a 3T MR clinical scanner. The developed methods are based on 3D encoding of Fourier space with 1) An in-plane single-shot EPI sampling scheme, called 3D-ssEPI dMRI pulse sequence and 2) An in-plane multi-shot EPI sampling scheme, termed the 3D-msEPI dMRI pulse sequence. The proposed acquisition methods are expected to:

- Improve the sensitivity of the dMRI acquisition by the 3D sampling scheme of the Fourier space.
- Improve the reached spatial resolution and reduce EPI-related artifacts such as blurring and geometric distortion by acquiring shorter echo train, using the msEPI or the parallel imaging technique with ssEPI.

Echo Planar Imaging pulse sequence

I.1. Spin Echo EPI pulse sequence

The Spin Echo-Planar Imaging (SE-EPI) pulse sequence typically uses an RF excitation pulse of 90° simultaneously with the slice-selection gradient applied along the z-axis to spatially select a narrow slice (see Chapter I). Once the RF transmitter is turned off, the excited spins lose coherence rapidly due to T_2^* relaxation, resulting in a decrease of the net transverse magnetization. After a delay of TE/2, an additional RF pulse of 180° is applied to rebuild the coherence of spins, allowing

the transverse magnetization to reappear and create an echo at a specific moment called the *echo time* (TE).

After the refocusing pulse, multiple or entire Fourier-space lines needed for image reconstruction are acquired using a train of bipolar oscillating readout gradients to produce multiple gradient echoes called the echo-train. Each gradient echo is individually phase encoded using a phase encoding gradient blip for line-to-line displacement in the Fourier space. The number of the acquired Fourier-space lines after each RF excitation pulse is called EPI-Factor (EF).

The delay separating two adjacent echoes is called the echo spacing (ES) and it depends on many factors such as the bandwidth, gradient performance (i.e. slew rate, amplitude) and the matrix size along the readout direction. The EF and ES together determine the measurement time and the minimum achievable TE, corresponding to the scan time needed to reach the central line of k-space.

The total scan time needed for a single slice imaging is the same as the sequence length "T_{seq}" and it is given by the following equation:

$$T_{seq} = \tau + (ES * EF) \tag{3.1}$$

where τ is the delay between the start of the sequence and the beginning of the first echo acquisition. Therefore, for multi-slices acquisition (i.e. N slices), the minimal total scan time "T_{scan}" can be written as follows:

$$T_{scan} = (N * T_{seq}) = N * (\tau + (ES * EF)) \tag{3.2}$$

I.2. Gradient Echo-EPI pulse sequence

The gradient echo EPI (GE-EPI) pulse sequence follows the same principles as for the SE-EPI explained above. It uses a slice-selection gradient and an excitation RF pulse to create a free induction decay (FID) signal. Then, a train of bipolar readout gradients combined with phase encoding gradient blips are used to spatially encode the produced gradient echoes under the envelope of the FID. The MR signal amplitude decays exponentially with the time constant T^*_2.

I.3. Diffusion-weighted EPI pulse sequence

The diffusion-weighted imaging is sensitizing the acquired MR signal to the diffusion of water molecules. This is can be achieved by adding high strength gradient pulses on either side of the refocusing RF pulse of an SE pulse sequence (Stejskal and Tanner, 1965).

For an accurate quantification of water molecules in the space, the water molecules diffusivity should be assessed along several non-collinear diffusion encoding directions. At least six directions are required for diffusion modeling using the mathematic model called the Tensor (Basser and Pierpaoli, 1998) (see Chapter I).

However, the feasible total scan duration of the diffusion-weighted acquisition determines the number of the diffusion directions that can be encoded. Currently, the 2D multi-slice single-shot EPI (2D-ssEPI) is typically chosen in dMRI studies for its high temporal resolution compared to the classic MR pulse sequences. Indeed, the acquisition speed of this method is highly beneficial, to measure diffusion in multiple directions in an acceptable scan duration. The typical pulse sequence and the resulting Fourier-space sampling scheme are shown in Figure III.1.

The introduction of advanced acquisition strategies such as the High Angular Resolution Diffusion Imaging (HARDI) (Tuch, 2004), which requires a higher number of diffusion encoding directions(>45), leads to an important increase in the total scan time.

Therefore, additional acceleration strategies are increasingly needed to achieve high temporal and high angular dMRI acquisition within an acceptable scan duration. Currently, Partial Fourier (PF) acquisition as well as more advanced techniques such as the parallel imaging approach and the simultaneous multislices acquisition are widely involved in EPI-based imaging protocol to significantly reduce the scan time and to address the EPI-related artifacts.

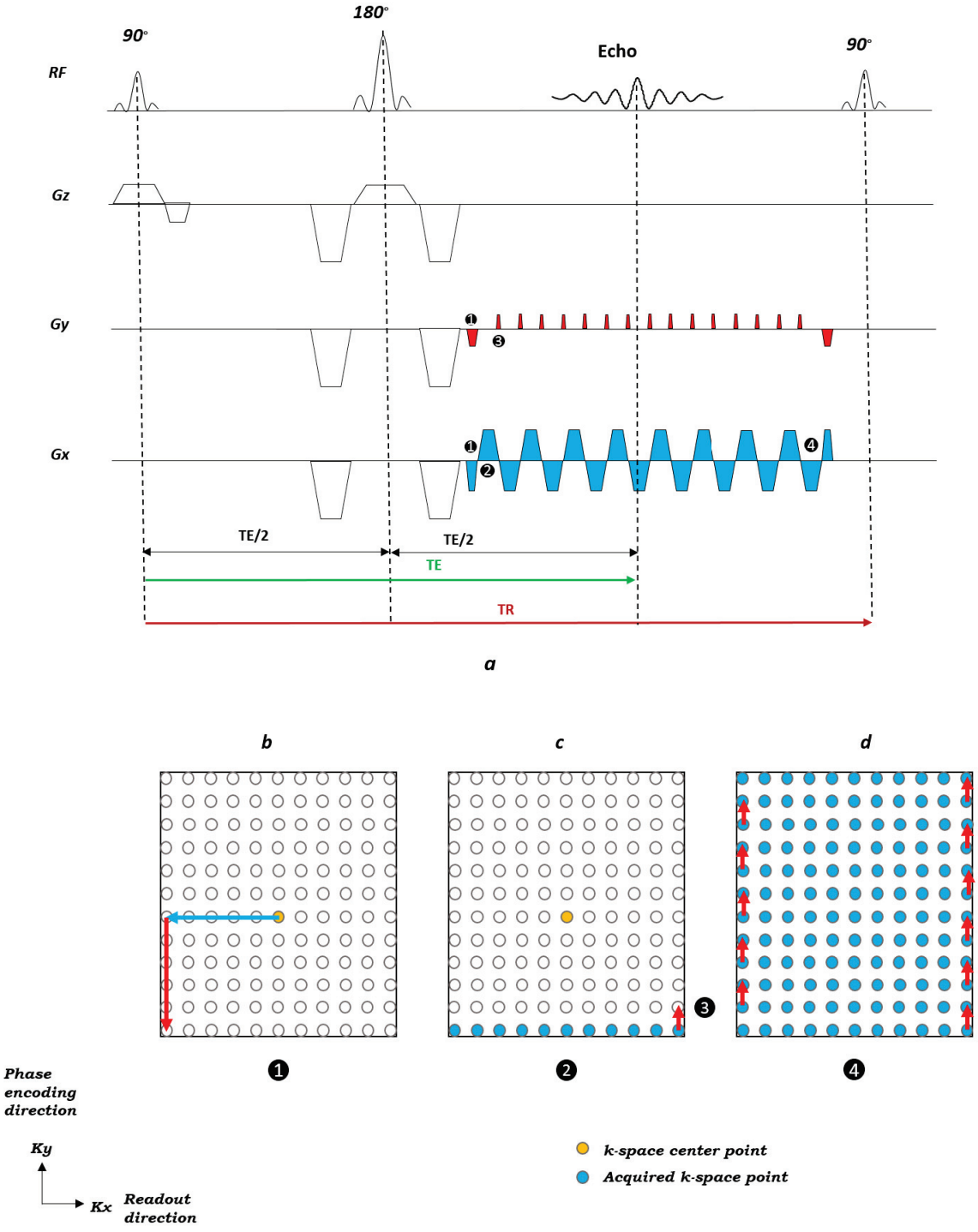

Figure III.1: Diagram of Diffusion-weighted EPI pulse sequence (a), and the resulting k-space sampling scheme (b, c, and d).

EPI Artifacts

Despite its acquisition speed, the ssEPI pulse sequence is prone to several artifacts that deteriorate the quality of the obtained images. Indeed, the low bandwidth along the phase encoding direction and the magnetic field inhomogeneity are the main reasons for geometrical and intensity distortions. Although significant improvements in MR scanners have been made and advanced acquisition approaches have been developed, various artifacts such as susceptibility as well as T_2^* blurring still affect the EPI images.

I.4. EPI-related artifacts

I.4.1. T_2^*-induced image blurring

Acquiring multiple or the entire Fourier-space lines using the ssEPI pulse sequence requires a long echo train, leading to a reduced SNR and a high level of geometric distortions that affect the reconstructed images. Indeed, during the EPI readout the acquisition of the MR signal is performed under the exponential decaying of signal amplitude with time constant T_2^*. Therefore, a significant signal loss occurred at the outer Fourier-space edge due to the long ETL used, resulting in highly pronounced distortions and image blurring. This is particularly problematic for high-resolution ssEPI scans where the number of Fourier-space lines in the phase encoding direction and/or Fourier-space points in the readout direction is further increased compared with the standard resolution scans, resulting in longer ETL.

Several techniques have been proposed to address image blurring in EPI, including the restriction of the readout duration by reducing ETL. Indeed, Parallel Imaging is the typical approach that can help alleviate the T_2^* decay effects by shortening the echo train without deteriorating the achievable spatial resolution. For example, for an acceleration factor of 2, parallel imaging reduces the ETL by half, resulting in considerable reduction of scan duration and image distortions, but with an SNR penalty.

I.4.2. Chemical-shift artifact

The chemical shift refers to the difference in the resonant frequency of molecules due to the molecular environment and the magnetic field inhomogeneity. Indeed, fat protons are experienced

to a slightly weaker local magnetic field and will resonate at a different frequencies than water protons. The chemical difference between water and fat has been calculated to be in the range of 3.5 parts per million (ppm) (Fig.III.2). Therefore, at 3T for example, this corresponds to a frequency difference of $\Delta f = (128 \times 10^6) \times (3.5 \times 10^{-6}) = 440$ Hz, where 128 MHz is the Larmor frequency of protons at 3T.

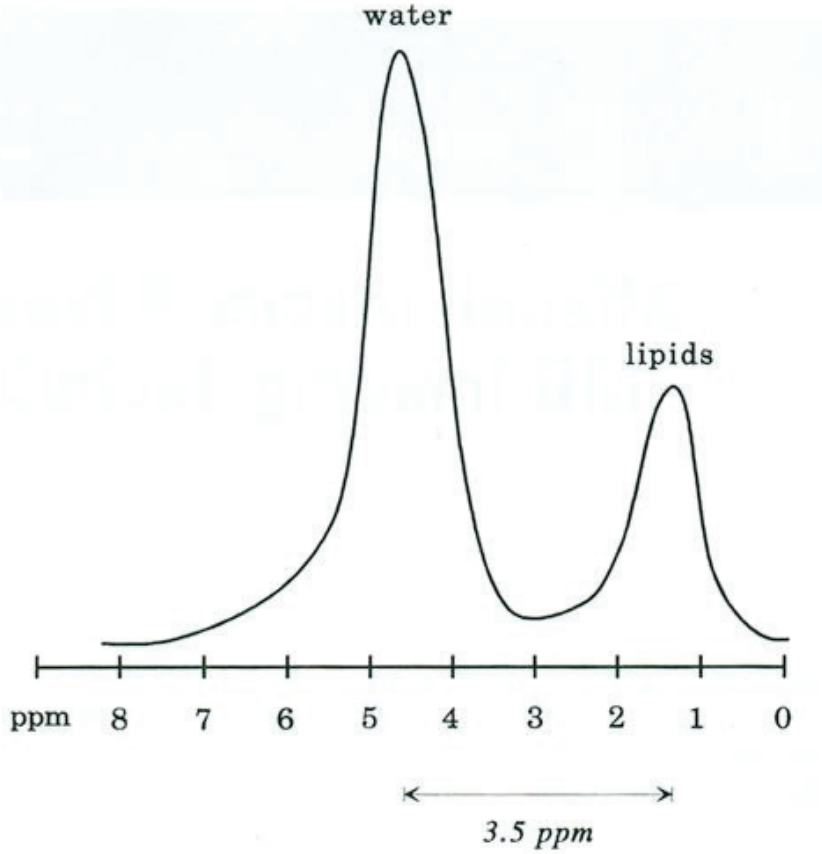

Figure III.2: MR Spectral peaks for fat and water. The average chemical shift difference is about 3.5 ppm.

The fat signal shift due to the chemical shift artifact can be estimated using two acquisition parameters: the receiver bandwidth and the matrix size. For example, for a total receiver bandwidth of 32 kHz and 256 pixels, the bandwidth per pixel is 32000/256 = 125 Hz. The fat-water frequency difference at 3T is about 440 Hz; the chemical-shift artifact size is computed as follows: (440 Hz) ÷ (125 Hz/pixel) = ~4 pixels.

The fat protons component of the MR signal has a lower frequency than water protons if they coexist in the same voxel. This induces a shift of the fat signal to another voxel in the final reconstructed image.

In routine brain diffusion imaging, only a signal of the water proton is expected, whereas the fat signal is simply suppressed. Various fat-suppression techniques exist and can be used prior to the imaging RF pulse, including fat-saturation pulses and Inversion Recovery (IR) preparation. However, for an effective chemical shift artifact mitigation using these methods, a good magnetic field homogeneity is highly desired to better resolve the frequencies of water and fat.

I.4.3. Nyquist ghosting artifact

The ghosting artifact, also called Nyquist N/2 ghost, is a typical artifact of the ssEPI pulse sequence (Porter et al., 1999). The bipolar readout gradients oscillation leads to systematic phase inconsistencies between even and odd echoes. This induces the misalignment of forwarded and backward echoes, giving rise to Nyquist ghosts in final reconstructed images (Bruder et al., 1992). The misalignment may arise for many reasons such as eddy currents, static field inhomogeneities and inaccurate timing of the readout gradients (Fig.III.3).

Various correction methods based on post-processing and/or on reference scan (Bruder et al., 1992) have been proposed to address the Nyquist ghost artifacts. The reference scan approach consists of acquiring a few gradient echoes, i.e. three echoes, at the k-space center without using phase encoding gradient. Then, the acquired echoes will be used as a reference to measure the phase shift information and subsequently align the imaging k-space lines.

In this manuscript, a reference-based approach was used to acquire reference data with phase encoding gradients disabled for Nyquist ghosting correction. A detailed description of the implemented method is provided below.

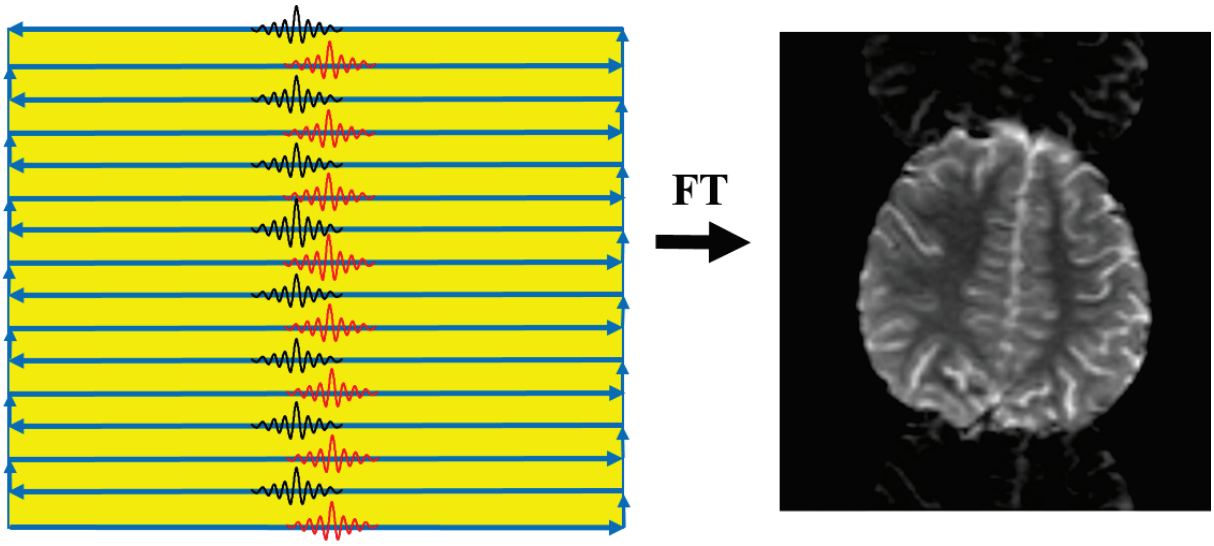

Figure III.3: The misalignment of forwarded and backward echoes (left) resulting in "Nyquist N/2 ghost" in the final reconstructed image.

I.4.4. Image distortion

The ssEPI technique is known by its low bandwidth per pixel in the phase encoding direction, i.e. the bandwidth per pixel is <20 Hz for a typical echo spacing of 0.5 ms and a classic matrix size of 128 pixels. Additionally, the homogeneity of the local magnetic field varies rapidly across distance, e.g., the patient's head, and even within an individual image voxel. Therefore, the frequency variation induces signal dropout from T_2^*-dephasing, resulting in spatial displacement of voxels in the reconstructed image (Fig.III.4.a).

Actually, the susceptibility-induced voxel dislocation is more pronounced in the phase encoding direction, whereas it is negligible in the readout direction due mainly to the relatively high bandwidth (>1000 Hz). So the pixel shift in the phase encoding direction induced by susceptibility artifacts in EPI can be written as follows:

$$\rho = \rho_0 + \left(\frac{\Delta\nu_\rho}{BWP_\rho}\right) \tag{3.3}$$

where ρ is the pixel position after phase shifting and ρ_0 is the correct position. $\Delta\nu_\rho$ and BWP_ρ are, respectively, the spatial distribution of the spatial frequency in Hz and the bandwidth per pixel in the phase encoding direction in Hz.

In addition, the produced susceptibility-induced distortions are more pronounced at ultra-high field (UHF). Several ways have been proposed to minimize image distortions in echo planar images, including using shorter ETL by increasing the bandwidth along the phase encoding direction using the multishot acquisition scheme. Moreover, the parallel imaging could be used with ssEPI acquisition to reduce the echo train length and address the image distortions (Fig.III.4.b).

Another means for distortion correction consists of acquiring a B_0 map and unwrapping the image through a phase correction (Jezzard and Balaban, 1995). The artifacts shape could be changed by permuting the phase and frequency encoding directions.

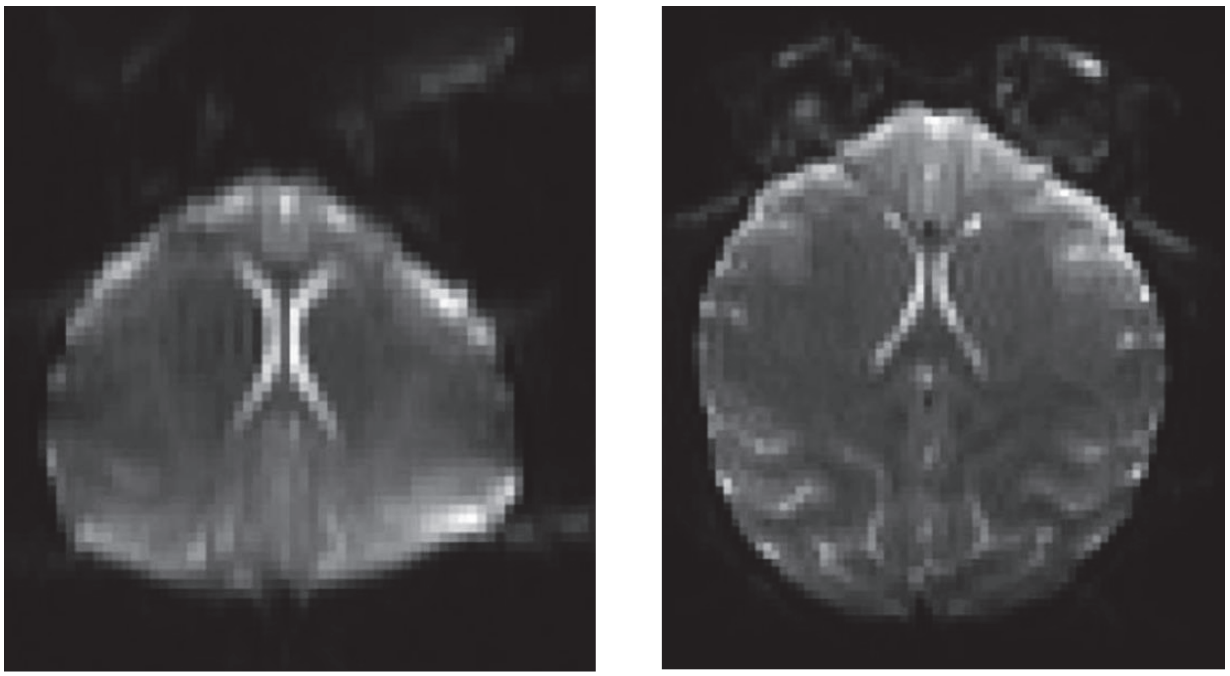

Figure III.4 : Susceptibility-induced distortions in EPI induced by long ETL (a) and the reduced distortion using parallel imaging with acceleration factor of 2 (b) (from (Liu et al., 2010)).

I.4.5. Intravoxel dephasing

The magnetic field varies from place to place even at a submicroscopic scale. Therefore, the spins are experienced to a different local magnetic field and will resonate at different frequencies

depending on the molecular environment and tissue types. The off-resonance effects are worse at the interface of different tissue types such as tissue-air and cause signal loss in these regions. Intravoxel dephasing appears when field inhomogeneities occur within a single voxel in echo planar images, resulting in signal loss induced by intravoxel phase dispersion.

Parallel imaging can be used to mitigate the intravoxel dephasing artifact by reducing the duration of the sampling trajectory. In addition, acquiring a thinner slice could be an effective way to avoid signal loss, resulting in improvement of the overall SNR (Fig.III.5).

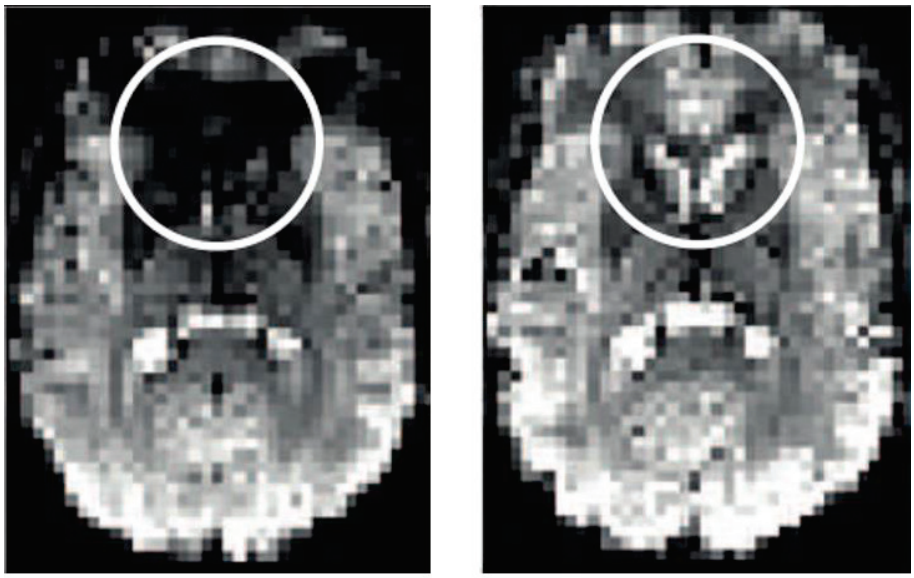

Figure III.5: The effect of varying slice thickness on Intravoxel dephasing artifact. The signal loss (outlined by white circle) with the slice thickness of 4 mm (a) and 1 mm (b).

I.5. DMRI-related artifacts

I.5.1. Eddy currents

The fast switching of strong gradient pulses for diffusion-sensitizing induces eddy currents in the various conducting surfaces of the scanner. This ends by an emergence of various forms of image distortions, including dilation and shift in the phase encoding direction mainly due to the significantly low bandwidth in that direction.

Quantitative parameters as well as parametric maps are computed from diffusion-weighted images obtained with different degrees of diffusion sensitization. Therefore, eddy current-induced distortions will not be the same in all the obtained images, leading to mis-registration between the obtained diffusion-weighted images. This induces a blurring in the computed derived maps and causes inaccurate quantification of diffusion parameters (Fig.III.6.a).

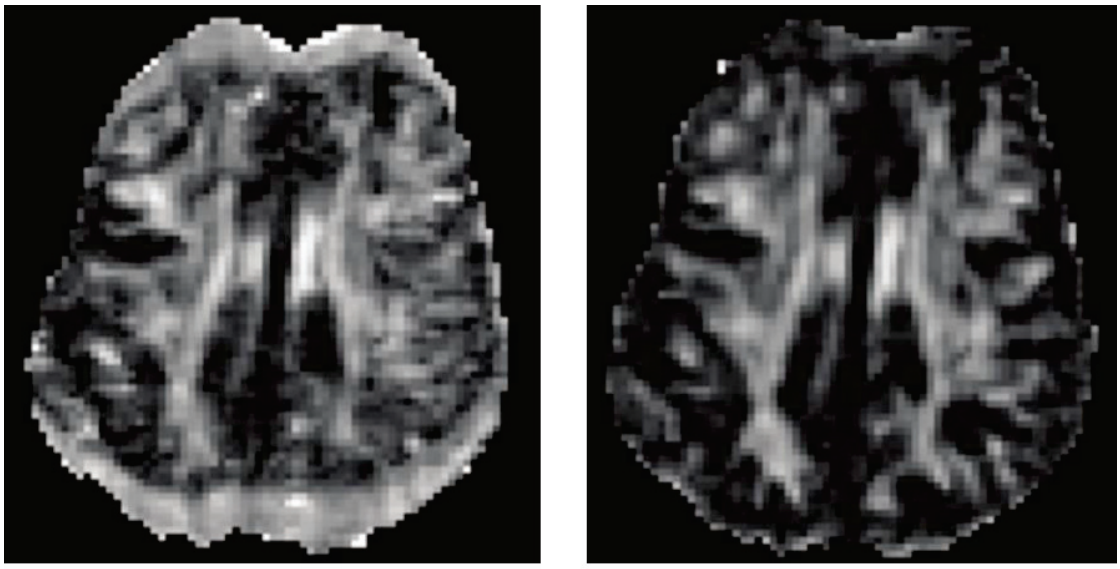

Figure III.6 : Examples of fraction anisotropy map extracted from diffusion-weighted uncorrected data (a), and after eddy currents correction (b) (from (Pierpaoli, 2010)).

Typically, eddy current artifacts can be addressed effectively using an appropriate diffusion sensitizing gradient waveform such as the bipolar gradients (Reese et al., 2003). However, the bipolar diffusion scheme induces an increase of the TE. Furthermore, an alternative approach based on post-acquisition image processing can correct image distortions by comparing the dMRI data to reference artifact-free anatomical data to estimate the distortion map (Fig.III.6.b).

I.5.2. Motion artifact

The major limitation of the diffusion-weighted imaging is its high sensitivity to subject motion, such as involuntary head motion or brain pulsation. In fact, the motion that occurs during the diffusion sensitizing gradients can deteriorate the image quality by inducing phase errors resulting in ghosting artifacts in the reconstructed images.

Currently, the standard 2D-ssEPI is the typical pulse sequence for dMRI due to its acquisition speed and the low sensitivity to subject motion since the entire k-space is sampled in a single shot after the RF pulse. However, the motion-induced phase variations can seriously affect the dMRI data when the k-space is sampled through several segments, i.e. multi-shot-EPI (Fig.III.7). In multi-shot EPI, phase inconsistencies occur when a motion happens between each shot or during the application of a diffusion gradient. This leads to phase inconsistencies between shots, leading to a specific multi-shot ghosting. One must notice that eddy currents have an impact on the ghosting appearance.

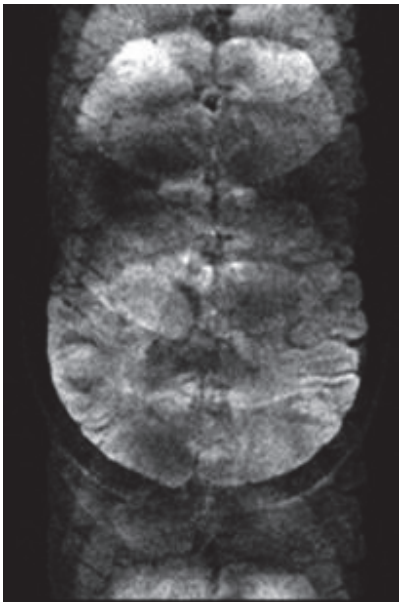

Figure III.7: Motion-induced artifacts in diffusion-weighted data acquired with 8-shot EPI pulse sequence at a b-value of 1000 s/mm2 (From (Liu et al., 2016)).

High-Resolution dMRI Pulse Sequence

I.6. Motivation

In diffusion-weighted imaging, the spatial resolution is restricted by the inherently low SNR and the capability of the used pulse sequence to acquire a large matrix size associated with a tight field of view. Furthermore, the dMRI-related artifacts combined with the EPI artifacts (discussed above) can seriously damage the quality of the reconstructed DW-images. Indeed, the image distortions,

the EPI ghosting and the eddy current effects can induce bias due to the variability of the diffusion measurements, resulting in potentially false-positive findings.

It was shown in previous studies that 3D-EPI acquisition has several advantages over the standard 2D-EPI approach. It allows achievement of thinner adjacent partitions that are beneficial to perform high-resolution dMRI data on the *in-vivo* human brain (Wu et al., 2016b). Also, it provides MR data with significantly higher SNR efficiency compared with the 2D-encoding (Engström and Skare, 2013).

This section provides a description of the development of two acquisition approaches based on 3D encoding of Fourier space to acquire high-resolution dMRI data. The main purpose of this work is to demonstrate the feasibility to perform high spatial resolution and high SNR dMRI data on the *in vivo* macaque brain as well as the human brain at a 3T clinical scanner using the:

- 3D-single-shot-EPI pulse sequence (3D-ssEPI),
- 3D-multi-shot-EPI pulse sequence (3D-msEPI).

The developed approaches were combined with the parallel imaging technique and partial Fourier to further reduce the acquisition duration and to reduce the geometric distortions.

I.7. 3D-EPI dMRI pulse sequence

The diffusion weighting 3D-msEPI and the 3D-ssEPI pulse sequences were developed using Siemens IDEA VD13D and VE11C software. Then, the proposed acquisition approaches were implemented on a 3T MR scanner Magnetom Prisma system (Siemens Healthineers, Erlangen, Germany).

I.7.1. Excitation RF pulses

As discussed above in section (III.1.2), chemical shift is a common issue in EPI sampling induced by the difference in resonant frequency of water protons and fat protons. It leads to a translation of the fat signal according to the water signal.

Instead of the classic fat signal suppression module, a binomial RF pulse known as the water excitation pulse was used. The binomial RF pulse allows addressing the chemical shift artifacts in the proposed pulse sequences by exciting only the water protons (Hauger et al., 2002). As an

alternative to single RF excitation pulse, a series of appropriately timed broadband binomial pulses can induce the same effects of single frequency selective RF pulse.

In this work, the Slab-selective 90° was constructed using the (1-2-1) implementation corresponding to three RF pulses of, respectively, 22.5°, 45°, and 22.5° (Fig.III.8).

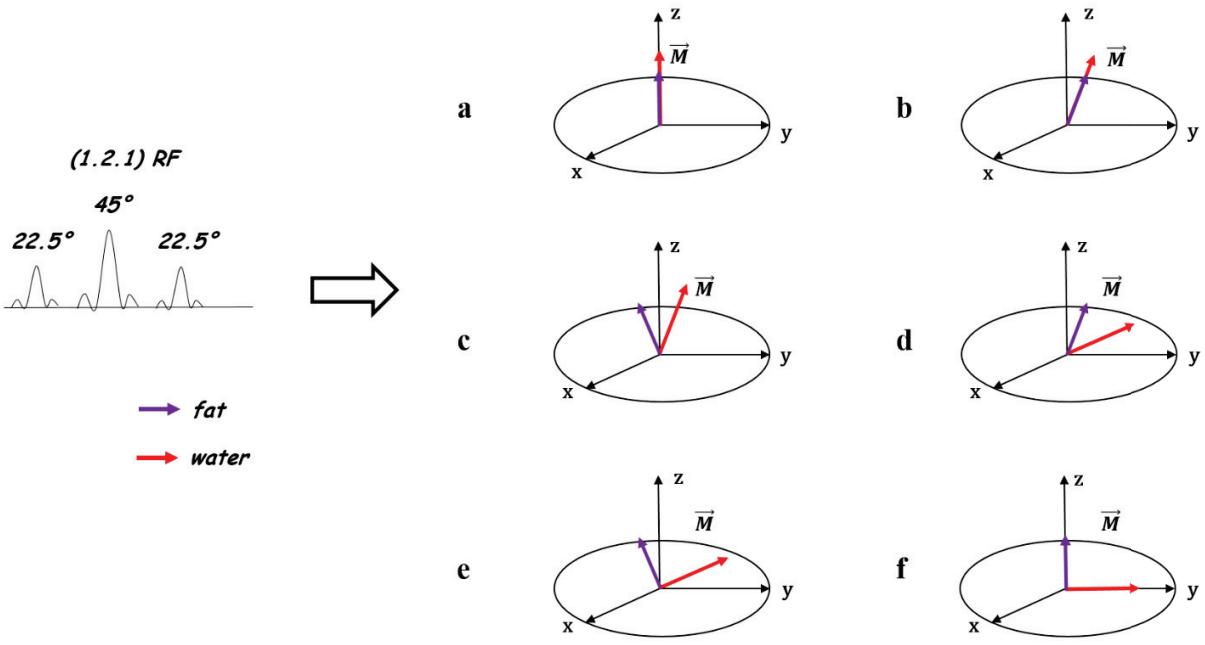

Figure III.8: Examples of a slab-selective 1-2-1 binomial pulse for water excitation used instead of single 90° RF pulse. Under the static B_0 the net magnetization is aligned along z-axis (a). After the first excitation pulse, the magnetization is flipped away by 22.5° (b). Because fat and water protons have different frequencies, after a waiting period the fat and water vectors will be exactly 180° out of phase (c). The second RF pulse tips the magnetization by 45°, resulting of total flipped angle of 67.5° for the water, whereas the fat magnetization is flipped to 22.5° (d). After a second waiting period, a phase difference of 180° will have occurred between the water and fat magnetization vectors (e). An additional RF pulse of 22.5° will completes the 90° excitation for water; however, the fat magnetization is totally restored to the longitudinal status (f).

I.7.2. Nyquist ghosting correction

Nyquist ghosting caused by odd-even echo misalignment along the phase-encoding direction is the most common artifact in EPI (Bruder et al., 1992); see section (III.1.3). A correction method based on reference scan was implemented to avoid ghosting artifacts in the reconstructed images. This approach consists of acquiring three gradient echoes at k_y=0 for each k-space interleave with phase encoding gradient disabled. The references echoes are acquired after the RF excitation pulse and before the first diffusion sensitizing gradient and are used to estimate the phase shift between forwarded and reflected echoes to correct for echo misalignment caused by gradient imperfections (Fig.III.9).

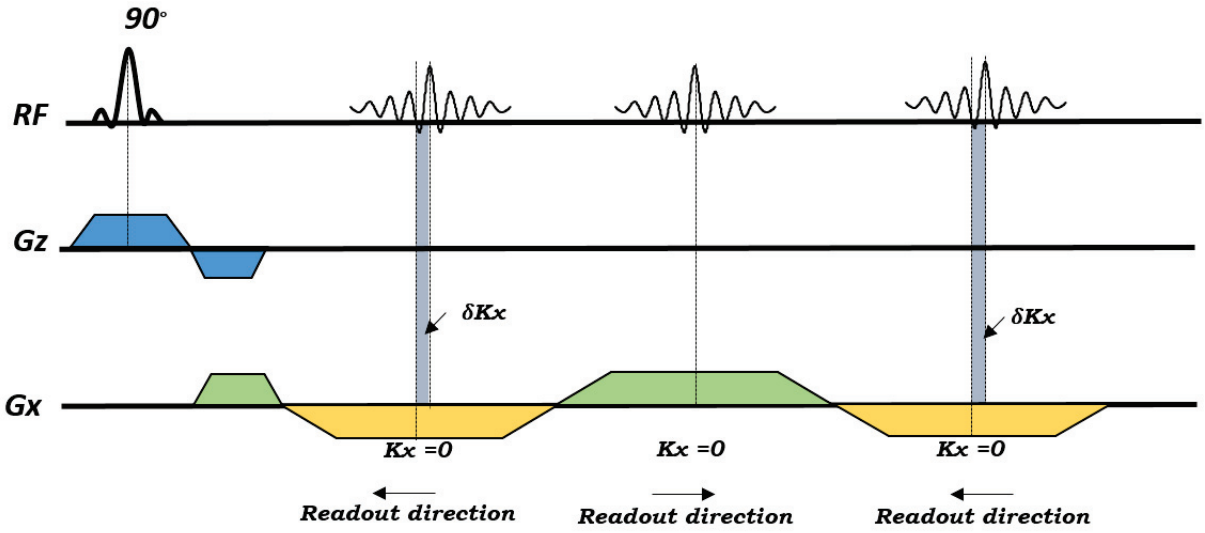

Figure III.9: Acquisition of references lines for phase shift correction by comparing forwarded and reflected echoes.

I.7.3. Diffusion-weighted preparation module

Almost any MR pulse sequence can be modified to be sensitive to diffusion by integrating diffusion sensitizing gradients after the RF pulse and before the readout gradients. In this study, the Stejskal-Tanner preparation scheme (Stejskal and Tanner, 1965) was implemented into the SE-EPI pulse sequence to acquire diffusion-weighted images (Fig.III.1). Two gradient pulses are carried out on

either side of the refocusing RF pulse. For stationary spins, the phase accumulation from the first gradient pulse is reversed by the second diffusion gradient pulse.

I.7.4. Three-dimensional single-shot EPI (3D-ssEPI)

Using the three dimensional single-shot-EPI (3D-ssEPI) approach, the k-space plane is acquired in a single shot after each RF excitation pulse, whereas, the interleaving is performed only on the partitions-encoding direction. Therefore, the achievable TE and the induced distortions shape are comparable to those obtained with the 2D-ssEPI. However, a significant improvement can be reached on SNR and the spatial resolution (Engström and Skare, 2013). In addition, the msEPI approach suffers from its high sensitivity to subject motions which induce an inter-shot variation of MR signal phase which typically causes ghosting artifacts in final images (Chang et al., 2015a; Miller and Pauly, 2003; Ordidge et al., 1994). The ssEPI is widely used because it is more robust to motion effects compared with msEPI. Figure III.10 illustrates the sampling scheme of the k-space using the 3D-ssEPI pulse sequence.

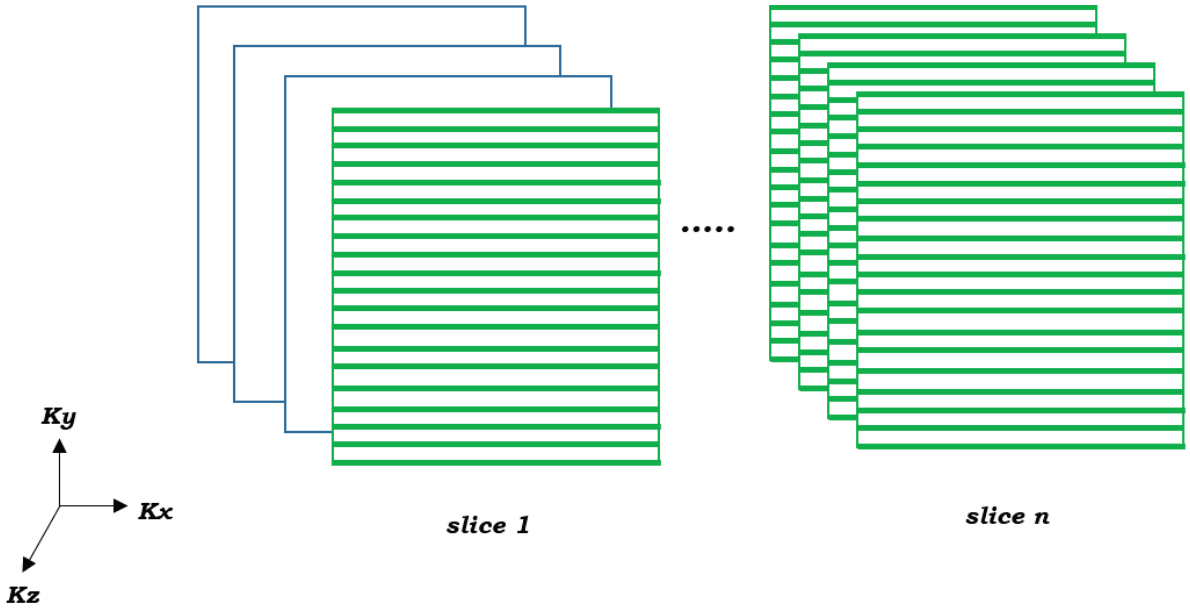

Figure III.10: Schematic of filling of a 3D k-space with looping in the partition encoding direction, whereas the in-plane sampling is performed using the ssEPI scheme.

I.7.5. Three-dimensional multi-shot EPI (3D-msEPI)

Data collected with classic ssEPI are very vulnerable to magnetic field inhomogeneity, resulting in severe images distortions and signal loss. In addition, the long echo train required to fully sample the Fourier space induces image blurring and limited spatial resolution. It was demonstrated that the parallel imaging is the typical method that can be used with the ssEPI pulse sequence to address the off-resonance effect, the geometric distortions, and blurring (Bammer et al., 2001). Indeed, this approach allows shortening of the echo-train by acquiring only half of the Fourier space lines, i.e. for an acceleration factor of 2, leading to an increase in the bandwidth per pixel in the phase encoding direction and to reduction in the total scan duration but with decreased SNR.

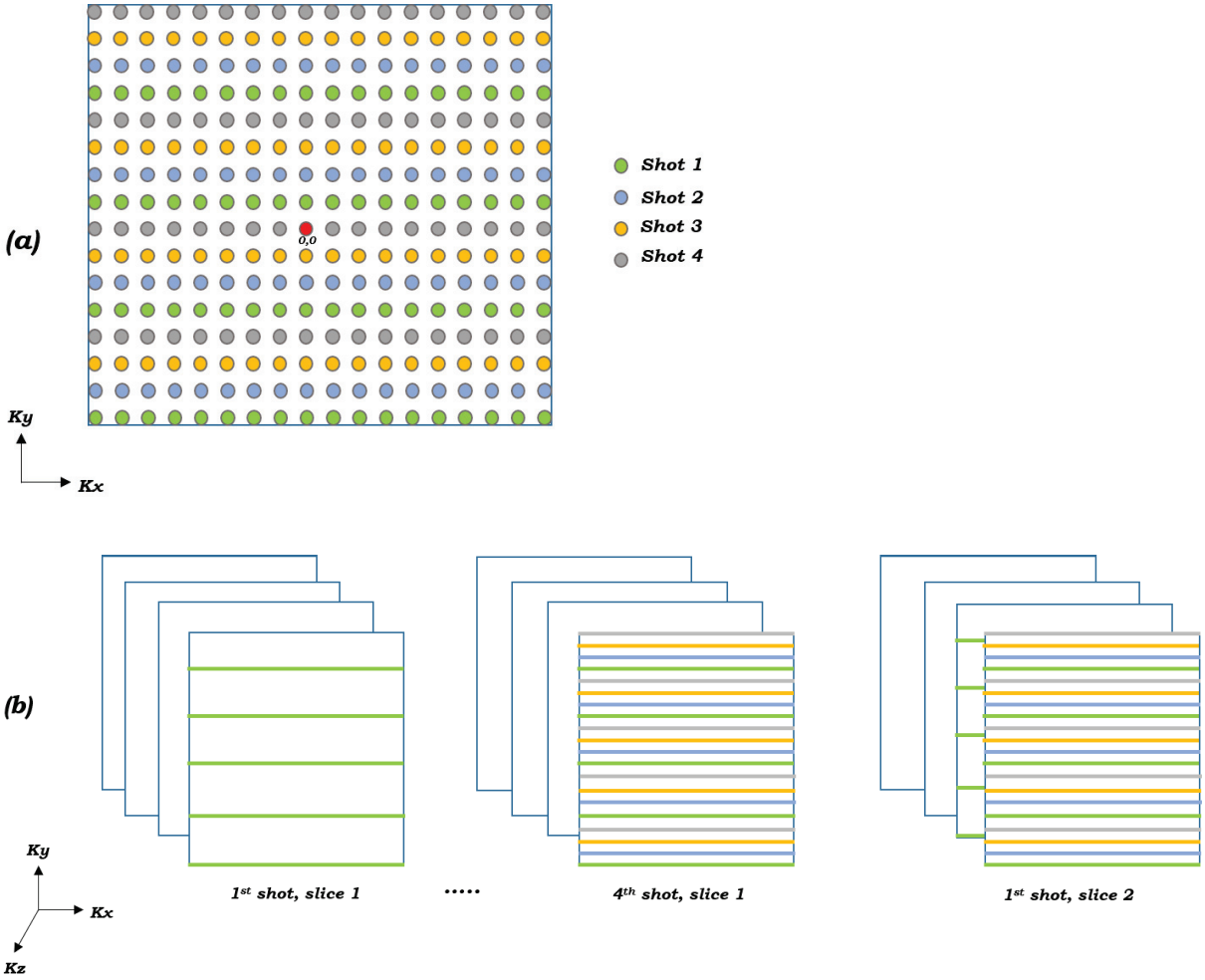

Figure III.11: Example of in-plane k-space sampling using 4-shots msEPI (a), and partition-to-partition acquisition in the 3D k-space (b).

In this study, an in-plane interleaved EPI (msEPI) sampling scheme was used in order to improve the achievable spatial resolution as well as to reduce the various ssEPI-related artifacts. For each EPI shot only a fraction k-space lines are acquired after the RF excitation pulse, resulting in relatively short ETL.

Therefore, the entire k_{xy} space is sampled through numerous EPI segments (Butts et al., 1996). For a given k_z encoding step, all the in-plane (k_x, k_y) segments were acquired sequentially before proceeding to the next k_{z+1} encoding step (Fig.III.11).

For each EPI segment the MR signal is less vulnerable to T_2^* decays effects due to the short ETL and the increased bandwidth in the phase encoding direction. This can produce images with high spatial resolution and reduced image blurring and distortions at the cost of increased scan-time.

I.8. Parallel imaging

The parallel imaging approach refers to the use of phased array coils to improve the MRI acquisitions. Indeed, parallel imaging combined with ssEPI allows to significantly decrease in scan time and reduction of the effects of chemical shift, blurring and off-resonance. This could be beneficial to maintain the robustness of the ssEPI to motion effects. Thereby, a specific reconstruction algorithm is needed for raw data reconstruction.

Basically, parallel imaging was introduced to speed up the MRI acquisition by acquiring only a fraction of the k-space lines. For raw data reconstruction, parallel imaging uses the coils sensitivities information mainly through two ways: First, the image domain reconstruction such as the SENSE technique, where the computed sensitivities maps are used to unravel the aliased images obtained by each coil element; second, the frequency domain such as GRAPPA, where the sensitivity information allows estimation of the weighting factor to generate the missing k-space lines. Using parallel imaging, scan time is decreased by a factor R, called the acceleration factor. The total scan time of a 2D EPI pulse sequence is given by the following equation:

$$T_{scan} = \frac{N_{ext} \times TR \times N_{PE}}{R \times ETL} \tag{3.5}$$

where N_{ext} is the number of signal averaging, N_{PE} is the full k-space lines and R is the acceleration factor.

I.8.1. Coil sensitivity

In MRI, the transmit coil emits the RF pulse in order to excite the spins located in the selected slice/slab. The receiver coil detects the tiny signal emitted by the spins during the relaxation phase once the transmitter is switched off.

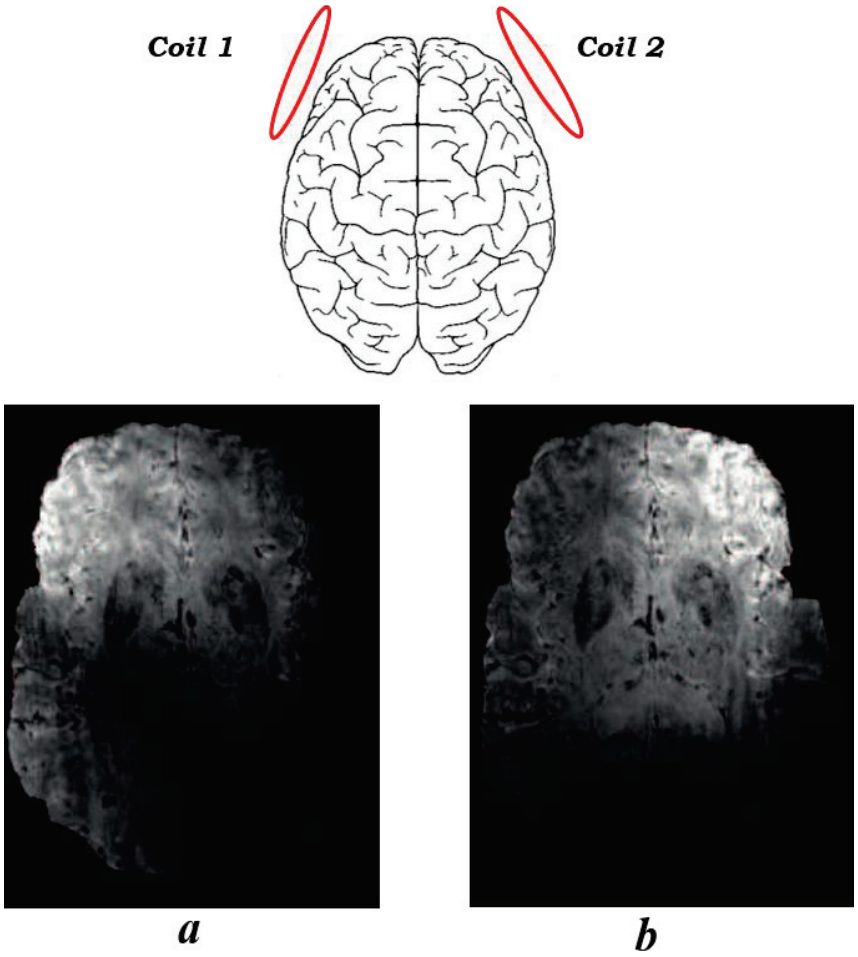

Figure III.12: Magnitude images (a) and (b) acquired with the coil 1 and coil 2, respectively, resulting in different sensitivities information (From (Mayur NARSUDE, 2014)).

In routine examinations, the MR signal can be collected using a single element or multi-channels receiver coils. The phased arrays coils are increasingly used in MRI acquisition for better coverage of the imaged subject (e.g., the human brain) and for maintaining homogenous signals, leading to higher SNR. For example, the final image $I(r)$ acquired using an n-phased arrays receiver coil can be described as follows:

$$R_n(r) = I(r)S_n(r) + N_n(r) \tag{3.4}$$

where (r) indicates the positions in the image space I (r), $S_n(r)$ is the complex sensitivity of the coil element (n), and $N_n(r)$ is the complex Gaussian noise. In the acquired image, the intensity of the received signal at a point (p) varies as a function of the distance from the coil. Figure IV.12 shows an example of reconstructed images acquired with two independent receiver coils. The spatial sensitivity of each individual coil element can provide additional information about the spatial position of the received signal. The acquired data by each coil element is reconstructed separately and then combined with the other elements to generate the final image.

I.8.2. SENSE

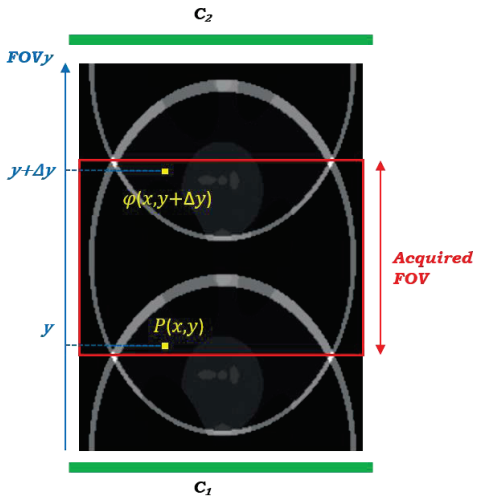

Figure III.13: Reconstruction in SENSE: Example with an acceleration factor (R=2) and two coil elements C_1 and C_2. The signal component at the aliased point P(x, y) in the obtained image is made up of the correct signal S (x, y) for this position (y) and one aliased signal S (x, y+ Δy) from aliased position φ(x, y + Δy).

Actually, the bandwidth in the readout encoding direction is significantly higher than in the phase encoding steps. Therefore, to accelerate data acquisition, the scan duration in the phase encoding direction can be reduced by skipping k-space lines using increased phase encoding step Δk_y, resulting in reduced ETL and reduced FOV.

SENSE (sensitivity encoding) acceleration method allows acquiring of data in a reduced FOV. Therefore, the Fourier-transformed data produce fold images in the phase encoding direction, yielding aliasing artifacts in that direction. The aliased signal component at each point is determined using the spatial sensitivities information from coil elements.

For example, with an acceleration factor (R) and two coil elements C_1 and C_2, the signal component at the aliased point P (x, y) in the obtained image I (x, y) is made up of the correct signal S (x, y) for this position (x,y) and one aliased signal S $(x, y+ \Delta y)$ from aliased position $\varphi(x, y + \Delta y)$ (Fig.III.13). the obtained images from each coil can be expressed as follows:

$$I_1(x, y) = \zeta_1 (x, y) \times S (x, y) + \zeta_1 (x, y+\Delta y) \times S (x, y+\Delta y) \qquad (3.6)$$

$$I_2(x, y) = \zeta_2 (x, y) \times S (x, y) + \zeta_2 (x, y+\Delta y) \times S (x, y+\Delta y) \qquad (3.7)$$

where $I_1(x, y)$ and $I_2(x, y)$ are the images obtained from C_1 and C_2, respectively. The coils are characterized by sensitivities ζ_1 and ζ_2, whereas Δy is the distance aliasing which can be written as follows:

$$\Delta y = \frac{FOV_y}{R} \qquad (3.8)$$

The FOV_y is the field of view in the phase encoding direction and R is the SENSE factor. Having provided knowledge on coils sensitivities information, the aliased signal components S $(x, y+ \Delta y)$ can be calculated and reassigned to its proper location.

Low-resolution calibration scans are carried out prior to the main imaging data acquisition to generate the sensitivity maps for each coil element. Then, the imaging data acquired by each coil element are Fourier-transformed to generate the aliased image. Last, the computed sensitivity maps as well as the obtained images are fed into the SENSE reconstruction algorithm to reconstruct the final image.

I.8.3. GRAPPA

GRAPPA (GeneRalized Autocalibrating Partially Parallel Acquisitions) (Griswold et al., 2002) is a further extension of the Auto-SMASH principle (Jakob et al., 1998).With GRAPPA, the data processing is made in the frequency domain, unlike in SENSE. The k-space is partially filled by skipping lines in the phase encoding direction. Figure III.14.b illustrates an example of an under-sampled k-space with an acceleration factor R=2, where one k-space line is skipped.

Additional low-resolution data are collected prior to the imaging data, where only the central part of k-space is sampled, so-called the auto-calibration signal (ACS). The ACS are used to estimate the weighting factors. Then, for each coil element, the missing k-space lines are estimated using the obtained weighting factors by convolution with the GRAPPA kernel estimated from the ACS of acquired data (Figure III.14.a) and (III.14.c).

Assuming that reconstruction of the missing k-space data in coil C at a line $(kx, ky + \varepsilon\Delta ky)$ using a block wise reconstruction can be represented by (Griswold et al., 2002):

$$S_C(kx, ky + \varepsilon\Delta ky) = \sum_{i=1}^{I} \sum_{b=0}^{N_b-1} n(j, b, i, \varepsilon)\ S_l(kx, k_y + bm\Delta k_y) \qquad (3.9)$$

where the index i counts through the individual coils and b counts through the individual reconstruction block. N_b is the number of blocks used in the reconstruction. A block is defined as a single acquired line and its adjacent m-1 missing lines, where m represents the acceleration factor. $n(j, b, i, \varepsilon)$ represents the coefficients for the linear combination.

This process is repeated for each individual coil element in the array, resulting in I sets of k-space. Then, separate images are generated after Fourier transformation of the completed k-spaces from different channels. Finally, the image is obtained using sum-of-squares method to combine all coils images. In order to speed up the 3D acquisition, the parallel acquisition method was developed and implemented in the proposed pulse sequences. The acceleration can take place in the partitions encoding direction for the 3D-msEPI pulse sequence, or in both phase and partitions encoding directions for the 3D-ssEPI pulse sequence. Figure III.15 illustrate an example of accelerated 3D-msEPI and 3D-ssEPI with R= 2 and R=4.

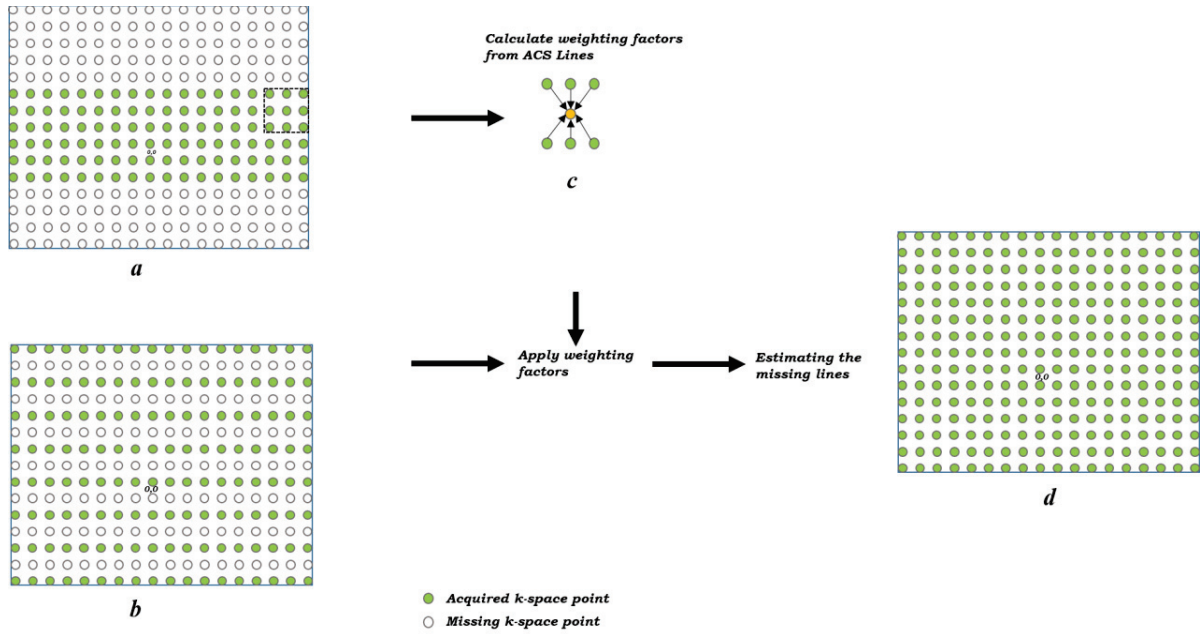

Figure III.14: A: the auto-calibration signals (ACS) collected at the central part of k-space, b: Under-sampled k-space data collected, c: The kernel (outlined by the dotted black box) consisting of source points (green circles) and target points (yellow circle) to calculate the weights factors. It is repeated through the ACS lines. d: The obtained weights are then applied to fill in the missing k-space points by interpolation.

Some improvements were done in parallel imaging by:

- Changing the acquisition mode (Caipirinha), which leads to a better reconstruction quality.
- An estimation of the reconstruction GRAPPA kernel by iterative method like Spirit or E-spirit.

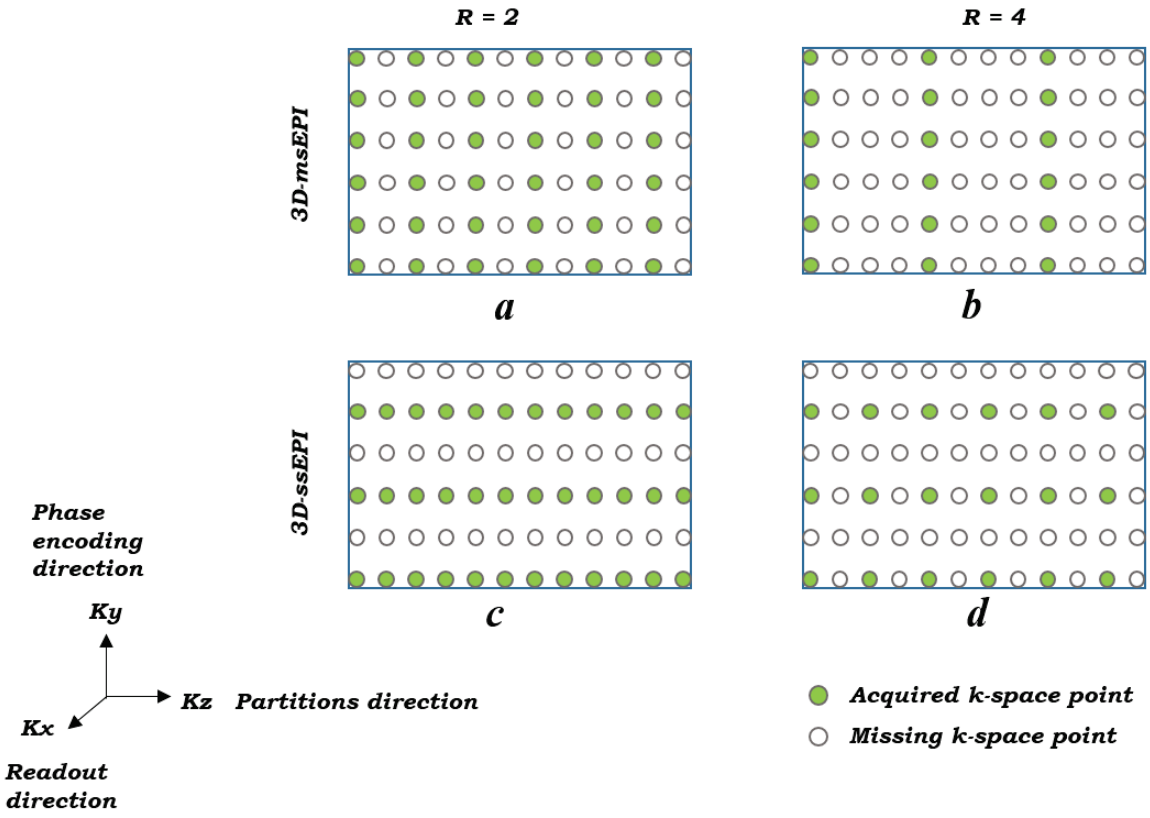

Figure III.15: The under-sampled k-space data collected using the 3D-msEPI (a, b) and the 3D-ssEPI (c, d) with an acceleration factor of R=2 (a, c) and R=4 (b, d): the acceleration is allowed only in the partitions direction with the 3D-msEPI pulse sequence.

In-vivo dMRI of Anesthetized Macaque Brain

I.9. 3D-msEPI dMRI data

I.9.1. DMRI protocol setup

Pilot studies were led *in-vitro* and *in-vivo* in order to optimize acquisition parameters and to validate the implemented 3D-msEPI-based dMRI acquisition approach as well as to demonstrate the feasibility of performing high isotropic spatial resolution of dMRI data on the *in-vivo* macaque brain at 3T.

A dedicated phantom was constructed in the lab based on a Lavdas et al. study (Lavdas et al., 2013). The spherical diffusion phantom was specifically constructed to:

* Have tissue-equivalent diffusivity parameters to mimic the conditions typically found in biological tissues.

* Allow the achievement of an isotropic spatial resolution of 0.6 mm.

An 8-channel phased-array coil designed to fit the size and the shape of the primate head was used for NMR signal reception, whereas the radiofrequency transmission was performed using a surface coil (Kolster et al., 2014). Two healthy adult Rhesus macaques (8 and 7 years old) were involved. Before MR scanning, the monkeys were anesthetized with Zoletil 100 (15 mg/kg) and set in a sphinx position on a plastic monkey chair with head restraining.

.

I.9.2. DMRI data acquisition

In the first time, the 3D-msEPI dMRI pulse sequence was optimized and used to collect cerebral dMRI data of anesthetized macaque monkeys with an isotropic spatial resolution of 0.6 mm using the following scan parameters: Repetition-Time/Echo-Time: 750/61 ms; Matrix size: 208×186×96 pixels; bandwidth=776Hz/pixel; EPI-factor=52, number of k_{xy} EPI shots=4; Field of view: 125×112×57.6 mm^3; Partial Fourier factor along k_y direction=6/8; and along k_z direction=6/8. Diffusion encoding directions: 21 directions acquired with b-value=1000 s/mm^2. Two images were collected with a b-value=0 s/mm^2. The total acquisition duration of DTI data was 1 hour and 19 minutes.

I.10. Preliminary results

The preliminary results indicate that the developed 3D-ssEPI pulse sequence is an effective approach to improve the overall SNR, the achievable spatial resolution and to minimize susceptibility-induced distortion of dMRI acquisition on the *in-vivo* monkey brain. Thanks to this approach, an isotropic resolution of 0.6 mm was achieved for the first time on an anesthetized macaque. Figure III.16 shows an example of a fractional anisotropy map achieved in this study. In addition, these preliminary results have shown that the use of the 8-channel phased-array coil,

designed with a surface coil for the radiofrequency transmission, induces B1 inhomogeneities which affect the quality of DW-images localized far from the center of the transmission coil.

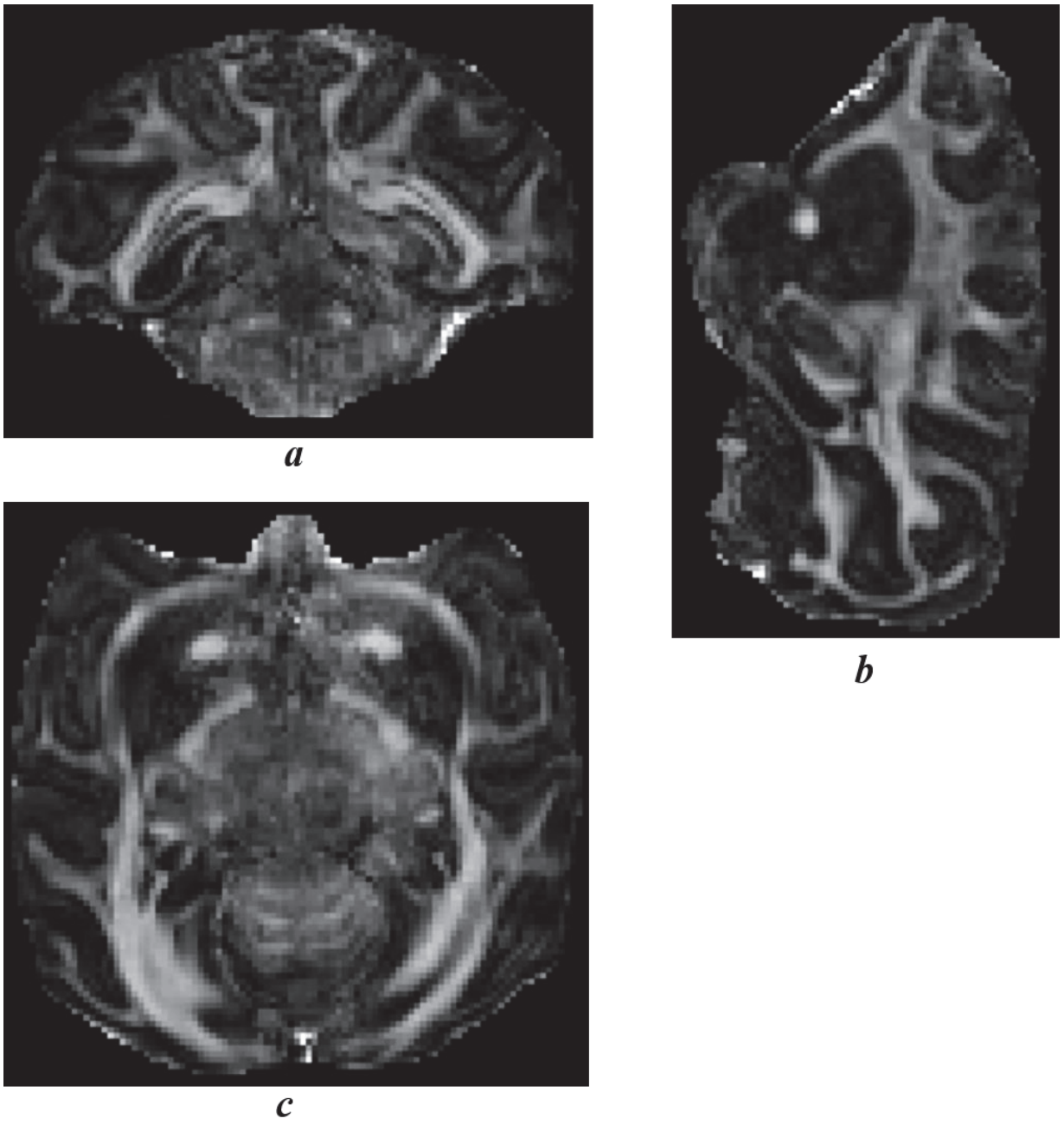

Figure III.16: Fractional anisotropy map (coronal view (a), sagittal view (b) and axial view (c)) acquired on anesthetized macaques at 3T with an isotropic spatial resolution of 0.6 mm

I.11. Experimental setup and dMRI protocol optimization

Instead of the 8-channel phased-array receive coil with local transmission, the whole body coil was used for RF transmission combined with three loop coils, whose diameters were 7 cm, 11 cm and 11 cm, respectively, for MR signal reception. Unlike the local transmission coil, the whole body coil should provide a higher homogeneous B1 field all over the monkey brain.

Furthermore, the monkeys are placed in a sphinx position in a Kopf MRI-compatible stereotaxic frame (Kopf Instruments, Tujunga, CA) and were intubated and maintained under 1.5% of isoflurane. This is beneficial for the dMRI acquisition since the animal head was fixed to avoid any rigid body motion. Also, the isoflurane anesthesia allows extension the animal for a long scan time (<4h) compared with the intramuscular injection.

Additional adjustments were performed on *in-vivo* in order to further optimize the acquisition parameter values such as the bandwidth, the partial Fourier factor, the number of EPI segments. This allows us to achieve a higher isotropic resolution (0.5 mm).

I.12. Comparison with the 2D-ssEPI and -msEPI pulse sequences

To demonstrate the effectiveness of the 3D-msEPI approach, the benefit of temporal SNR (SNR per unit of time) improvement with the 3D-msEPI sequence was evaluated through a direct comparison with the multi-slice 2D-ssEPI as well as the 2D-msEPI dMRI pulse sequences. The common protocol parameters for all of the three sequences were: FOV_{xyz} = 125×105×67.2 mm^3, matrix $size_{xyz}$ = 248×210×112 voxels, Partial Fourier factor along k_y direction = 6/8, phase encoding direction = AP. The slice thickness was set to 0.6 mm in all acquisitions to follow the hardware limits of the 2D-EPI pulse sequences. Total scan time per sequence was kept constant at 4 min across all the scans. DW-images were acquired with b-value = 1000 s/mm^2 using each of the three pulse sequences. Additional parameters set up for the three pulse sequences are recapitulated in Table III.1.

Parameters	*3D msEPI*	*2D msEPI*	*2D ssEPI*
TR (ms)	**750**	**15200**	**41200**
TE (ms)	**72**	**72**	**186**
FOV (mm)	**125*105**	**125*105**	**125*105**
Matrix size (pixel)	**248*210**	**248*210**	**248*210**
Spatial resolution (mm^3)	**0.5*0.5*0.6**	**0.5*0.5*0.6**	**0.5*0.5*0.6**
Bandwidth (Hz/pixel)	**776**	**776**	**776**
Partial Fourier Factor (ky)	**6/8**	**6/8**	**6/8**
Partial Fourier Factor (kz)	**6/8**	**-**	**-**
Scan time	**4m10s**	**4m18s**	**4m04s**

Table III.1: Scan parameters used in the comparison between 3D-msEPI, 2D-msEPI and 2D-ssEPI dMRI pulse sequences

A visual inspection in term of image quality and distortion level can be sufficient to evaluate the effectiveness of the proposed 3D-msEPI compared to the gold standard 2D-ssEPI pulse sequence (Fig.III.18.a and III.18.c). However, for an accurate quantification, SNR comparison was made between the 3D- and 2D-msEPI dMRI pulse sequences since they share the same image artifact (geometric distortion, deformation) (Fig.III.18.a,b). Therefore, to evaluate the SNR improvement with the 3D-msEPI, SNR maps were computed for both datasets on b1000-images, by dividing the intensity of each pixel of the image by the standard deviation of noise measured within two regions of interest (ROIs) delineated in the background of the image. Then, the colored map was computed pixel-by-pixel as the ratio of the 3D-msEPI SNR map to the 2D-msEPI SNR map (Fig.III.18.d).

The computed $SNR_{3D\text{-}msEPI}/SNR_{2D\text{-}msEPI}$ maps, computed from images acquired with b=1000 s/mm^2, reveal an average ratio of $SNR_{3D\text{-}msEPI}/SNR_{2D\text{-}msEPI}$ of about 4.7 for the white matter and of about 3 for the grey matter. The white matter ROIs were placed in the Corpus Callosum and the posterior limb of the internal capsule.

Average ratios of $SNR_{3D\text{-}msEPI}/SNR_{2D\text{-}msEPI}$ about 4 for the white matter and about 3 for the grey matter were obtained from images acquired without diffusion weighting (b=0 s/mm^2).

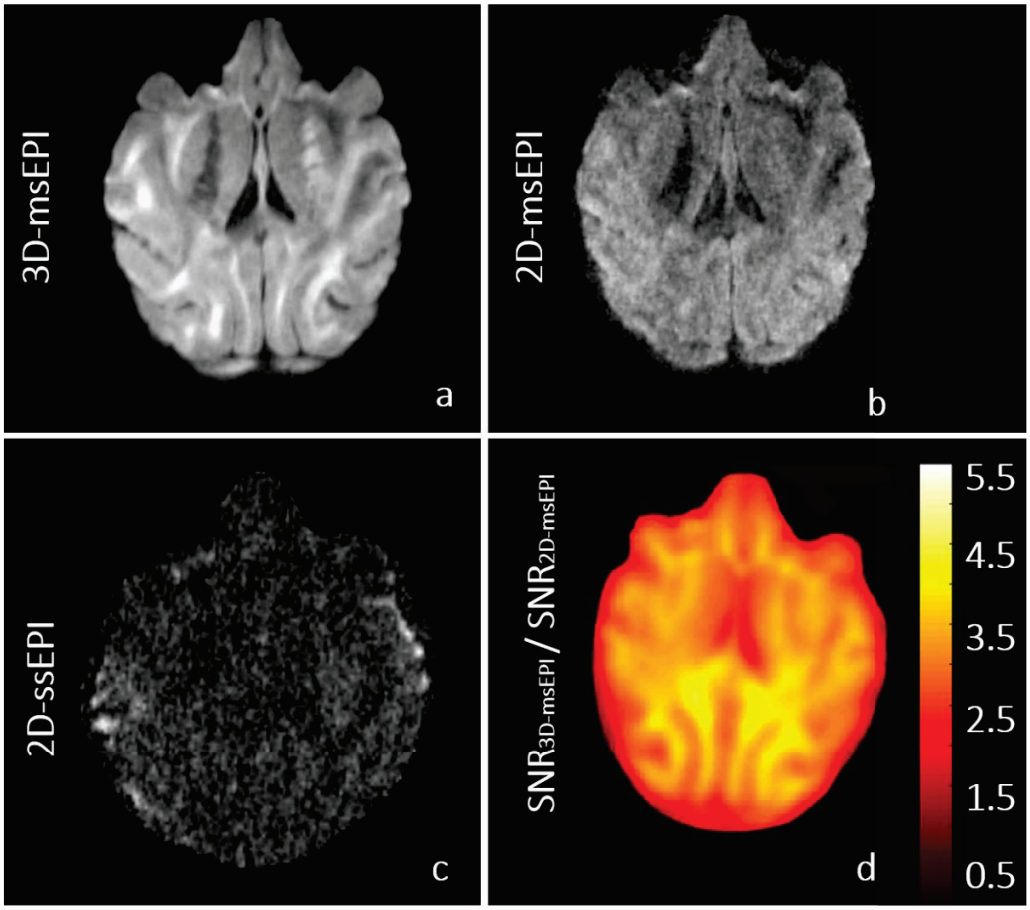

Figure III.17: B1000-images acquired using 3D-msEPI (a), 2D-msEPI (b) and 2D- ssEPI (c) pulse sequences. The SNR3D-msEPI/ SNR2D-msEPI map computed with b1000-images to evaluate the SNR improvements between the 3D-msEPI and the 2D-msEPI approaches (d).

I.13. Cerebral dMRI of macaque brain with a spatial resolution of 0.5 mm

Cerebral dMRI data were acquired with an isotropic spatial resolution of 0.5 mm using the proposed 3D-msEPI-based dMRI pulse sequence, and using the whole body coil for RF transmission and three loop coils for MR signal reception.

The acquisition parameters were set to: Repetition-Time (TR)=750 ms, Echo-Time (TE)=72 ms, bandwidth=776Hz/pixel, EPI-factor=53, number of k_{xy} EPI shots=4, Field Of View

$(FOV)_{xyz}$=125×105×56 mm^3, Matrix $Size_{xyz}$=248×210×112 voxels, Partial Fourier factor along k_y direction=6/8, and along k_z direction=6/8 and phase encoding direction=Anterior-Posterior (AP). With these parameters, the acquisition duration of a whole brain 3D DW-image was 4 min 10 sec. Figure III.17 shows an example of axial views of the macaque brain images achieved at 3T with an isotropic spatial resolution of 0.5 mm. In this condition, diffusion tensor data with 30 diffusion directions and with 2 non DW-images could be acquired in 2 h 13 min.

The acquisition duration required to collect this high resolution data with sufficiently SNR is relatively large and could be not compatible with the experimental conditions of certain studies. A shorter acquisition duration could be reached using 3D-msEPI dMRI pulse sequence with parallel imaging technique and using a receiving coil more sensitive than that we used in this work.

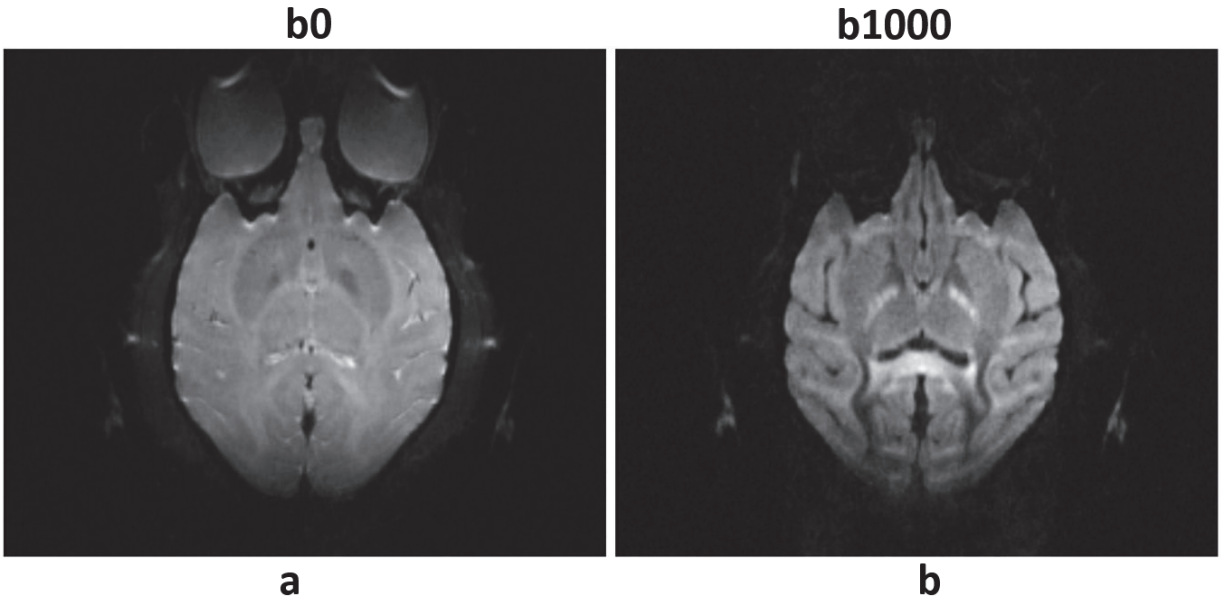

Figure III.18: Example of axial views of the obtained b0 (a) and b1000 (b) images acquired with an isotropic spatial resolution of 0.5 mm on one macaque monkey brain.

A dMRI study involving four macaques has been performed in order to demonstrate the achievability at 3T of very high resolution (isotropic spatial resolution of 0.5 mm) dMRI of the anesthetized macaque brain using the 3D-msEPI dMRI pulse sequence. This study, presented in chapter 4, illustrates also the benefits of very high-resolution dMRI data to analyze thin brain structures.

I.14. 3D-ssEPI dMRI data of macaque brain

The large acquisition duration of 3D-msEPI dMRI pulse could limit its use particularly for dMRI studies requiring a high number of diffusion directions or multi-shell encoding of water molecule diffusivity. We therefore developed the 3D-ssEPI dMRI pulse sequence to obtain a desirable compromise between the required acquisition duration and the achieved spatial resolution.

Additional datasets were acquired using 3D-ssEPI on one monkey brain using the optimal experimental setup previously presented. Similarly, DW-images were acquired with b-value = 0 s/mm^2 and b-value = 1000 s/mm^2 at an isotropic spatial resolution of 0.8 mm using the following parameters: Repetition-Time (TR)=1200 ms, Echo-Time (TE)=79 ms FOV_{xyz} = 125×105×57.6 mm^3, matrix $size_{xyz}$ = 156×130×72 voxels, Partial Fourier factor along k_y direction = 5/8 and along k_z direction=6/8 phase encoding direction = AP. With these parameters, the acquisition duration of a whole brain 3D DW-image was 64 sec. Figure III.19 shows an example of axial views of the macaque brain images achieved at 3T using 3D-ssEPI dMRI pulse sequence with an isotropic spatial resolution of 0.8 mm.

The proposed ssEPI acquisition approach allows speeding up of the scan duration compared to the msEPI, as well as achievement of a spatial resolution of 0.8 mm on the *in-vivo* macaque brain in an acceptable scan duration of 1 minute per image. An isotropic spatial resolution of 0.8 mm remains higher than that reported in the literature to non-invasively perform dMRI data on the macaque brain.

I.15. Comparison with the state of the art

The low sensitivity of the acquisition as well as the spatial resolution are a crucial challenge for dMRI application. The high spatial resolution is key for an accurate analysis of the cerebral microstructure and delineation of the white matter connectivity. The obtained dMRI data demonstrates that the 3D-msEPI is a suitable approach that allows acquiring *in vivo* dMRI data of the macaque brain with sub-millimetric spatial resolution. An isotropic resolution of 0.5 mm dMRI data were successfully collected. Such a resolution is the highest ever achieved on an *in-vivo* macaque brain. The voxel size reached in this study, 0.125 mm^3, is 2.7 times smaller than that achieved by Janssens et al. (0.343mm^3). In addition, the dMRI data were acquired non-invasively

using the 3-channel surface coils, whereas Janssens et al. have used an 8-channel phased array coil whose loops were invasively implanted onto the skull of a macaque monkey.

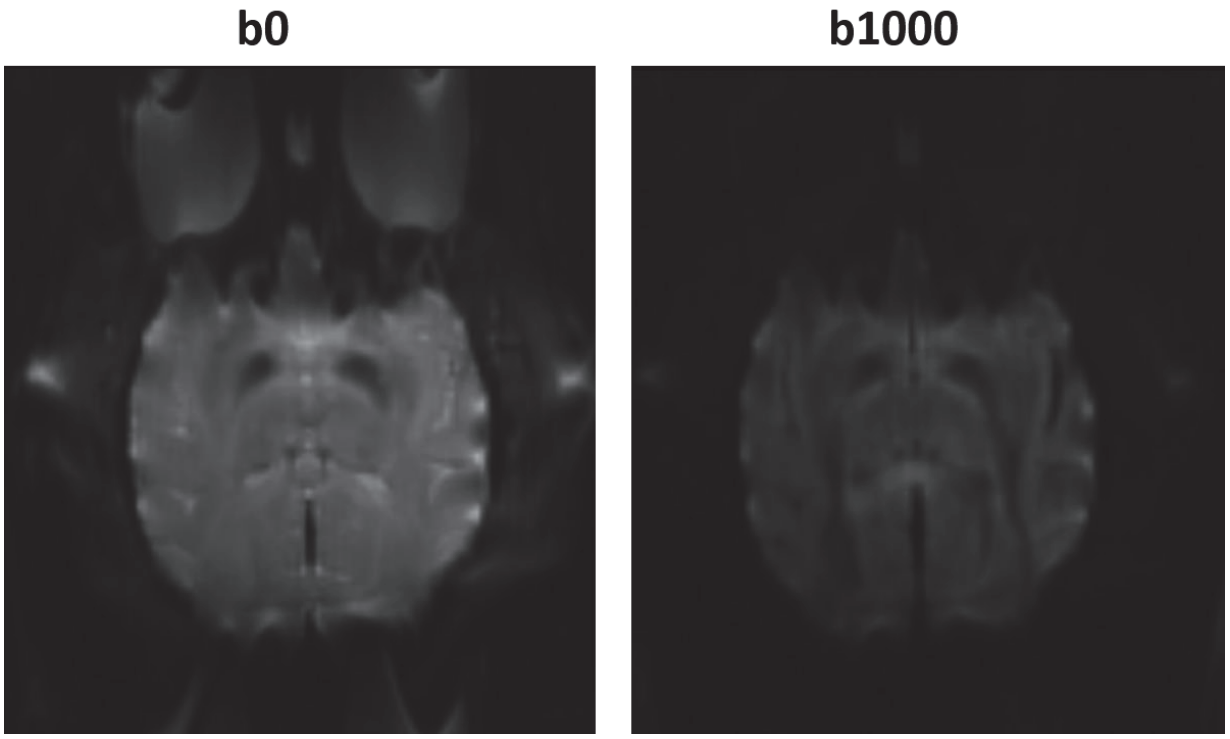

Figure III.19: Example of axial views of the obtained b0 and b1000 images acquired with an isotropic spatial resolution of 0.8 mm on one macaque monkey brain in 2 minutes.

DMRI on the Human brain

I.16. Data acquisition

Some preliminary data have been acquired in humans using the developed 3D-msEPI and 3D-ssEPI dMRI pulse sequences. DW-images were acquired from two healthy adult subjects on the 3T Prisma system (Siemens Healthineers, Erlangen, Germany) using a 64-channel head coil for signal reception and the whole body coil for RF transmission.

I.16.1. 3D-msEPI data

The first subject was involved to perform high-resolution dMRI data using the 3D-msEPI dMRI pulse sequence. DW-images with b-value=1000 s/mm^2 were collected along 12 diffusion-encoding

directions as well as one non DW-image. An isotropic resolution of 0.8mm x 0.8mm x 0.8mm was achieved using the following parameters: TR/TE=1000/64 ms, number of k_{xy} EPI shots=4, FOV_{xyz} = 210×179×89.6 mm^3, matrix $size_{xyz}$ = 262×224×112 voxels, Partial Fourier factor along k_y direction = 6/8 and along k_z direction=6/8 phase encoding direction = AP. The acquisition time was 5 minutes 35 seconds per whole brain DW-image. Figure III.20 shows an example of the high-quality axial, coronal and sagittal views of the 3D DW-images of the human brain acquired with the 3D-msEPI dMRI pulse sequence with an isotropic spatial resolution of 0.8 mm.

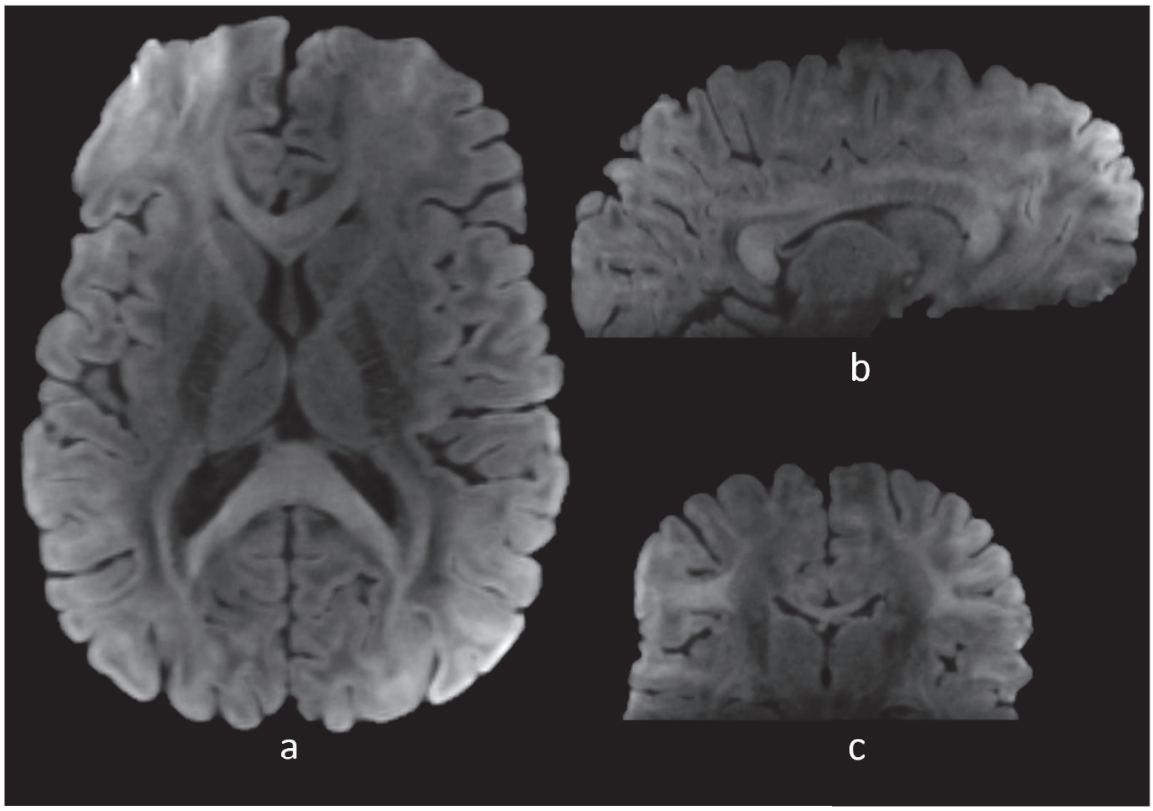

Figure III.20: Example of axial (a), sagittal (b) and coronal (c) views of the obtained b1000-images acquired with the 3D-msEPI with an isotropic resolution of 0.8 mm on the human brain in 5 minutes 30 seconds.

I.16.2. 3D-ssEPI data

Parallel imaging was implemented in the proposed 3D-ssEPI dMRI pulse sequence. Additional dMRI datasets were acquired using this pulse sequence with b-value=1000 s/mm^2 and with b-value of b=0 s/mm^2. An isotropic spatial resolution of 1.2 mm was acquired using the following parameters: TR/TE= 1000/86 ms, in-plane acceleration factor R=2, FOV_{xyz} = 211×180×115 mm^3, matrix $size_{xyz}$ = 176×150×96 voxels, Partial Fourier factor along k_y direction = 7/8 and along k_z direction=6/8 phase encoding direction = AP. The acquisition time was 1 minute 12 seconds per volume. Twenty-one DW-images were collected in twenty-one diffusion non-collinear directions. Figure III.21 shows an example of the obtained images

Unlike the 3D-msEPI, the 3D-ssEPI sampling of the Fourier space allows achievement of an isotropic resolution of 1.2 mm with high SNR in a reduced scan time, i.e., 1 minute per volume compared to 5 minutes for the msEPI).

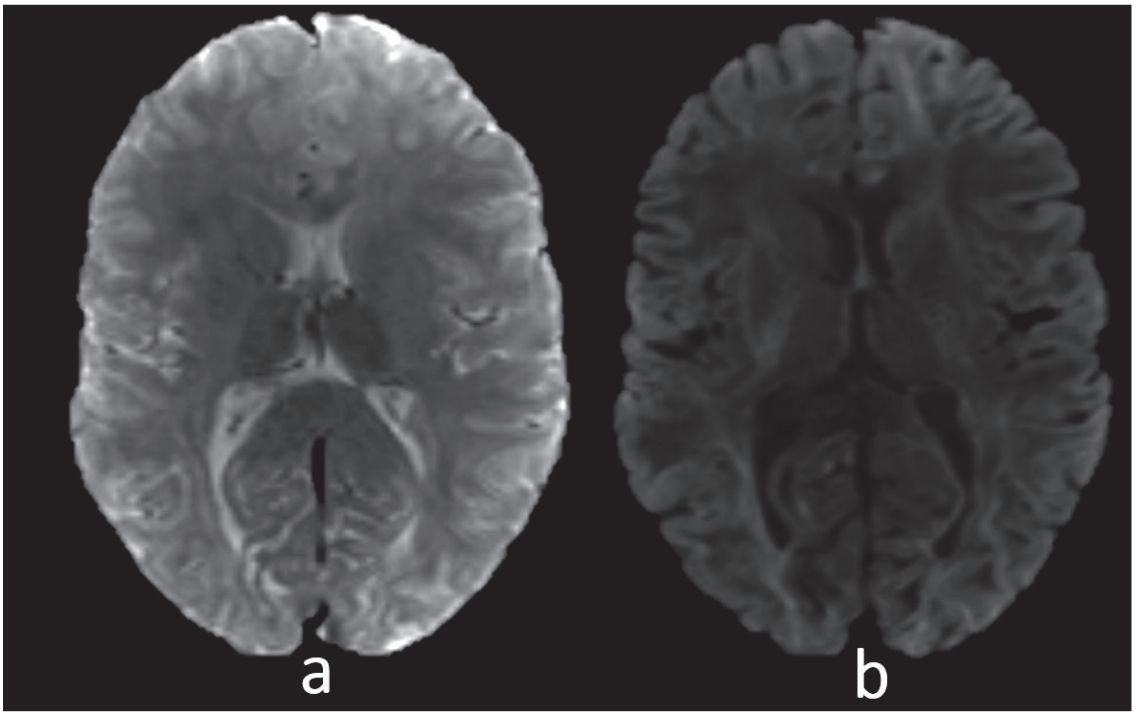

Figure III.21: Example of axial views of the obtained b0 and b1000 images acquired with an isotropic spatial resolution of 1.2 mm on one subject in 1 min 12s.

The acceleration factor R=2 along the first phase encoding direction allows shortening the scan time by acquiring only the half of the k-space lines, resulting in significantly reduced geometric distortions in the reconstructed images. The obtained images are consistent with that reported in the Engström study (Engström and Skare, 2013). However, more efforts should be invested to further improve the achieved spatial resolution as well as the obtained SNR in the acquired images. Additional optimization of acquisition parameters, (e.g., TR, acceleration factor, etc.), will likely allow achievement of a submillimeter spatial resolution within an acceptable scan time.

Conclusion

The ssEPI was a very successful method for diffusion-weighted imaging because it is capable of speedy acquisition and is less sensitive to motion artifacts. However, the ssEPI is prone to off-resonance effects, blurring and limited spatial resolution. The use of parallel imaging is the typical way used to improve the spatial resolution and correct image distortions, although with an SNR penalty.

In this work, acquisition approaches were developed to perform high-resolution diffusion-weighted imaging on *in-vivo* human and non-human primate brains. A significant improvement in the image quality, i.e. overall SNR, distortions, blurring, as well as the available spatial resolution have been demonstrated using the developed pulse sequences.

Chapter IV. Application on in-vivo macaque brain at 3T

Introduction

This section is based on:

High-resolution 3D diffusion tensor MRI of anesthetized rhesus macaque brain at 3T. NeuroImage, 2018, 181:149-161

Slimane Tounekti, Thomas Troalen, Yann Bihan-Poudec, Mathilda Froesel, Franck Lamberton, Valéry Ozenne, Justine Clery, Nathalie Richard, Maxime Descoteaux, Suliann Ben Hamed, Bassem Hiba

In the previous Chapter, it has been demonstrated the feasibility of achieving an isotropic spatial resolution of 0.5 mm of cerebral dMRI data on *in-vivo* macaque monkey using the developed pulse sequence at 3T clinical scanner.

Here, a dMRI study was carried out on 4 anesthetized Rhesus macaque monkeys. The main purpose of this study is to validate the proposed method by:

- Acquiring dMRI data with an isotropic spatial resolution of 0.5 mm on many subjects (male/female, different age).
- Highlighting the potential of dMRI data performed with such high resolution to precisely capture the microstructure of thin cerebral structures.
- Comparing the SNR efficiency of the 3D-msEPI approach to the classic acquisition methods: 2D-ssEPI and 2D-msEPI to demonstrate the added value of the developed pulse sequence at such resolution.

Materials and methods

I.1. DMRI pulse sequence design

The proposed diffusion-weighted acquisition pulse sequence was implemented to perform a 3D-sampling of k-space. A full description of the implemented 3D multishot-EPI (3D-msEPI) pulse sequence used in this study is available in the previous Chapter (section IV). The Stejskal-Tanner preparation scheme (Stejskal and Tanner, 1965) was then introduced into the pulse sequence to create diffusion weighting in MR images.

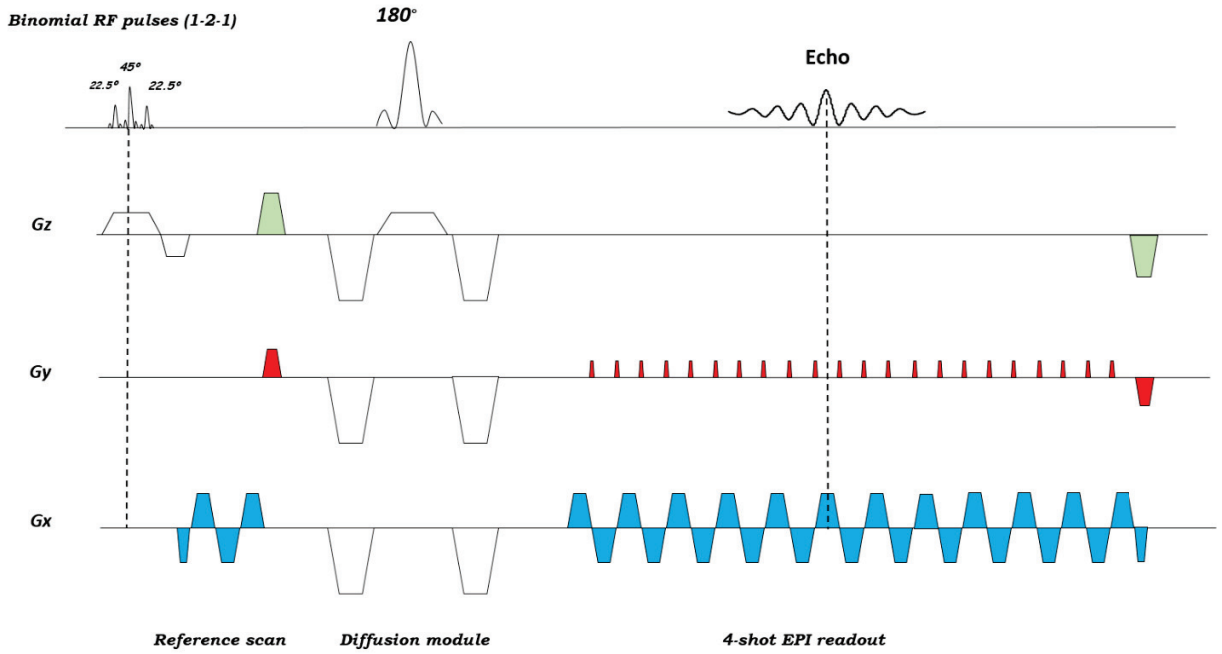

Figure IV.1: Diagram of the implemented Diffusion weighted EPI-based pulse sequence. Each k-space interleave (EPI readout) is preceded by an appropriate excitation RF pulse and a diffusion preparation module (orange trapezoid waveforms)

The RF excitation was performed using a binomial pulse, known as water excitation to address the chemical shift artifacts (Hauger et al., 2002). Slab-selective 90° (3.44 ms binomial pulses, bandwidth-time product of 5.2) and 180° (3.3 ms Sinc pulse) radiofrequency (RF) pulses were used

respectively for excitation and refocusing of spins inside the slab. The diagram of the 3D-msEPI dMRI pulse sequence is illustrated in Figure IV.1.

I.2. Protocol setup

In this study, *in-vivo* MRI scans were performed on a 3T Magnetom Prisma system (Siemens Healthineers, Erlangen, Germany). This Magnetic Resonance (MR) system is characterized by a maximum gradient amplitude of 80 mT/m and a maximum slew rate of 200 T/m/s. A whole body coil was used for RF transmission and three constructor loop coils with different diameters (two 11 cm, and one 7 cm) were used for MR signal reception. The 11 cm coils were placed on both sides of the head and the 7 cm coil on the top to fit the shape of the monkey head and to cover all the brain with maximum MR signal homogeneity (Fig.IV.2).

Figure IV.2: Schematic of the position of the 3 single-loop coils relative to the monkey's head.

Four healthy adults *Rhesus* macaques (*macaca mulatta*) were involved in this study: three males (9, 8 and 6 years old and 9, 9 and 7 kg respectively) and one female (5 years old and 6.5 kg). Before the MRI session, monkeys were first anesthetized with an intramuscular injection of ketamine (10mg\kg). Then, the subjects were intubated and maintained under 1.5% of isoflurane. During the scan, animals were placed in a sphinx position in a Kopf MRI-compatible stereotaxic frame (Kopf Instruments, Tujunga, CA). The head was carefully immobilized with a plastic mouth bite bar and two ear bars in order to avoid any motion of the head during the experiment. Cardiac and respiration rates as well as oxygen saturation level and expired CO_2 were continuously monitored and maintained in normal range (Li et al., 2013).

This study was authorized by the French Ministry for Higher Education and Research (project no. 20-12-0401-005) in accordance with the French transposition texts of Directive 2010/63/UE. This authorization was based on an ethical evaluation by the Ethical Committee for Animal Research registered as C2EA number 42.

I.3. MRI data acquisition

Pilot studies, not presented here, were led *in-vitro* and *in-vivo* in order to optimize acquisition parameters to achieve dMRI data with an isotropic spatial resolution of 0.5 mm using the proposed 3D-msEPI-based dMRI pulse sequence. The final acquisition parameters were set to: Repetition-Time (TR)=750 ms, Echo-Time (TE)=72 ms, bandwidth=776Hz/pixel, EPI-factor=53, number of k_{xy} EPI shots=4, Field Of View $(FOV)_{xyz}$=125×105×56 mm^3, matrix $size_{xyz}$=248×210×112 voxels, Partial Fourier factor along k_y direction=6/8, and along k_z direction=6/8 and phase encoding direction=Anterior-Posterior (AP).

30 Diffusion-Weighted (DW) axial images were acquired with b-value=1000 s/mm^2 applied along 30 non-collinear diffusion encoding directions (b1000-images). Diffusion direction vectors were generated using an electrostatic repulsion model (Caruyer et al., 2013) and are provided in Table IV.1. Two b0-images were also collected without diffusion weighting (b-value=0 s/mm^2) one before and one after the b1000-images. The total acquisition time of data was 130 minutes. One supplementary DW-image was acquired with b-value=0 s/mm^2 using the same acquisition parameters but with a reversed phase encoding direction (Posterior Anterior (PA)). This PA B0-image was used during the post-processing for susceptibility artifact correction.

In addition, 3D T1-weighted axial image was acquired for each subject using a magnetization-prepared rapid gradient-echo (MPRAGE) pulse sequence. Spatial resolution was set to 0.5 mm, matching dMRI data, with TR= 3000 ms, TE=3.62 ms, Inversion Time (TI) =1100 ms, flip angle=8°, bandwidth=250H z/pixel, turbo factor=144, FOV_{xyz}=160×105×72 mm^3 and matrix $size_{xyz}$=320×210×144 voxels.

I.4. Image post-processing

MR images were reconstructed with the Gadgetron framework (Hansen and Sørensen, 2013). Image reconstruction applied in this study includes a noise decorrelation step (or noise pre whitening) as described in Kellman et al (Kellman and McVeigh, 2005). Partial Fourier reconstruction is achieved by means of zero padding. The possible blurring effect of this procedure is expected to be the same in the image plane between the 2D and 3D-msEPI data. After reconstruction, images were converted into the NeuroImaging Informatics Technology Initiative (NII) format.

A visual quality control was performed on DW-images. Three scores were determined for each b0 and b1000-image by two experts according to: 1) The SNR, 2) The degree of residual ghosting due to the use of msEPI (Butts et al., 1996), 3) The spatial distortions. These scores were defined between 1 for the degraded images and 4 for images of high quality. According to these scores, 3D DW-images for which at least one of the double blind expert scores was inferior to 2 were considered as corrupted and were removed from the final data set.

Next, the susceptibility-induced off-resonance field was estimated from the pairs of b0-images acquired with direct (AP) and reversed (PA) phase encoding direction using the Topup procedure (Andersson et al., 2003) of FSL (FMRIB Software Library). The Eddy tool of FSL was then used to correct the susceptibilities, eddy currents effects and movements in DW-images (Andersson and Sotiropoulos, 2016). Finally, the spatial-intensity inhomogeneities of DW-images were estimated and corrected using the N4 algorithm (Tustison et al., 2010).

Diffusion encoding directions			
Direction	**Gx**	**Gy**	**Gz**
1	0.049	-0.919	-0.391
2	0.726	0.301	-0.618
3	-0.683	0.255	-0.684
4	0.845	-0.502	-0.186
5	-0.73	-0.619	-0.288
6	-0.051	0.039	0.998
7	-0.018	0.871	-0.491
8	-0.444	0.494	0.747
9	-0.989	-0.086	-0.116
10	-0.47	-0.855	0.221
11	0.412	0.4	0.819
12	-0.552	0.79	-0.267
13	-0.123	-0.477	0.871
14	-0.848	0.141	0.51
15	-0.341	-0.788	-0.512
16	0.361	-0.529	0.768
1	-0.472	0.85	0.234
18	-0.856	-0.481	0.189
19	0.797	0.162	0.582
20	0.467	-0.009	-0.884
21	0.013	0.998	-0.056
22	0.882	-0.387	0.267
23	0.017	-0.536	-0.844
24	-0.442	-0.651	0.617
25	0.365	-0.058	0.929
26	0.977	-0.004	-0.213
27	-0.406	-0.902	-0.145
28	-0.627	0.614	0.479
29	-0.354	0.772	-0.528
30	-0.658	-0.472	-0.586

Table IV.1: The 30 diffusion direction vectors used in the dMRI acquisition

Diffusion tensor maps (the eigenvalues (λ_1, λ_2, λ_3), Axial Diffusivity (AD), Radial Diffusivity (RD), Mean Diffusivity (MD) and Fractional Anisotropy (FA)), were computed from the acquired dMRI datasets using the MRtrix3 software (Tournier et al., 2012). From the λ_1, λ_2 and λ_3 values, the sphericity coefficient (Cs), planicity coefficient (Cp) and linearity coefficient (Cl) were extracted. These coefficients were respectively computed as $Cs=3.\lambda_3 / (\lambda_1 + \lambda_2 + \lambda_3)$, $Cp=2.(\lambda_2 - \lambda_3)/(\lambda_1 + \lambda_2 + \lambda_3)$ and $Cl= (\lambda_1 - \lambda_2)/(\lambda_1 + \lambda_2)$ (Westin et al., 2002).

All the tractography processes were performed with MRtrix3 (Tournier et al., 2007, 2004). The tractography approach is based on the definition in each voxel of the Fiber Orientation Distribution (FOD) using spherical deconvolution (Tournier et al., 2007, 2004). The response function was estimated from the data and the spherical deconvolution was applied with a spherical harmonics order of 6 and a number of iterations of 200. A whole brain tractography, consisting of 2,000,000 streamlines, was then performed with the probabilistic fiber-tracking algorithm (iFOD2) (Tournier and , F. Calamante, 2010) using an angle threshold criterion of 40° and a FOD threshold of 0.25.

To test the efficiency of high spatial resolution to analyze small structures in the macaque brain, DW-images acquired at an isotropic spatial resolution of 0.5 mm were down-sampled using linear interpolation to generate another dMRI dataset with a 1 mm^3 cubic voxel size. The average of the signal of 8 0.5mm voxels was assigned to the corresponding one 1mm voxel. Thus, no spatial smoothing is applied on top of this averaging process to avoid any hyper-signal. The partial volume effect is restricted to the decrease in spatial resolution from 0.5 to 1mm. This is the spatial resolution currently achieved to study macaque brain using standard dMRI pulse sequences based on 2D-ssEPI.

I.5. Data quantification

To quantify SNR of dMRI data achieved at a spatial resolution of 0.5 mm, three Regions Of Interests (ROI) were manually drawn on FA maps at the same location for each monkey (Fig.IV.3). Two White Matter (WM) ROIs were located in the Corpus Callosum (CC) and in the Posterior Limb of Internal Capsule (PLIC), and one Grey Matter (GM) ROI was located in the Superior and Middle Temporal Gyrus (S/M TG). Table IV.4 shows the size of each ROI. A fourth ROI was positioned in the background of the images in order to assess the standard deviation of noise.

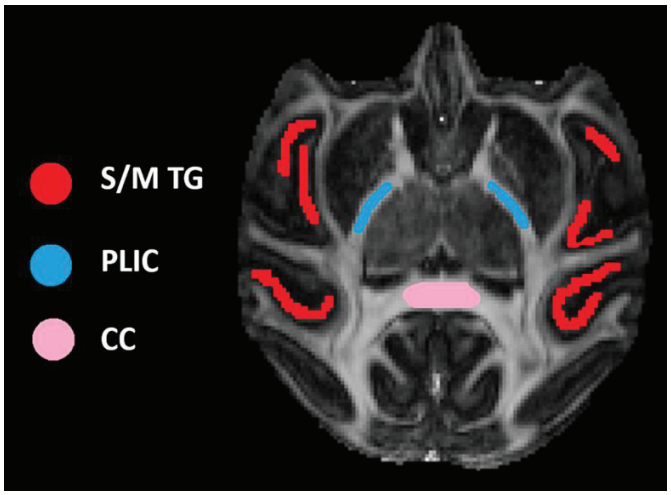

Figure IV.3: Location of the Regions Of Interests (ROIs) used for ROI-based analysis. These include ROIs for White Matter, one located in the Corpus Callosum (CC) and two in the Posterior Limb of the Internal Capsule (PLIC) respectively. For Grey Matter, several ROIs were located in the Superior and Middle Temporal Gyrus (S/M TG).

For each subject, SNR values were computed in each of the 3 ROIs for the 2 b0-images and 30 b1000-images as the ratio of the mean signal within the ROIs to the standard deviation of the noise. The measured SNR values were then averaged to obtain one SNR_{b0} and one SNR_{b1000} for each of the three ROIs.

Furthermore, the same three ROIs described above were used to quantify diffusion tensor metrics (FA, MD, AD and RD). For each subject, mean values ± standard deviation were computed for each of the three ROIs and for each diffusion tensor metric.

I.6. Tractography

Dissections of well-known white matter bundles, such as the cingulum bundle (CB) and the fornix (Fx) are presented in this study and were made by using a multiple dissection ROI approach (note that these dissection ROIs are different from the above quantification ROIs). Tractography was then performed, on the high (0.5 mm) and low (1 mm) resolution DW datasets, with exactly the same dissection ROIs. Between the high resolution and low resolution, the step size parameters were kept constant for the tracking step, equal to half the voxel size.

I.7. Comparison between dMRI pulse sequences based on 3D-EPI and 2D-EPI

Additional datasets were acquired using three methods, 3D-msEPI, 2D-msEPI and the gold standard 2D-ssEPI, in order to evaluate the SNR efficiency for the 3D-msEPI approaches. The data were acquired on one monkey brain during the same MRI session.

Parameters	3D msEPI	2D msEPI	2D ssEPI
TR (ms)	**750**	**15200**	**41200**
TE (ms)	**72**	**72**	**186**
FOV (mm)	**125*105**	**125*105**	**125*105**
Matrix size (pixel)	**248*210**	**248*210**	**248*210**
Spatial resolution (mm^3)	**0.5*0.5*0.6**	**0.5*0.5*0.6**	**0.5*0.5*0.6**
Bandwidth (Hz/pixel)	**776**	**776**	**776**
Partial Fourier Factor (ky)	**6/8**	**6/8**	**6/8**
Partial Fourier Factor (kz)	**6/8**	**-**	**-**
Scan time	**4m10s**	**4m18s**	**4m04s**

Table IV.2: Scan parameters used for the different 3D-msEPI, 2D-msEPI and 2D-ssEPI dMRI pulse sequences

DW-images were acquired with b-value = 0 s/mm^2 and b-value = 1000 s/mm^2 using each of the three pulse sequences, with the following parameters: FOV_{xyz} = 125×105×67.2 mm^3, matrix $size_{xyz}$ = 248×210×112 voxels, Partial Fourier factor along k_y direction = 6/8, phase encoding direction = AP. The slice thickness was set to 0.6 mm in all acquisitions to follow the hardware limits of the 2D-EPI pulse sequences. The 2D-EPI acquisitions were averaged to match the same scan time as the 3D-msEPI, i.e. 4 minutes for a complete brain volume coverage. The following parameters were used:

- 3D-msEPI: TR = 750 ms, TE = 72 ms, 4 shots, partial Fourier factor of 6/8 in k_z
- 2D-msEPI: TR = 15200 ms, TE = 72 ms, 4 shots, 4 averages, (140 ms per slice, scan time 4m18s)

- 2D-ssEPI: TR = 41200 ms, TE = 186 ms, 5 averages (390 ms per slice, scan time 4m04s)

Table IV.2 recapitulates the acquisition parameters of each of the 2D-ssEPI, 2D-msEPI and 3D-msEPI dMRI pulse sequences used in this comparison.

A direct SNR comparison was performed between DW datasets collected using the 3D-msEPI and the 2D-msEPI pulse sequences. SNR maps were computed from each of these two datasets, for both b0 and b1000-images, by dividing the intensity of each pixel of the image by the standard deviation of noise measured within two ROIs delineated in the background of the image. The obtained SNR maps were smoothed by a Gaussian kernel of 1 mm. Then, colored maps were computed pixel-by-pixel as the ratio of the 3D-msEPI SNR map to the 2D-msEPI SNR map.

Results

I.8. Comparison between SNR efficiencies of 2D-ssEPI, 2D-msEPI and 3D-msEPI

To compare the proposed acquisition method with the classic 2D techniques, dMRI images were acquired with 3D-msEPI, 2D-msEPI and 2D-ssEPI with similar experimental conditions, matching the same scan time per volume of about 4 minutes (see paragraph II.7). Figure IV.4 presents the obtained images. The left column shows the images acquired with b-value=0 s/mm^2, the right column displays the images acquired with b-value=1000 s/mm^2.

Three major differences can be observed between the three data sets. First, the SNR was significantly higher in the images collected using the 3D-msEPI pulse sequence for both b0 and b1000-images. Second, the image distortions were more important for the images collected using the 2D-ssEPI module because of its large echo train length. Third, the use of a short TR (750 ms) for the 3D-msEPI acquisition led to a different contrast of brain tissues compared to that obtained using 2D-EPI sampling of k-space with a longer TR.

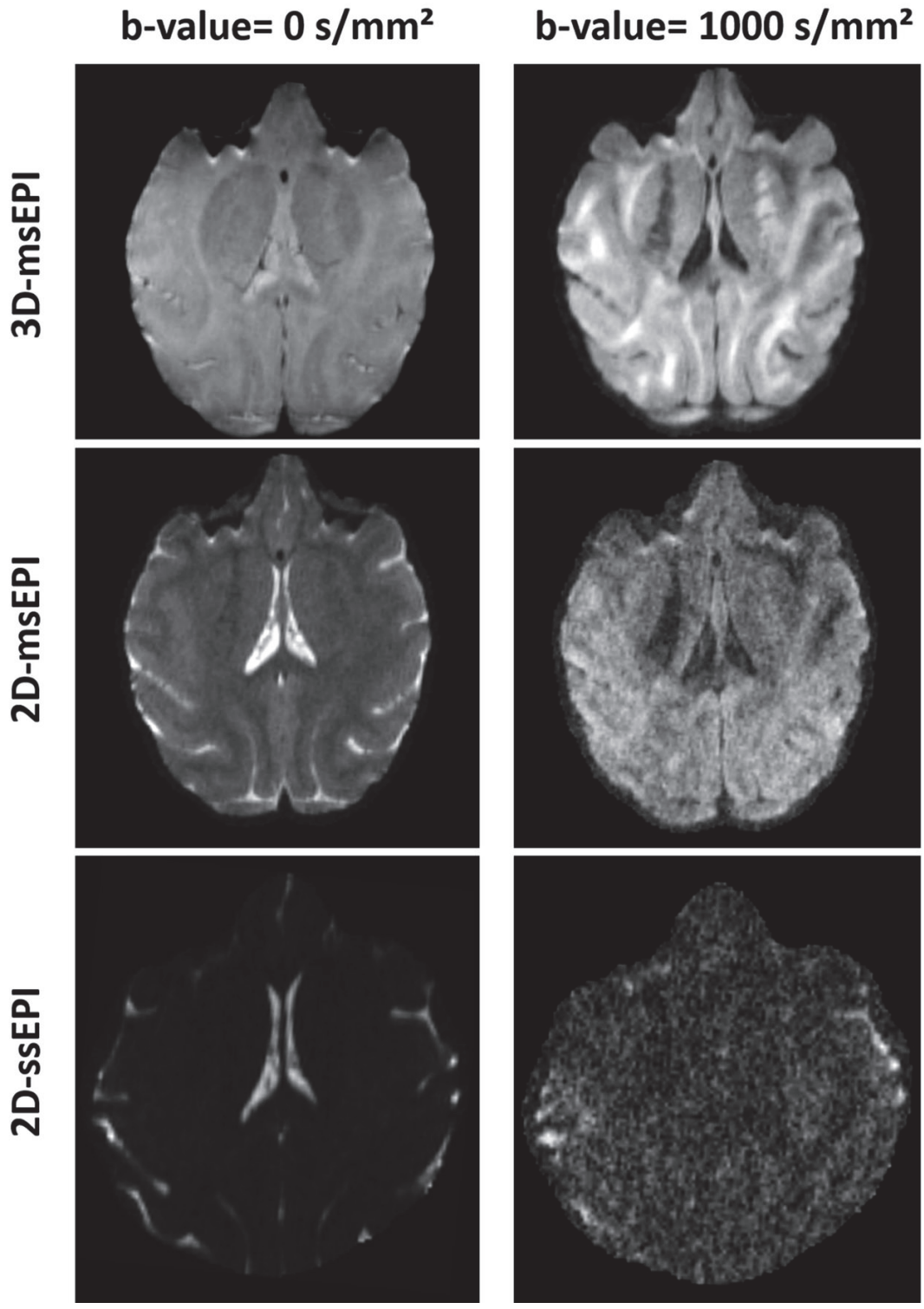

Figure IV.4: Comparison between images acquired with and without diffusion weighting using 3D Multi-shot Echo Planar Imaging (3D-msEPI), 2D Multi-shot Echo Planar Imaging (2D-msEPI) and 2D Single-Shot Echo Planar Imaging (2D- ssEPI) sampling of k-space.

More specifically, the computed $SNR_{3D\text{-}msEPI}$/ $SNR_{2D\text{-}msEPI}$ maps are shown in Figure IV.5. For images acquired with b-value=0 s/mm^2, the ratio of $SNR_{3D\text{-}msEPI}/SNR_{2D\text{-}msEPI}$ was about 4 for the WM and about 3 for the GM in the ROIs of interest. This ratio increased to be about 4.7 for WM at a b-value=1000 s/mm^2, Table IV.3 presents the measured values of $SNR_{3D\text{-}msEPI}/SNR_{2D\text{-}msEPI}$ 2D-msEPI ratio.

	$SNR_{3D\text{-}msEPI}$ to $SNR_{2D\text{-}msEPI}$ of b-value=0 s/mm^2 images	**$SNR_{3D\text{-}msEPI}$ to $SNR_{2D\text{-}msEPI}$ of b-value=1000 s/mm^2 images**
Corpus Callosum	3.71	4.45
PLIC	4.19	4.99
Grey Matter	3.03	3.36

Table IV.3: Mean values of the ratio of SNR3D-msEPI to SNR2D-msEPI measured in Corpus Callosum, Posterior Limb of the Internal Capsule (PLIC) and in Grey Matter. This ratio is assessed for images acquired with b-value=0 s/mm^2 and b-value=1000 s/mm^2.

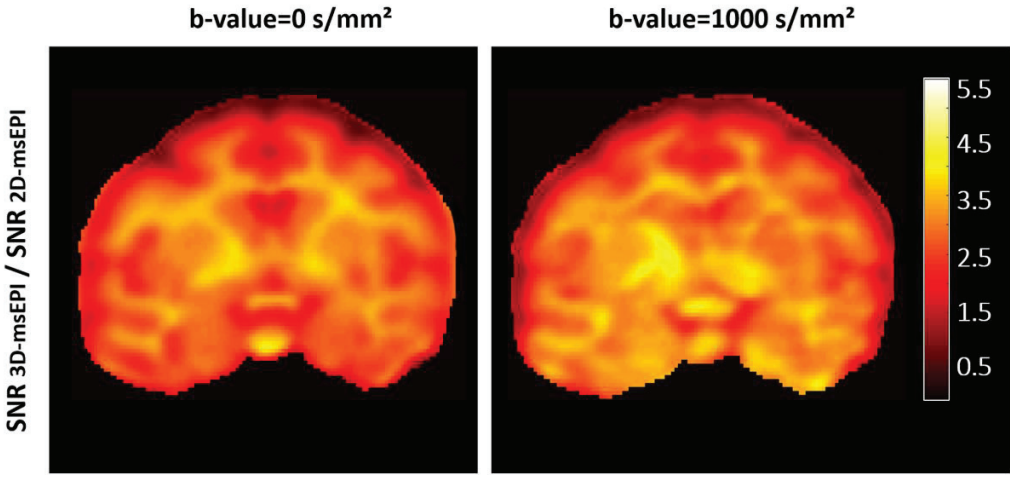

Figure IV.5: SNR improvements between dMRI data acquired using 3D Multi-shot Echo Planar Imaging (3D-msEPI) and 2D-msEPI with b-value=0 s/mm^2 and-value with b-value=1000 s/mm^2

I.9. High-resolution dMRI of macaque brain

DMRI data with an isotropic spatial resolution of 0.5 mm were successfully collected from all the four subjects involved in this study. During the quality control procedure, all the data obtained high scores in terms of SNR and of absence of geometric distortion artifacts. 10 diffusion-weighted images distributed among the 4 subjects (0 image from subject #1, 4 images from subject #2, 6 images from subject #3 and 0 images from subject #4; 7.8% of the total number of diffusion weighted images collected from the 4 subjects) were scored as corrupted because of blurring and ghosting which could be due to physiological motions and pulsations occurring inside the skull and/or to residual head motions.

These corrupted DW-images were removed from dMRI datasets before applying the post-processing pipeline. Figure IV.6 shows an example of images with b-value of 0 s/mm^2 (b0-image) and 1000 s/mm^2 (b1000-image) before (A and B) and after (C and D) the application of the data post-processing procedures (correction of susceptibilities and eddy current effects and intensity normalization).

	Voxels per ROI	**b-value=0 s/mm^2 images (Mean ± SD)**	**b-value=1000 s/mm^2 images (Mean ± SD)**
Corpus Callosum	**152±20**	**74.07±3.24**	**35.01±4.93**
PLIC	**109±28**	**64.95±3.88**	**30.53±5.76**
Grey Matter	**218±41**	**67.20±11.21**	**32.85±0.23**

Table IV.4: Mean ± SD of Signal to Noise Ratio (SNR) of MR images collected from the 4 monkeys with an isotropic spatial resolution of 0.5 mm. SNR values are measured in Corpus Callosum, Posterior Limb of the Internal Capsule (PLIC) and Superior and Middle Temporal Gyrus Grey Matter (see figure 4.2) from images collected with b-value=0 s/mm^2 and with b-value=1000 s/mm^2

Table IV.4 summarizes the mean values ± Standard Deviations (SD) of SNR values experimentally measured for the 4 subjects from white (Corpus Callosum (CC) and Posterior Limb of Internal Capsule (PLIC)) and grey matter ROIs at b-values of 0 s/mm^2 and 1000 s/mm^2. Across all brain voxels, the SNR values, measured from b1000-images, are inferior to that of b0-images but remain high enough (superior to 25) to allow computing DTI maps and to performing fiber tractography.

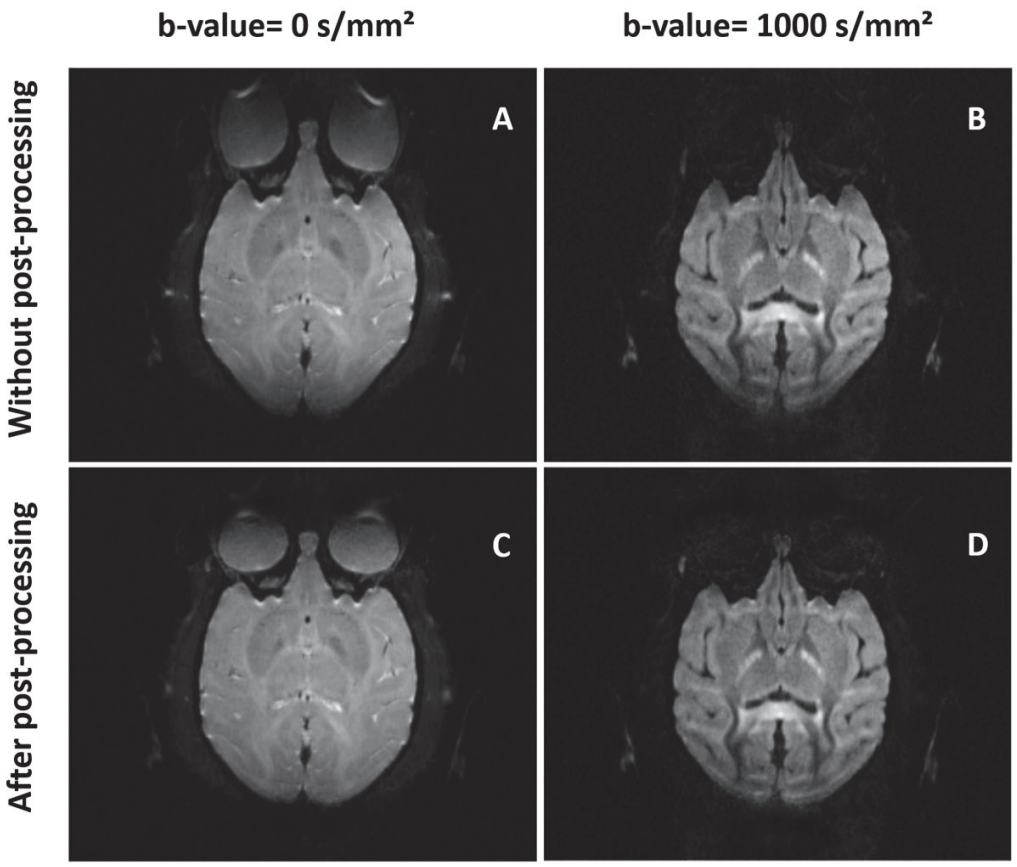

Figure IV.6: Axial views of the b0 (A and C) and b1000-images (B, D) before (top row) and after (bottom row) the corrections of susceptibilities and eddy currents effect and the intensity normalization

	FA ***(Mean ± SD)***	**MD (10^{-3} mm²/s)** ***(Mean ± SD)***	**AD (10^{-3} mm²/s)** ***(Mean ± SD)***	**RD (10^{-3} mm²/s)** ***(Mean ± SD)***
Corpus Callosum	0.85±0.01	0.74±0.02	1.76±0.06	0.23±0.01
PLIC	0.76±0.01	0.79±0.07	1.69±0.14	0.35±0.03
Grey Matter	0.22±0.02	0.74±0.03	0.92±0.06	0.65±0.03

Table IV.5: Mean ± SD values of DTI parameters (Fractional Anisotropy (FA), Mean Diffusivity (MD), Axial Diffusivity (AD) and Radial Diffusivity (RD)) measured in the 4 monkeys in the selected Corpus Callosum, Posterior Limb of the Internal Capsule (PLIC) and Grey Matter ROIs

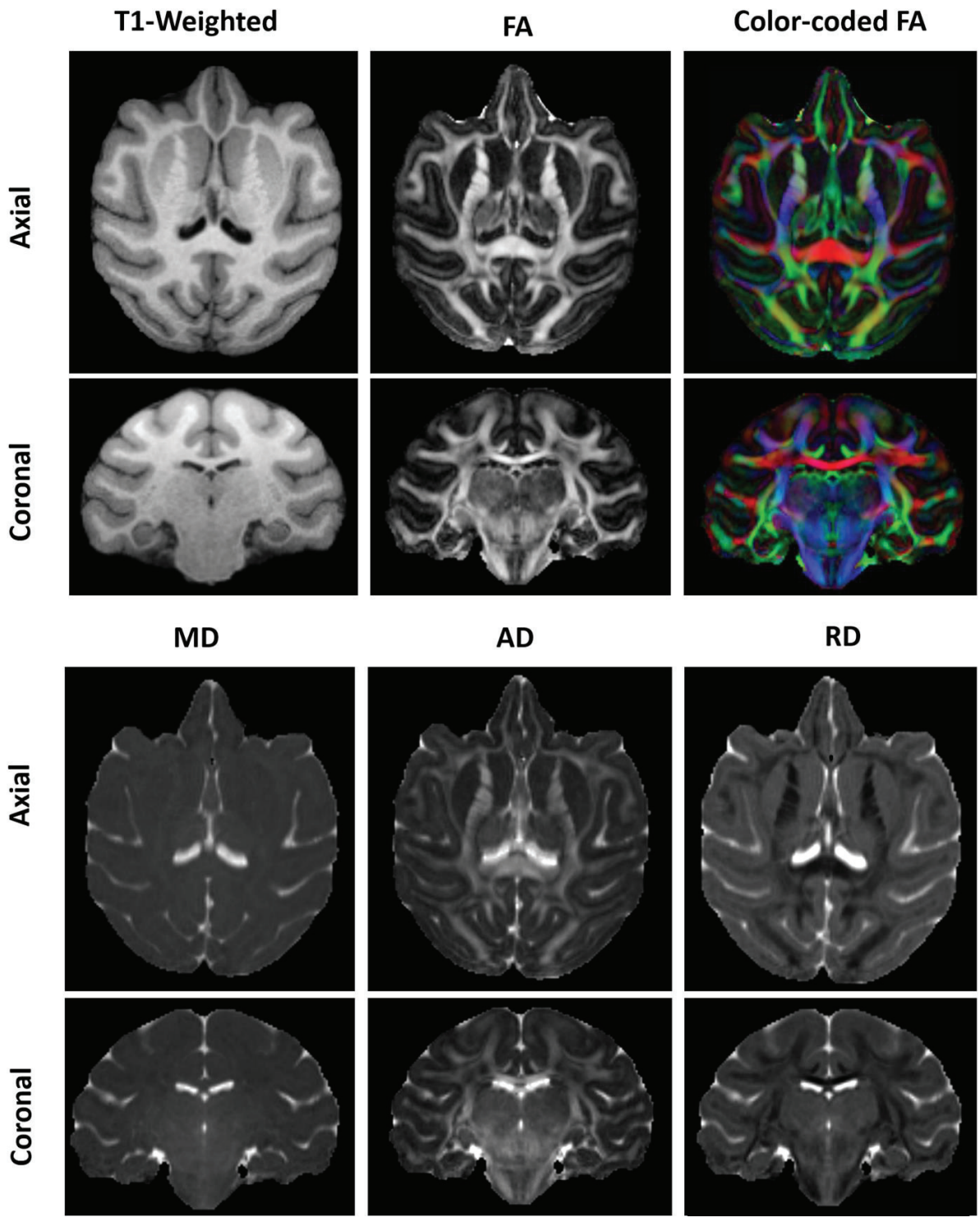

Figure IV.7: Selected Axial and Coronal views of monkey brain anatomical T1-weighted images and DTI maps (Fractional Anisotropy (FA), Color-coded FA, Mean Diffusivity (MD), Axial Diffusivity (AD) and Radial Diffusivity (RD)) at an isotropic resolution of 0.5 mm.

High quality DTI maps were obtained from dMRI data acquired at an isotropic resolution of 0.5 mm using the 3D-msEPI. Figure IV.7 shows an example of axial and coronal views of DTI maps (FA, Color-coded FA, MD, AD and RD) acquired in one of the monkeys. The same fine anatomical features are clearly visible both on the anatomical images (Fig.IV.7, left column, T1-weighted images acquired with a spatial isotropic resolution of 0.5 mm) and on the DTI maps (Fig.IV.7, middle and right column). However, additional details can be seen on the FA maps allowing to distinguish the finest anatomic structures.

	FA	**MD (10^{-3} mm²/s)**	**AD (10^{-3} mm²/s)**	**RD (10^{-3} mm²/s)**
Corpus Callosum (CC)	0.854 ± 0.013	0.743 ± 0.023	1.768 ± 0.06	0.230 ± 0.019
Genu of CC	0.77 ± 0.049	0.786 ± 0.1	1.69 ± 0.12	0.338 ± 0.09
Splenium of CC	0.741 ± 0.098	0.956 ± 0.16	1.98 ± 0.07	0.441 ± 0.2
Optic Nerve	0.78 ± 0.11	0.934 ± 0.14	2 ± 0.09	0.4 ± 0.02
PLIC	0.766 ± 0.009	0.795 ± 0.077	1.69 ±0.145	0.351 ± 0.039
Grey Matter	0.224 ± 0.026	0.741 ±0.039	0.923 ± 0.063	0.650 ± 0.031
CSF	0.044 ± 0.003	2.898 ± 0.329	3.033 ± 0.334	2.849 ± 0.307

Table IV.6: Mean ± SD values of DTI parameters (Fractional Anisotropy (FA), Mean Diffusivity (MD), Axial Diffusivity (AD) and Radial Diffusivity (RD)) measured in the 4 monkeys in the selected Corpus Callosum (CC), Genu of CC, Splenium of CC, Optic Nerve, Posterior Limb of the Internal Capsule (PLIC), Grey Matter and Corticospinal Fluid (CSF) ROIs.

Moreover, the Color-coded FA maps allow to define the organization of fiber bundles within the white matter, according to their main directions (red= left-right, green= Anterior-Posterior and blue= Inferior-superior). This level of descriptive information cannot be provided by T1-weighted images of equal resolution. Table IV.5 summarizes the values of FA, MD, AD and RD measured

from the 4 monkeys in the selected WM (CC and PLIC) and GM ROIs. Table IV.6 provides water diffusion metrics assessed in additional ROIs.

Most interestingly, FODs obtained with a spatial resolution of 0.5 mm captured the complex WM organization (Fig.IV.8 A and B). For example, the obtained FODs illustrated high anisotropy in the CC and Corticospinal tracts (CST), and clearly indicated the crossing fiber regions in the Centrum Semiovale region of the brain (CSO), where crossings between the CC, the superior longitudinal fasciculus and the Corticospinal tracts is known to occur (Descoteaux et al., 2007; Fortin et al., 2012) .

The tracking of these 3 components is proposed in the figure (Fig.IV.8 C, D, E, and F) and indicates the reliability with which we can extract the three bundles. Likewise, these FODs also captured the interface between WM and GM. For example, a clear transition in local tissue anisotropy can be seen between arcuate sulcus GM and adjacent WM (Fig.IV.10).

I.10. Benefits of using an isotropic spatial resolution of 0.5 mm in dMRI of macaque brain

To demonstrate the added value of achieving dMRI data at a spatial resolution of 0.5 mm instead of the millimetric resolution commonly used *in-vivo* to study macaque brain, DTI-maps were reconstructed with 1 mm^3 cubic size voxels by down-sampling the original 0.5 mm dMRI data (see II.4). Figure IV.9 visually illustrates the FA maps obtained with a spatial resolution of 0.5 mm and one of 1 mm. Clear differences in anatomical definition can be seen, both in WM organization and in GM definition.

To illustrate the benefits of high-resolution dMRI to analyze small cerebral structures in the macaque brain, we focused on the hippocampus and WM/GM interface. Figure IV.10 shows that at a spatial resolution of 0.5 mm, some internal substructures of the hippocampus become distinguishable.

The resolution of 0.5 mm is also beneficial to analyze the thin superficial-WM located between the deep-WM and the cortex-GM. The superficial-WM is mainly composed of short association fibers (U-fibers) connecting adjacent gyri (Schmahmann and Pandya, 2006).

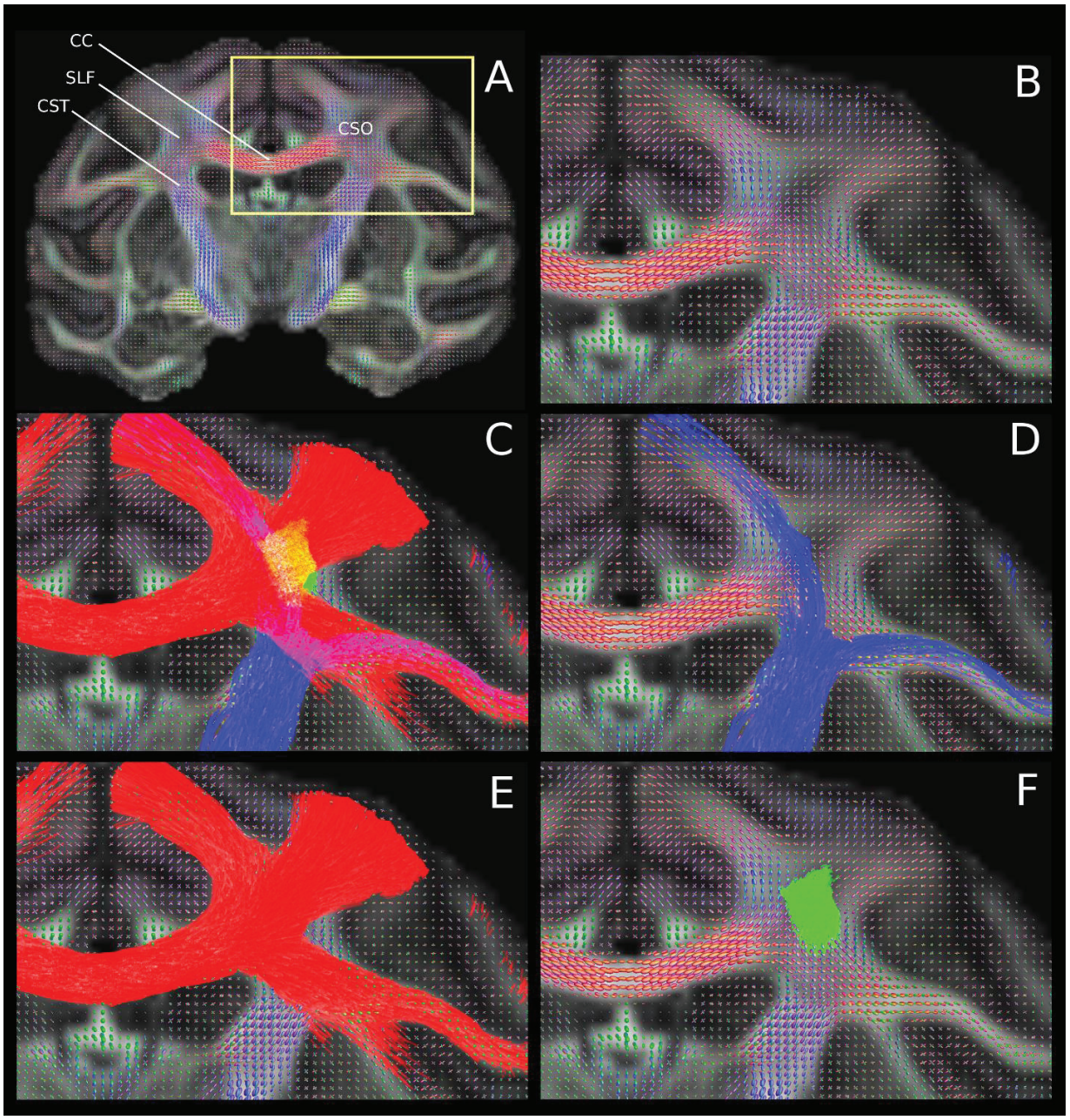

Figure IV.8: Representation of the high-resolution Fiber Orientation Distribution (FOD) centered on the centrum Semiovale on a coronal slice of the Fractional Anisotropy map. One can see on the zoomed box the crossing fibers between the Corpus Callosum (CC), the Corticospinal Tract (CST), and the Superior Longitudinal Fasciculus (SLF). Tracking results of the CST (blue tracts), CC (red tracts) and SLF (green tracts) passing through the centrum Semiovale region are shown in (C, D, E and F).

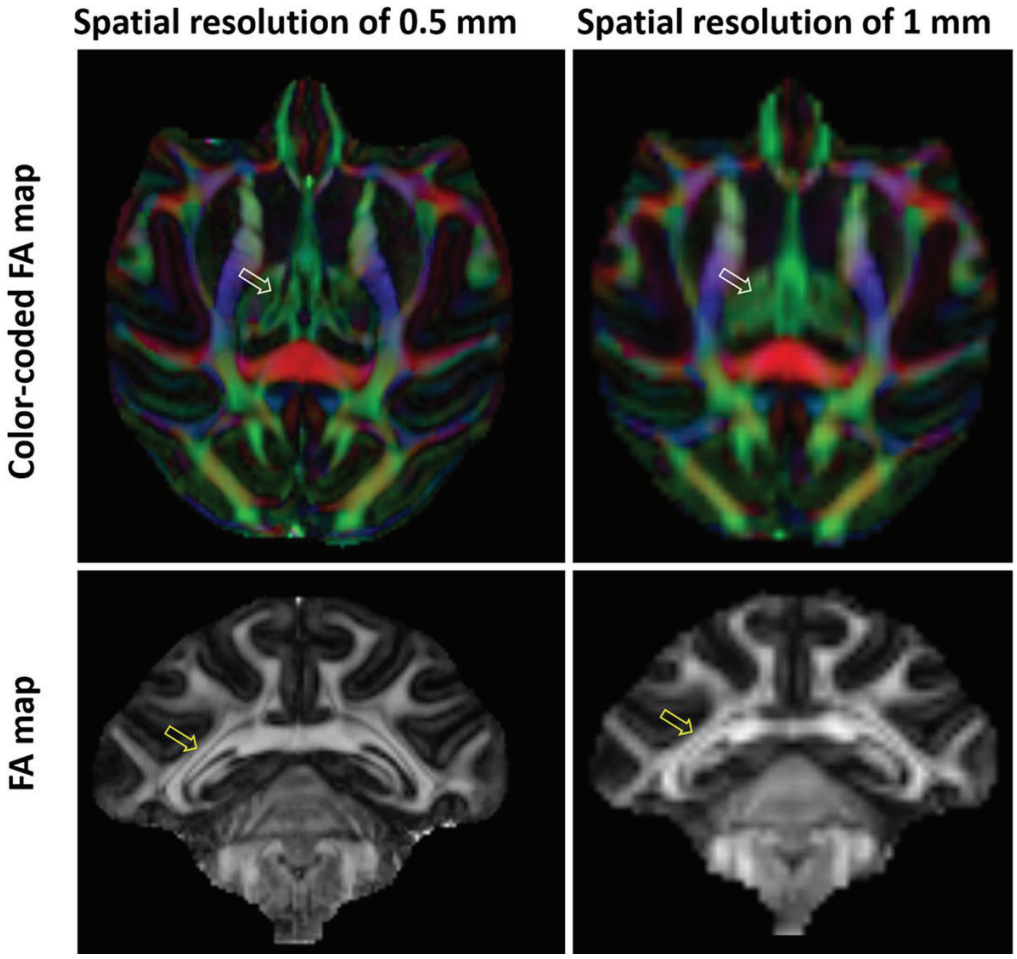

Figure IV.9: Visual comparison between Fractional Anisotropy (FA) maps obtained with isotropic spatial resolutions of 0.5 mm (left column) and 1 mm (right column). The 1 mm data were obtained by down-sampling the 0.5 mm data. An example of thin anatomic details that can be seen only at a spatial resolution of 0.5 mm, are indicated by arrows

The high-resolution dMRI data achieved in this study allowed the detection of the U-fibers described in the *ex-vivo* macaque brain by Oishi et al. (Oishi et al., 2011). Figures IV.11 focuses on the Central Sulcus (CS) and the Arcuate Sulcus (AS). U-fibers appear with high values on FA, λ_1 and CL. The 0.5 mm resolution enables to visualize cortex-GM with a thickness of 2-4 pixels, and the U-fiber with a thickness of 1-3 pixels surrounded by one-voxel-thick cortex-GM/superficial-WM and deep-WM/superficial-WM interfaces. These interfaces could correspond to partial volume effects introduced by the change of axon orientations at the boundaries of the superficial-WM.

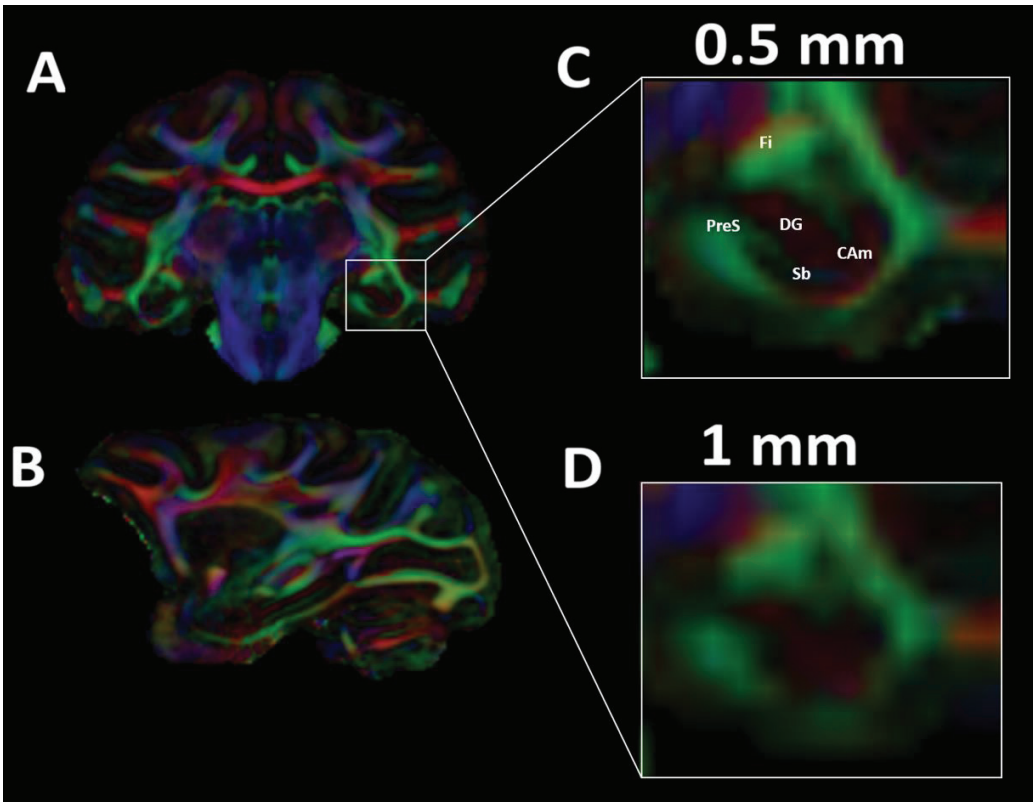

Figure IV.10: Coronal and sagittal views (A and B) of Color-coded fractional anisotropy map at a spatial resolution of 0.5 mm. C shows a zoom on the hippocampus region delimited by the white box in A . D presents the same zoom but with a spatial resolution of 1 mm. The spatial resolution of 0.5 mm allows a precise identification of internal anatomical sub-structures of the hippocampus, such as the SuBiculum (Sb), the Pre-Subiculum (PreS), the Cornu Ammonis (CA) and the Dentrate Gyrus (DG).

On a low-resolution image, one U-fiber and its interface with cortex-GM and with deep-WM is contained inside one to two pixels at the most. The values of water diffusion metrics (in terms of FA, λ_1, λ_2, λ_3 and Cl) of these pixels are very influenced by partial volume effects (Fig.IV.11).

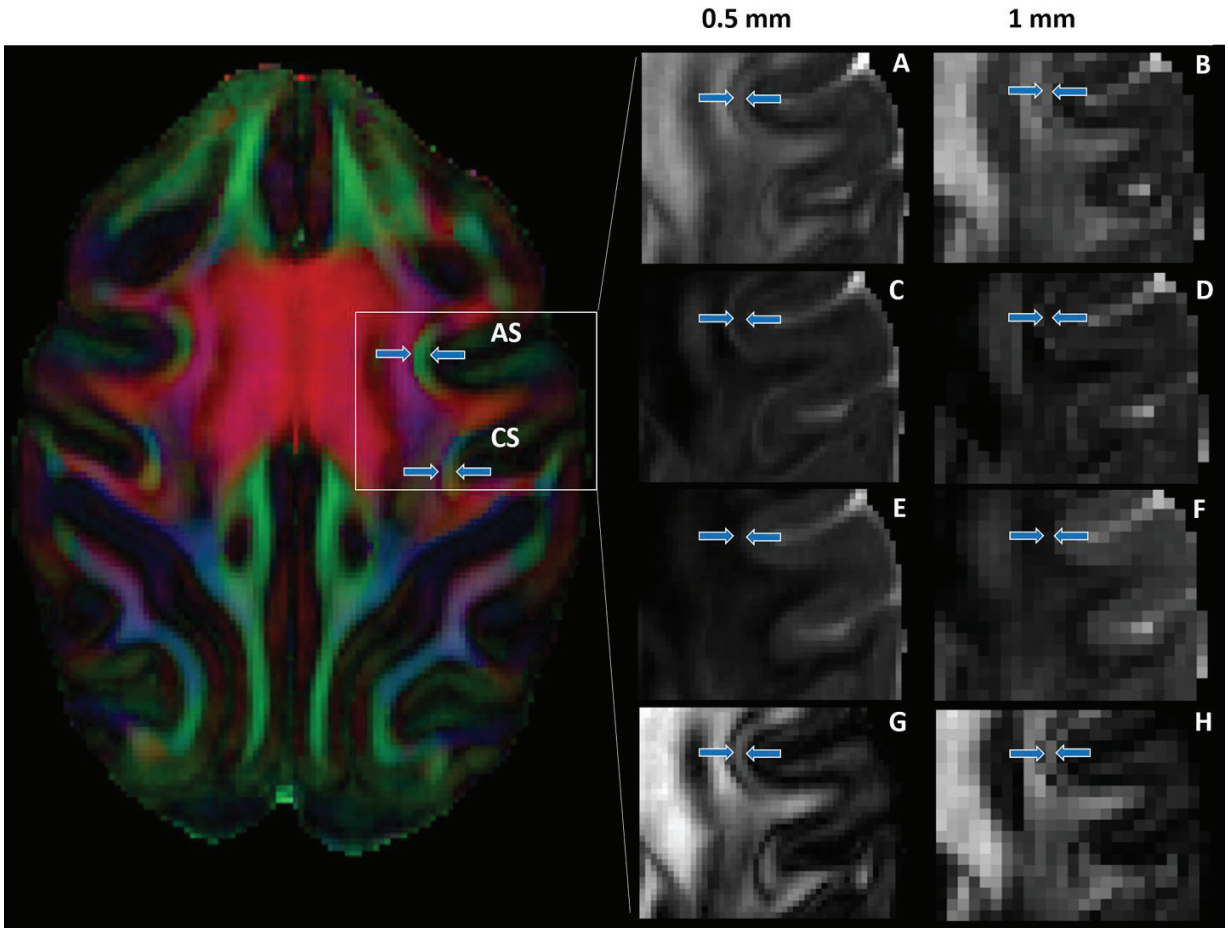

Figure IV.11: Axial view of Color-coded FA of a monkey brain. The zoomed box shows the Central Sulcus (CS) and the Arcuate Sulcus (AS). The U-fiber indicated by blue arrows on eigenvalue λ1 map (A, B), on eigenvalue λ2 map (C, D), on eigenvalue λ3 map (E, F) and on linearity coefficient map (G, H) at a spatial resolution of 0.5 mm (left column: A, C, E and G) and of 1 mm (right column: B, D, F and H). In high-resolution data, the organization of cortical grey matter, U-fiber and deep white mater are better distinguishable and less corrupted by the partial volume effects.

Figure IV.12 illustrates the orientation of superficial-WM and deep-WM fibers around the Arcuate Sulcus as revealed by the main direction of the diffusion tensor (Fig.IV.12.A) and by peaks extracted from the FODs (Fig.IV.12.B).

In the fundus of the Arcuate Sulcus, the main diffusion tensor orientation of Superficial-WM is

parallel to the U-fibers. Whereas, the peaks extracted from the FOD (Fig.IV.12.b) indicates a secondary diffusion component orientated perpendicularly to the U-fibers. This peak component was not detected by Reveley in *ex-vivo* data (Reveley et al., 2015).

On the fundus of the gyri, the penetration of fibers originating from deep-WM and from U-fibers into cortex-GM is clearly detectable using both the diffusion tensor orientation and FOD peaks. The trajectory of the WM fibers is harder to estimate using the 1-mm dMRI data (Fig.IV.12.C and D). An additional Figure IV.13 presents for each animal involved in this study: an axial Color-coded FA map, an axial FA map and FODs peaks centered on the fundus of the Arcuate Sulcus.

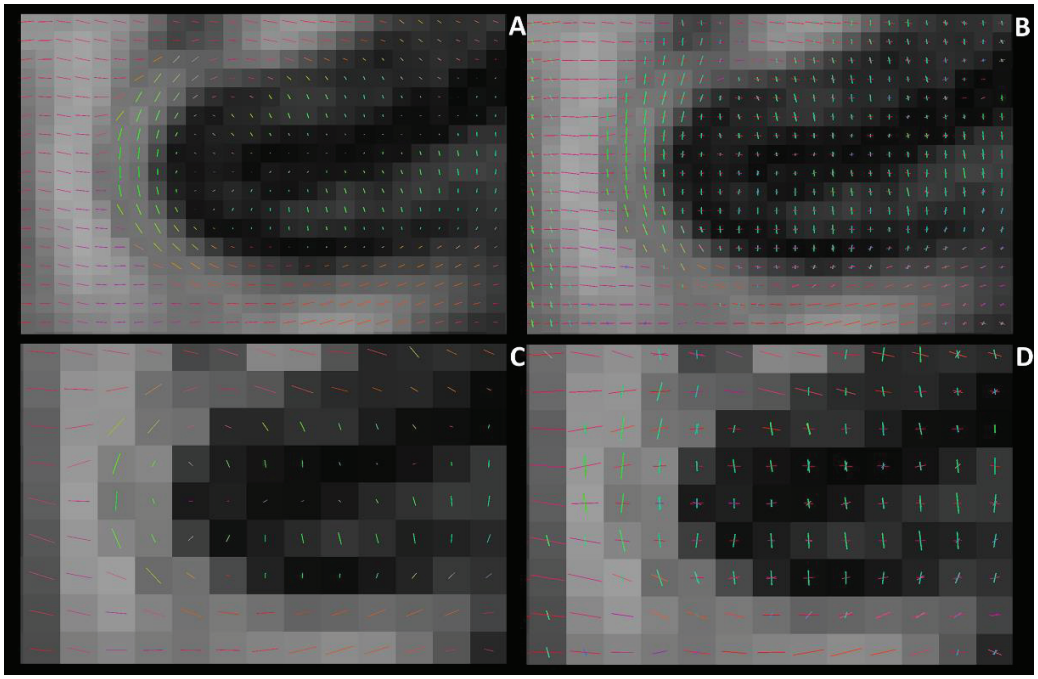

Figure IV.12: Main direction of water diffusivity estimated from the diffusion tensor data with a spatial resolution of 0.5 mm and 1 mm (A and C respectively), and from thresholded peaks extracted from the FODs with a spatial resolution of 0.5 mm and 1 mm (B and D respectively). All the directions are visualized on the fractional anisotropy map centered on the Arcuate Sulcus.

Figure IV.14 presents an example of the cingulum or Cingulate Bundle (CB) and the Fornix (FX) bundles obtained from high-resolution dMRI data of one of the 4 monkeys using tractography. The reconstructed CB is located in the cingulated gyrus just above the Corpus Callosum (CC) on the medial wall of the brain.

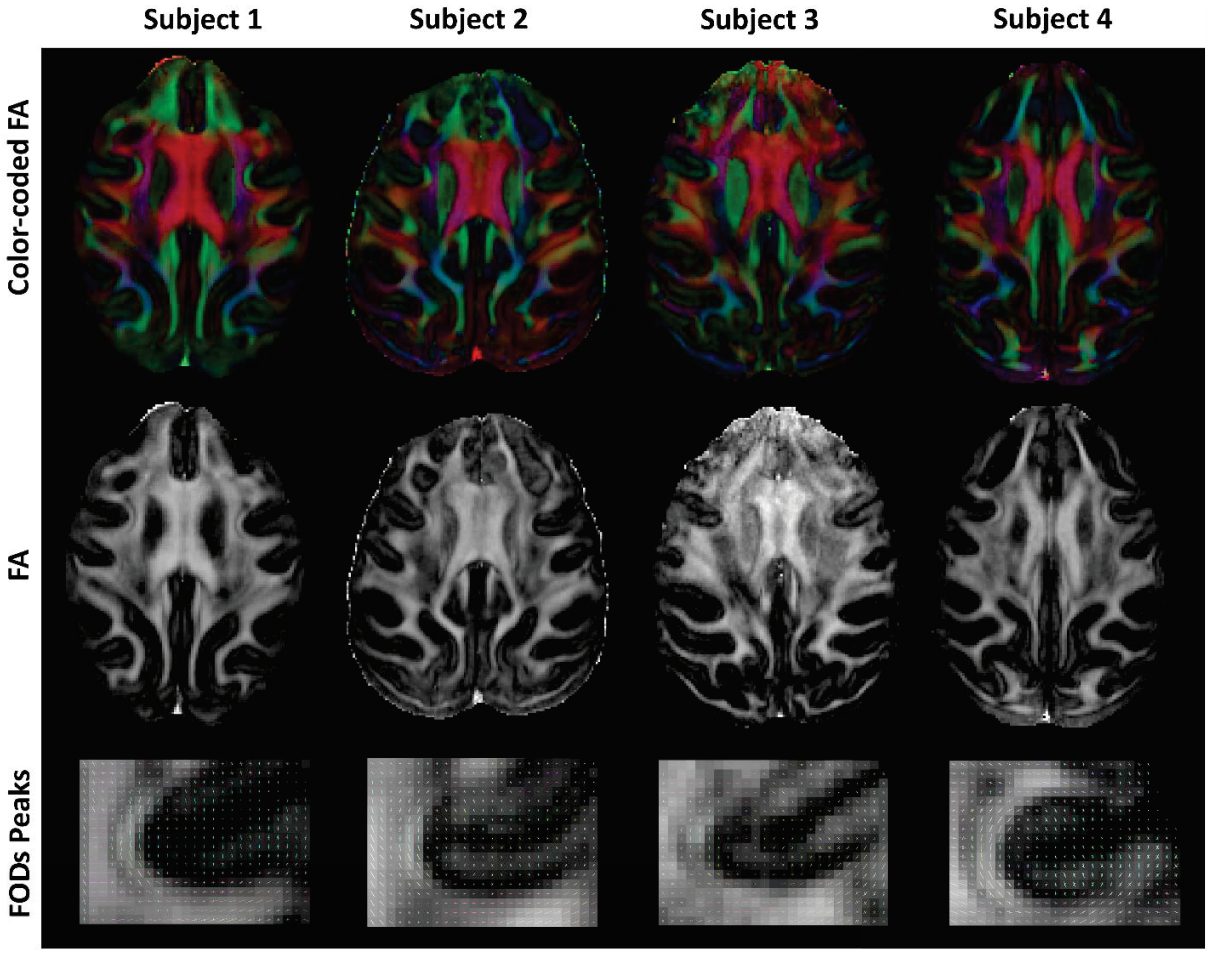

Figure IV.13: Axial views of Color-coded Fractional Anisotropy (FA), Fractional Anisotropy (FA)) obtained on each of the four macaques monkey at an isotropic resolution of 0.5 mm. For each animal, the thresholded peaks extracted from the Fiber Orientation Distributions (FODs) are visualized on the FA map and centered on the arcuate sulcus region.

It branches posteriorly down around the splenium of the Corpus Callosum into the parahippocampal gyrus (PH) before terminating in the Entorhinal Cortex (EC), located in the medial temporal lobe. Anteriorly, it arches down around the genu of the Corpus Callosum towards the paraterminal gyrus (PT) (Fig.IV.14.A). The branching of the CB towards Posterior Cingulate Cortex (PCC), Anterior Cingulate Cortex (ACC) and medial prefrontal cortex (mPFC) can also be seen clearly on Figure IV.14.A.

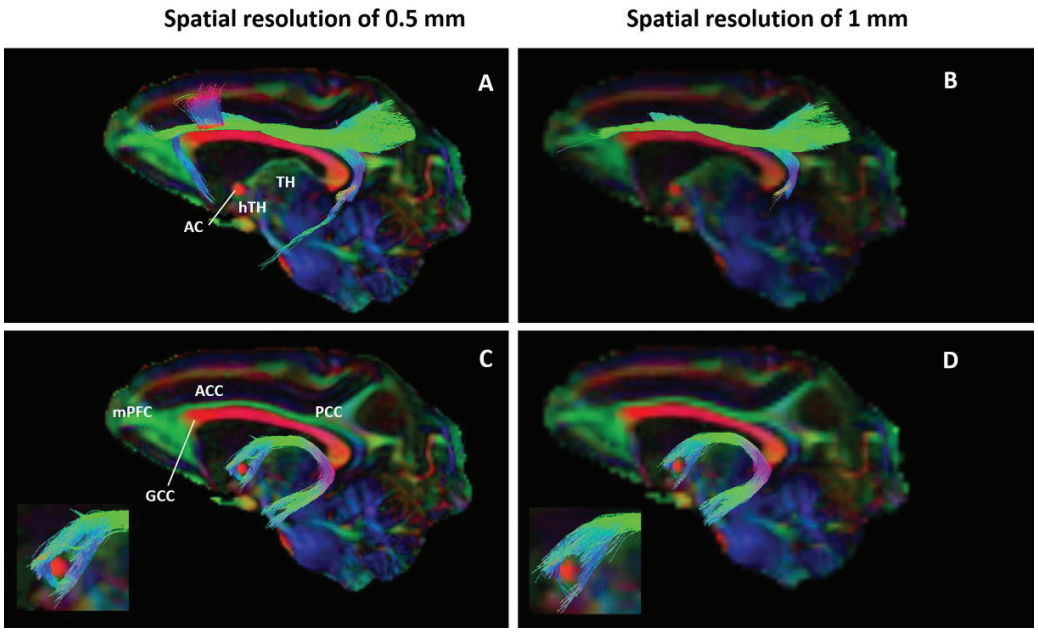

Figure IV.14: Comparison of tractography reconstruction results of the Cingulum Bundle (CB)(A and B) and the Fornix bundles (FX) (C and D) performed using dMRI data at resolution of 0.5 mm (left column) and subsampled data with 1 mm voxel size (right column).

The FX bundle revealed by tractography is located below the Corpus Callosum and arches around the thalamus (TH) (Fig. IV.14.C and IV.14.D). Anteriorly, it branches into two distinct tracks around the Anterior Commissure (AC). The most posterior of these two branches connects to the Mammillary Bodies (MB) on the medial temporal lobe and to the hypothalamus (hTH).

Posteriorly, the fornix arches down towards the hippocampus (HP) forming the fimbriae of the fornix. These CB and FX tracts are in accordance with the Calabrese's Atlas and the Zakszewski's Atlas performed using ex-vivo MRI data of macaque brain (Calabrese et al., 2015; Zakszewski et al., 2014).

Figures IV.14.A and IV.14.C show that, in comparison with the tractography results obtained from dMRI data with a spatial resolution of 1 mm (Fig.IV.14.B and IV.14.D), the use of 0.5 mm dMRI data for the tractography of cingulum bundles provides a better course on the parahyppocampal gyrus region and a good anterior arch. The added value of high-resolution DTI onto FX bundle

tractography is more subtle, though not negligible (see zoomed box of the Fig.IV.14). Indeed, a better segregation of the anterior branching of the FX can be identified. Posteriorly, a possible segregation between the FX branch ending up in the hippocampus and a more anterior branch ending up in the amygdala can be noted.

Discussion

I.11. High quality/resolution dMRI feasibility

High-resolution dMRI is very challenging due to the low sensitivity of the acquisition and to the large matrix size required to be collected in the Fourier–space. In this study, an acquisition method based on a 3D-EPI sampling of the Fourier-space was implemented and optimized on a 3T clinical scanner in order to achieve *in-vivo* dMRI of the macaque brain with a submillimetric resolution. The EPI sampling of Fourier-space was set to a multi-shot fashion in order to shorten the Fourier-space traversals, the echo time and the echo train length, and then to achieve a low-distortion dMRI.

This study demonstrates the achievability of high spatial resolution dMRI, up to 0.5 mm, on anesthetized and intubated macaque monkeys (Fig.IV.6 and Fig.IV.7). To our knowledge, such a resolution is the highest ever achieved on *in-vivo* macaque brain. In terms of voxel size, the voxel size reached in this study (0.125 mm^3, 2h acquisitions, surface coils) is 2.7 time smaller than that achieved by Janssens et al (0.343 mm^3) in 3h of acquisition time and using a 8-channel phased array coil whose loops were invasively implanted onto the skull of a macaque monkey (Janssens et al., 2012).

In term of angular resolution of dMRI data, the 3D-msEPI approach used to obtain a spatial resolution of 0.5 mm without any imaging acceleration strategy, provide a low angular resolution compared to that illustrated by Janssens et al. (~15 brain DW-images/h in this study against ~86 brain DW-images/h for Janssens approach). With an MR coil appropriated to achieve dMRI data using parallel imaging, 3D-EPI used in a single shot mode with parallel imaging is expected to achieve a similar angular resolution by hour as the 2D-ssEPI dMRI approach.

For example, dMRI data with 256 diffusion directions could be achieved non-invasively at a spatial resolution of 0.7 mm in 3h20 min using a 3D-ssEPI dMRI sequence and a parallel imaging factor of 2. So this is slightly slower than what is reported by Janssens et al., with however a major difference in overall SNR.

Thanks to the intrinsically high sensitivity of 3D-msEPI, high-resolution DW-images were obtained in this study with a high SNR (Table IV.4), a parameter that is crucial to compute accurately the water diffusion metrics maps (Qin et al., 2009) and to reduce the bias due to the non-Gaussian noise distribution (Basser et al., 1994). The water diffusion parameters measured in the white and grey matters of *in-vivo* macaque brains from DW-images with a cubic spatial resolution of 0.5 mm are compatible with those reported in the literature (Hofer et al., 2008; Liu et al., 2009; Shi et al., 2013). One can note that relatively high FA values were measured in the cerebral white matter (Table IV.5). This could be due to the low partial volume effects in the high-resolution DW-images. In the same manner, this study reveals anisotropy values of water diffusivity in the grey matter (Table IV.5 and figure IV.12), very close to what has already been reported in some *in-vivo* and *ex-vivo* studies (McNab et al., 2013; Reveley et al., 2015).

I.12. Comparison between 2D-ssEPI, 2D-msEPI and 3D-msEPI based dMRI pulse sequences

The comparison between 2D-ssEPI, 2D-msEPI and 3D-msEPI based dMRI pulse sequences showed that 1) the 2D-msEPI is more appropriate than 2D-ssEPI to perform high-resolution dMRI data in the anesthetized macaque due to its higher SNR efficiency and its robustness against the EPI-related artifacts such as susceptibility-induced geometric distortions (Fig.IV.4). This result is in line with previous studies performed in human (Atkinson et al., 2000; Butts et al., 1996; Golay et al., 2002). Additionally, msEPI is less sensitive to eddy currents effects than the ssEPI (Butts et al., 1997). 2) The 3D-msEPI offers a further significant SNR improvement compared to the 2D-msEPI method (Fig.IV.4). As quantitatively illustrated in Figure IV.5 and summarized in Table IV.5 and Table IV.6, the SNR increase obtained with the 3D-msEPI depends on the type of cerebral tissue considered (~3 in grey matter and ~4 in white matter). These results are in agreement with those recently reported in human studies (Chang et al., 2015b; Golay et al., 2002).

The difference in SNR measured between 3D-msEPI and 2D-msEPI data sets is mainly due to the high SNR efficiency of the 3D sampling of Fourier–space but could also be impacted by the imperfection of the 2D slice selectivity of the radiofrequency pulses used for 2D-EPI. These imperfections induce more pronounced deviations in the effective slice profile from the ideal rectilinear shape. These effects tend to be worse for the thinner slices required to achieve isotropic high-resolution dMRI data (Zhao et al., 2005).

Parallel imaging, not employed in this study, is expected to allow a significant decrease of TE and ETL of ssEPI and msEPI dMRI pulse sequences, and could thus enhance the quality of achievable data particularly for the ssEPI-dMRI pulse sequence

I.13. Limitation of 3D-msEPI based dMRI pulse sequence

In this study, an acquisition duration of 2h10min was required to collect 30 b1000 and 2 b0 images with high SNR using a whole brain 3D dMRI pulse sequence. Even if this long acquisition duration remains compatible with the experimental conditions on anesthetized monkeys, it could present a limitation to encode a higher number of diffusion directions in space and/or to perform multi-shell dMRI data. Various strategies could be employed to reduce the acquisition duration of whole brain 3D-msEPI-based dMRI. First, parallel imaging techniques allow to considerably reduce the acquisition time and to minimize geometric distortions (Griswold et al., 2002; Pruessmann et al., 1999). Parallel-imaging requires a phased-array coil with an appropriated geometry. Such a coil, more sensitive than the loop coils used here, could partially compensate the SNR decrease induced by acquisition acceleration (Janssens et al., 2012).

The multislab method has also been used in order to reduce the acquisition duration of 3D-EPI-based dMRI (Bruce et al., 2017; Engström and Skare, 2013; Wu et al., 2016b). However, the main challenge of the 3D-multislab approach is the signal mitigation between adjacent slabs also known as the slab boundary artifact. Numerous approaches have been proposed to overcome the slab boundary artifacts including oversampling the acquisition in the slice direction and using an optimized RF excitation pulse profile with an optimal TR (Engström et al., 2015). Moreover, data post-processing correction strategies were introduced in order to achieve high-resolution 3D

multislab dMRI data of the human brain free of slab boundary artifacts (Engström et al., 2015; Van et al., 2015; Wu et al., 2016a).

Another drawback for dMRI using 3D-msEPI is the inter-shot variation of MR signal phase, induced by the random rigid-body motion of the head and by the bulk motion caused by cerebrospinal fluid flow across the cardiac cycle. This shot-to-shot nonlinear phase inconsistencies, which typically causes ghosting artifacts in the generated images, would be amplified by the diffusion-sensitizing gradients when 3D-msEPI is used to collect dMRI data (Miller and Pauly, 2003).

Several reports have described 1D or 2D echo navigator based approaches aiming to estimate and reduce motion-induced phase inconsistencies of 2D-msEPI (Butts et al., 1996; Jeong et al., 2013; Liu et al., 2016; Ordidge et al., 1994; Porter and Heidemann, 2009). More recently, the feasibility of ghosting-free dMRI of human brain using 2D-navigated 3D-msEPI pulse sequence has been demonstrated (Chang et al., 2015b; Wu et al., 2016b).

The 2D-Navigator echoes were used to measure inter-shot phase variations and to perform a suitable phase correction of 3D-msEPI DW-data. However, the efficiency of this approach is valid only for the relatively thin slab (e.g. <30 mm) with the assumption that phase variations are negligible in the slice encoding direction (Engström and Skare, 2013). Chang et al. have recently described that motion-induced phase inconsistencies along the k_z component could be estimated and corrected using 3D-navigator echoes in order to achieve near whole brain dMRI data using single slab of 100 mm (Chang et al., 2017)

McNab et al. have combined a cardiac triggered 3D radial sampling of the Fourier-space with a batched internal navigator echoes approach to overcome the ghosting artifacts due to shot-to-shot nonlinear phase inconsistencies (McNab et al., 2010). Finally, readout-segmented EPI, which can be compatible with the 3D approach, has been also shown to be robust against ghosting artifacts (Frost et al., 2014). In this study, the head of the monkey was carefully fixed during the acquisition, as described above in the protocol setup section, to avoid the rigid-body motion of the head. However, the visual quality control shows that near 8% of DW-images were corrupted by ghosting artifacts, probably because of phase inconsistencies induced by physiological motions.

In this study, the objective of which was to prove the feasibility of very high-resolution dMRI in anesthetized macaque brain, DW-images corrupted by ghosting artifacts were simply removed from dMRI data sets before applying the post-processing pipeline. This lead to a reduction of the angular resolution of dMRI data and thus a reduction of the quality of diffusion tensor reconstructions. More subtle phase inconsistencies, induced by physiological motion, present in the remaining images though undetectable by eye inspection, could affect the quality of diffusion tensor maps by overestimating the diffusivity in brain regions where cardiac pulsatility is important as in brainstem and medial part of cerebellum (Nunes et al., 2005; Pierpaoli, 2010; Skare and Andersson, 2001). This will need to be quantified in future work.

An appropriate approach, based on navigator echoes and aiming to address the sensitivity of the proposed dMRI pulse sequence to ghosting artefacts, is under development in order to obtain completely ghosting-free high-resolution dMRI data in the macaque brain.

I.14. Added value of high resolution dMRI

This study highlights the potential of very high-resolution dMRI to precisely capture the microstructure of thin cerebral structures such as the hippocampus and superficial white matter. At a spatial resolution of 0.5 mm, some internal substructures of the hippocampus, such as the SuBiculum , the Pre-Subiculum, the Cornu Ammonis and the Dentrate Gyrus , start to be distinguishable and analyzable (Fig.IV.10). An acquisition zoomed on the hippocampus with adapted anisotropic voxel size could further enhance the capability of high-resolution dMRI to reveal more internal substructures of the hippocampus.

The resolution of 0.5 mm seems also to be beneficial to resolve and analyze the cortical GM/WM interface (Fig.IV.11). The superficial-WM structure has been considered as an ultimate limitation of tractography because it prevents reconstructed streamlines from penetrating from the deep-WM into the cortex-GM. *Ex-vivo* dMRI data acquired with high spatial resolution (250 μm) were used to demonstrate this limitation of tractography (Reveley et al., 2015). However, water diffusivity and core physiological properties of GM, superficial-WM and deep-WM change due to the brain fixation process. These changes could affect the FODs quality and influence tractography results. Therefore, the achievement of high-resolution dMRI *in-vivo* could open the door to study tractography limitation directly in alive tissues and independently of the brain fixation effects.

High-resolution Multi-shell dMRI could enhances the quality of the FODs and could be a promising issue to resolve the fibers crossing in superficial WM, and then to enhance tractography results.

High resolution FODs allow to discriminate the SLF, CST and CC tracts (Fig.IV.8). However, the quality of the CST tract is limited. Indeed, a part of the CST doesn't travel the three crossing region of the Centrum Semiovale to go into the motor areas of the cortex (precentral cortex). This is probably due to the low angular resolution, and the low volume fraction of the CST, compared to the volume fraction of the CC and SLF. This problem has been described in the literature and a solution have been proposed by Rheault et al. (Rheault et al., 2018). In agreement with this study, other recent reports point out the benefit of high-resolution dMRI to characterize small anatomical structure of brain (Steele et al., 2016). This is not only helpful to understand brain anatomy and connectivity, but could also lead to define new enhanced prognostic biomarkers of pathological, pharmacological or physiological conditions (Planche et al., 2017).

Conclusion

With an isotropic spatial resolution of 0.5 mm and a scan time of about 2 hours, the 3D-msEPI based dMRI acquisition method proposed in this study represents a significant achievement with respect to the state of the art of dMRI on anesthetized monkeys at 3T. This study highlights the potential of *in-vivo* very high-resolution dMRI to precisely capture the microstructure of thin cerebral structures such as the hippocampus and superficial white matter. Additional methodological developments are required to reduce the sensitivity of the proposed dMRI pulse sequence to ghosting artifacts and to reduce the acquisition duration. This would be a major methodological step towards a more systematic use of the 3D multi-shot EPI in human clinical research, thus demonstrating the tight link between preclinical and clinical applications.

Conclusion

This thesis is part of a larger project conducted by MR methodologists and neuroscientists which aims to better understand brain function and connectivity. The project also aims to increase the diagnostic and prognostic capacities of dMRI.

The developed approach is based on 3D encoding of k-space in order to improve the inherently low sensitivity of the dMRI acquisition. This allows significant enhancement of the overall SNR of the obtained images and increase in the spatial resolution in slice direction without being impacted by the imperfection of the 2D slice selectivity of the radiofrequency pulses used for 2D sampling of k-space. In addition, the k-space sampling was conducted using msEPI scheme to increase the in-plane resolution as well as to reduce the EPI-related artifacts such as off-resonance, image distortions, and blurring. The MR pulse sequence was developed and implemented on a 3T MR scanner (Prisma, Siemens) to perform high-sensitivity and high-resolution dMRI on the *in-vivo* human and non-human primate brains.

In-vitro acquisitions were first performed on a homemade diffusion phantom in order to set the acquisition parameters. Then additional *in-vivo* acquisitions were carried out to further optimize the experimental protocol and validate the pulse sequence.

Moreover, we have demonstrated the effectiveness and the added value of the proposed acquisition method at such resolution compared to the typically used pulse sequences. This study has shown that the classic 2D-ssEPI is not appropriate for performing high-resolution dMRI data because of high level distortions, signal loss, and susceptibility artifacts. Furthermore, we illustrated that 3D-msEPI provides a significant SNR improvement in comparison with the 2D-msEPI pulse sequence. An SNR gain of 3 was quantified for cerebral grey matter and of 4.7 for white matter.

Thanks to the developed approach, we were able to non-invasively achieve dMRI data of the macaque monkey brain at 3T with an isotropic spatial resolution of 0.5 mm. This is the highest spatial resolution ever achieved non-invasively on the *in-vivo* macaque brain.

This study has also illustrated the benefits of very high spatial resolution dMRI data (cubic 0.5 mm) to visualize and analyze *in-vivo* fine structures of the macaque brain not detectable with the classical acquisition resolution (cubic 1mm), such as the subfields of the hippocampus and superficial white matter. High-resolution dMRI was also shown to be useful for detecting with more precision the orientation and the trajectories of white matter bundles.

The prelaminar dMRI acquisitions conducted in humans using the 3D-msEPI dMRI pulse sequence provided very encouraging results. DW-images with an isotropic spatial resolution of 0.8 mm, with high SNR as well as low image artifacts were achieved using the proposed pulse sequence.

Finally, the 3D-ssEPI approach was combined with the parallel imaging technique in order to reduce the acquisition duration of dMRI and was used to collect dMRI data on human and macaque brains.

To emphasize the contributions of the thesis, we can summarize these achievements in the following points:

<u>Methodological developments</u>

- Development of 3D-msEPI and 3D-ssEPI dMRI pulse sequences using Siemens IDEA VD13D and VE11C software. Then, the pulse sequences was implemented on a 3T MR scanner Magnetom Prisma system (Siemens Healthineers, Erlangen, Germany).
- The SIEMENS data reconstructor software (ICE) was not adopted for the reconstruction of data acquired using 3D-EPI pulse sequence. Therefore, in collaboration with Yann Bihan-Poudec (a PhD student in our group from 2016/2019), we have used Gadgetron software (Hansen and Sørensen, 2013) to reconstruct 3D dMRI data. Yann Bihan-Poudec has also set up all the data post processing and tractography pipelines and adapted it for the high-resolution images.
- The parallel imaging technique (GRAPPA) was implemented along the phase and slice/partition encoding directions.

<u>Validation and optimization</u>

- *In-vitro* and *in-vivo* optimization of the acquisition parameters (e.g., TR, TE, RF pulse, Bandwidth, and EPI segments) for macaque and human acquisition.
- Optimization of the experimental protocol setup: substitution of the custom-built 8-channel coil with a local transmission coil by a vendor three loop surface receiver coils with whole body coil transmission to improve the B_1 field homogeneity. In addition, isoflurane anesthesia was used instead intramuscular injection of ketamine.

Results

- Performing dMRI data on 4 anesthetized macaque brains with an isotropic spatial resolution of 0.5 mm in an acceptable scan time or preclinical conditions.
- Performing dMRI data on the human brain with an isotropic spatial resolution up to 0.8 mm.

Basically, the 3D-msEPI pulse sequence was developed to reach much higher spatial resolution with high SNR and reduced artifacts dMRI data. However, it requires a long scan time and it is very sensitive to subject motion. Whereas, the 3D-ssEPI pulse sequence combined with the parallel imaging allows achievement of high spatial resolution (e.g. 1 mm isotropic) with high SNR in a clinically acceptable scan time (e.g., 1 minute/ image).

Perspective

The inherently low sensitivity of dMRI acquisition is a crucial challenge to obtaining data with high resolution. For this reason, we have chosen a single slab mode for whole brain 3D-msEPI scheme imaging, resulting in long scan time of ~4 minutes per DW-image. This limits the feasible angular resolution, e.g., we were limited to 30 encoding directions in 2h. The parallel imaging techniques (SENSE and GRAPPA) are typically used in order to reduce the duration of the MR scan. With an appropriate MR phased arrays coil, the 3D-ssEPI can be used with parallel imaging and it is expected to achieve higher angular resolution similar in acceptable scan time.

On the other hand, dMRI acquisition suffers from its high sensitivity to subject motion specifically when it is conducted using the msEPI approach. Indeed, random bulk motion induces an inter-shot variation of MR signal phase, which typically causes ghosting artifacts. In this study, near 8% of DW-images were corrupted by ghosting artifacts, and were simply removed from dMRI data sets before applying the post-processing pipeline. To address this limitation, additional methodological developments are underway to combine the proposed methods (3D- msEPI and ssEPI) with the 2D/3D navigator echo approach (Liu et al., 2016; Ordidge et al., 1994; Porter and Heidemann, 2009).

References

Albert Einstein, 1905. On the movement of small particles suspended in stationary liquids required by the molecular-kinetic theory of heat. Ann. der Phys. 17 V, 549–560. doi:10.1002/andp.19053220806

Andersson, J.L.R., Skare, S., Ashburner, J., 2003. How to correct susceptibility distortions in spin-echo echo-planar images: Application to diffusion tensor imaging. Neuroimage 20, 870–888. doi:10.1016/S1053-8119(03)00336-7

Andersson, J.L.R., Sotiropoulos, S.N., 2016. An integrated approach to correction for off-resonance effects and subject movement in diffusion MR imaging. Neuroimage 125, 1063–1078. doi:10.1016/j.neuroimage.2015.10.019

Atkinson, D., Porter, D.A., Hill, D.L.G., Calamante, F., Connelly, A., 2000. Sampling and Reconstruction Effects Due to Motion in Diffusion-Weighted Interleaved Echo Planar Imaging. Magn. Reson. Med. 44, 101–109.

Bammer, R., Keeling, S.L., Augustin, M., Pruessmann, K.P., Wolf, R., Stollberger, R., Hartung, H.P., Fazekas, F., 2001. Improved diffusion-weighted single-shot echo-planar imaging (EPI) in stroke using sensitivity encoding (SENSE). Magn. Reson. Med. 46, 548–54.

Bammer, R., Stollberger, R., Augustin, M., Simbrunner, J., Offenbacher, H., Kooijman, H., Ropele, S., Kapeller, P., Wach, P., Ebner, F., Fazekas, F., 1999. Diffusion-weighted imaging with navigated interleaved echo-planar imaging and a conventional gradient system. Radiology 211, 799–806. doi:10.1148/radiology.211.3.r99jn15799

Basser, P.J., Mattiello, J., LeBihan, D., 1994. MR diffusion tensor spectroscopy and imaging. Biophys. J. 66, 259–267. doi:10.1016/S0006-3495(94)80775-1

Basser, P.J., Pajevic, S., Pierpaoli, C., Duda, J., Aldroubi, A., 2000. In vivo fiber tractography using DT-MRI data. Magn. Reson. Med. 44, 625–32.

Basser, P.J., Pierpaoli, C., 1998. A simplified method to measure the diffusion tensor from seven MR images. Magn Reson Med 39, 928–934. doi:10.1002/mrm.1910390610

Bilgic, B., Ye, H., Wald, L.L., Setsompop, K., 2017. Simultaneous Time Interleaved MultiSlice (STIMS) for Rapid Susceptibility Weighted acquisition. Neuroimage 1–10. doi:10.1016/j.neuroimage.2017.04.036

Brown, R., 1828. XXVII. A brief account of microscopical observations made in the months of June, July and August 1827, on the particles contained in the pollen of plants; and on the general existence of active molecules in organic and inorganic bodies. Philos. Mag. 4, 161–173. doi:10.1080/14786442808674769

Bruce, I.P., Chang, H.-C., Petty, C., Chen, N.-K., Song, A.W., 2017. 3D-MB-MUSE: A robust 3D multi-slab, multi-band and multi-shot reconstruction approach for ultrahigh resolution diffusion MRI. Neuroimage 159, 46–56. doi:10.1016/j.neuroimage.2017.07.035

Bruder, H., Fischer, H., Schmitt, F., 1992. Image Reconstruction for Echo Planar Imaging with Nonequidistant k-Space Sampling. Magn. Reson. Med. 23, 311–323. doi:10.1002/mrm.1910230211

Butts, K., Crespigny, A. De, Pauly, J.M., Moseley, M., 1996. Diffusion-Weighted interleaved Echo-Planar Imaging with a Pair of Orthogonal Navigator Echoes. Magn. Reson. Imaging 35, 763–770. doi:10.1002/mrm.1910350518

Butts, K., Pauly, J., De Crespigny, A., Moseley, M., 1997. Isotropic diffusion-weighted and spiral-navigated interleaved EPI for routine imaging of acute stroke. Magn. Reson. Med. 38, 741–749. doi:10.1002/mrm.1910380510

Calabrese, E., Badea, A., Coe, C.L., Lubach, G.R., Shi, Y., Styner, M.A., Johnson, G.A., 2015. A diffusion tensor MRI atlas of the postmortem rhesus macaque brain. Neuroimage 117, 408–416. doi:10.1016/j.neuroimage.2015.05.072

Caruyer, E., Lenglet, C., Sapiro, G., Deriche, R., 2013. Design of multishell sampling schemes with uniform coverage in diffusion MRI. Magn. Reson. Med. 69, 1534–1540. doi:10.1002/mrm.24736

Chang, H.C., Guhaniyogi, S., Chen, N.K., 2015a. Interleaved diffusion-weighted improved by adaptive partial-Fourier and multiband multiplexed sensitivity-encoding reconstruction. Magn. Reson. Med. 73, 1872–1884. doi:10.1002/mrm.25318

Chang, H.C., Hui, E.S., Chiu, P.W., Liu, X., Chen, N. kuei, 2017. Phase correction for three-dimensional (3D) diffusion-weighted interleaved EPI using 3D multiplexed sensitivity encoding and reconstruction (3D-MUSER). Magn. Reson. Med. 0, 33–35. doi:10.1002/mrm.26944

Chang, H.C., Sundman, M., Petit, L., Guhaniyogi, S., Chu, M.L., Petty, C., Song, A.W., Chen, N. kuei, 2015b. Human brain diffusion tensor imaging at submillimeter isotropic resolution on a 3Tesla clinical MRI scanner. Neuroimage 118, 667–675. doi:10.1016/j.neuroimage.2015.06.016

Chen, N. kuei, Guidon, A., Chang, H.C., Song, A.W., 2013. A robust multi-shot scan strategy for high-resolution diffusion weighted MRI enabled by multiplexed sensitivity-encoding (MUSE). Neuroimage 72, 41–47. doi:10.1016/j.neuroimage.2013.01.038

D'Arceuil, H., de Crespigny, A., 2007. The effects of brain tissue decomposition on diffusion tensor imaging and tractography. Neuroimage 36, 64–68. doi:10.1016/j.neuroimage.2007.02.039

DeFelipe, J., 2011. The Evolution of the Brain, the Human Nature of Cortical Circuits, and Intellectual Creativity. Front. Neuroanat. 5, 1–17. doi:10.3389/fnana.2011.00029

Descoteaux, M., 2008. High Angular Resolution Diffusion MRI : from Local Estimation to Segmentation and Tractography. PhD Thesis 313.

Descoteaux, M., Angelino, E., Fitzgibbons, S., Deriche, R., 2007. Regularized, fast, and robust analytical Q-ball imaging. Magn. Reson. Med. 58, 497–510. doi:10.1002/mrm.21277

Dietrich, O., Raya, J.G., Reeder, S.B., Reiser, M.F., Schoenberg, S.O., 2007. Measurement of signal-to-noise ratios in MR images: Influence of multichannel coils, parallel imaging, and reconstruction filters. J. Magn. Reson. Imaging 26, 375–385. doi:10.1002/jmri.20969

Douaud, G., Jbabdi, S., Behrens, T.E.J., Menke, R.A., Gass, A., Monsch, A.U., Rao, A., Whitcher, B., Kindlmann, G., Matthews, P.M., Smith, S., 2011. DTI measures in crossing-fibre areas: Increased diffusion anisotropy reveals early white matter alteration in MCI and mild Alzheimer's disease. Neuroimage 55, 880–890. doi:10.1016/j.neuroimage.2010.12.008

Engström, M., Martensson, M., Avventi, E., Skare, S., 2015. On the signal-to-noise ratio efficiency

and slab-banding artifacts in three-dimensional multislab diffusion-weighted echo-planar imaging. Magn. Reson. Med. 73, 718–725. doi:10.1002/mrm.25182

Engström, M., Skare, S., 2013. Diffusion-weighted 3D multislab echo planar imaging for high signal-to-noise ratio efficiency and isotropic image resolution. Magn. Reson. Med. 70, 1507–1514. doi:10.1002/mrm.24594

Fan, Q., Nummenmaa, A., Polimeni, J.R., Witzel, T., Huang, S.Y., Wedeen, V.J., Rosen, B.R., Wald, L.L., 2017. HIgh b-value and high Resolution Integrated Diffusion (HIBRID) imaging. Neuroimage 150, 162–176. doi:10.1016/j.neuroimage.2017.02.002

Feng, L., Jeon, T., Yu, Q., Ouyang, M., Peng, Q., Mishra, V., Pletikos, M., Sestan, N., Miller, M.I., Mori, S., Hsiao, S., Liu, S., Huang, H., 2017. Population-averaged macaque brain atlas with high-resolution ex vivo DTI integrated into in vivo space. Brain Struct. Funct. 222, 4131–4147. doi:10.1007/s00429-017-1463-6

Fortin, D., Aubin-Lemay, C., Boré, A., Girard, G., Houde, J.-C., Whittingstall, K., Descoteaux, M., 2012. Tractography in the study of the human brain: a neurosurgical perspective. Can. J. Neurol. Sci. 39, 747–56. doi:10.1017/S0317167100015560

Frahm, J., Haase, A., Matthaei, D., 1986. Rapid NMR imaging of dynamic processes using the FLASII technique. Magn. Reson. Med. 3, 321–327. doi:10.1002/mrm.1910030217

Frost, R., Jezzard, P., Clare, S., Porter, D.A., Miller, K.L., 2015. Scan Time Reduction for Readout-Segmented EPI Using Simultaneous Multislice Acceleration : Diffusion-Weighted Imaging at 3 and 7 Tesla 149, 136–149. doi:10.1002/mrm.25391

Frost, R., Miller, K.L., Tijssen, R.H.N., Porter, D.A., Jezzard, P., 2014. 3D multi-slab diffusion-weighted readout-segmented EPI with real-time cardiac-reordered k-space acquisition. Magn. Reson. Med. 72, 1565–1579. doi:10.1002/mrm.25062

Golay, X., Jiang, H., van Zijl, P.C.M., Mori, S., 2002. High-resolution isotropic 3D diffusion tensor imaging of the human brain. Magn. Reson. Med. 47, 837–843. doi:10.1002/mrm.10143

Gold, G.E., Han, E., Stainsby, J., Wright, G., Brittain, J., Beaulieu, C., 2004. Musculoskeletal MRI at 3.0 T: Relaxation Times and Image Contrast. Am. J. Roentgenol. 183, 343–351. doi:10.2214/ajr.183.2.1830343

Griswold, M.A., Jakob, P.M., Heidemann, R.M., Nittka, M., Jellus, V., Wang, J., Kiefer, B., Haase, A., 2002. Generalized Autocalibrating Partially Parallel Acquisitions (GRAPPA). Magn. Reson. Med. 47, 1202–1210. doi:10.1002/mrm.10171

Hansen, M.S., Sørensen, T.S., 2013. Gadgetron: An open source framework for medical image reconstruction. Magn. Reson. Med. 69, 1768–1776. doi:10.1002/mrm.24389

Hauger, O., Dumont, E., Chateil, J.-F., Moinard, M., Diard, F., 2002. Water excitation as an alternative to fat saturation in MR imaging: preliminary results in musculoskeletal imaging. Radiology 224, 657–663. doi:10.1148/radiol.2243011227

Hennig, J., 1988. Multiecho imaging sequences with low refocusing flip angles. J. Magn. Reson. 78, 397–407. doi:10.1016/0022-2364(88)90128-X

Hennig, J., Nauerth, A., Friedburg, H., 1986. RARE imaging: a fast imaging method for clinical MR. Magn. Reson. Med. 3, 823–33.

Hofer, S., Merboldt, K.D., Tammer, R., Frahm, J., 2008. Rhesus monkey and human share a similar topography of the corpus callosum as revealed by diffusion tensor mri in vivo. Cereb. Cortex 18, 1079–1084. doi:10.1093/cercor/bhm141

Holdsworth, S.J., Skare, S., Newbould, R.D., Guzmann, R., Blevins, N.H., Bammer, R., 2008. Readout-segmented EPI for rapid high resolution diffusion imaging at 3T. Eur. J. Radiol. 65, 36–46. doi:10.1016/j.ejrad.2007.09.016

Hutchison, R.M., Culham, J.C., Flanagan, J.R., Everling, S., Gallivan, J.P., 2015. Functional subdivisions of medial parieto-occipital cortex in humans and nonhuman primates using resting-state fMRI. Neuroimage 116, 10–29. doi:10.1016/j.neuroimage.2015.04.068

Jaermann, T., Pruessmann, K.P., Valavanis, A., Kollias, S., Boesiger, P., 2006. Influence of SENSE on image properties in high-resolution single-shot echo-planar DTI. Magn. Reson. Med. 55, 335–342. doi:10.1002/mrm.20769

Jakob, P.M., Grisowld, M.A., Edelman, R.R., Sodickson, D.K., 1998. AUTO-SMASH: A self-calibrating technique for SMASH imaging. Magma Magn. Reson. Mater. Physics, Biol. Med. 7, 42–54. doi:10.1007/BF02592256

Janssens, T., Keil, B., Farivar, R., McNab, J.A., Polimeni, J.R., Gerits, A., Arsenault, J.T., Wald, L.L., Vanduffel, W., 2012. An implanted 8-channel array coil for high-resolution macaque MRI at 3T. Neuroimage 62, 1529–1536. doi:10.1016/j.neuroimage.2012.05.028

Jeong, H., Gore, J.C., Anderson, A.W., 2013. High-Resolution Human Diffusion Tensor Imaging Using 2-D Navigated Multishot SENSE EPI at 7 T 802, 793–802. doi:10.1002/mrm.24320

Jezzard, P., Balaban, R.S., 1995. Correction for Geometric Distortion in Echo-Planar Images from B0 Field Variations. Magn. Reson. Med. 34, 65–73.

Kellman, P., McVeigh, E.R., 2005. Image reconstruction in SNR units: A general method for SNR measurement. Magn. Reson. Med. 54, 1439–1447. doi:10.1002/mrm.20713

Khachaturian, M.H., 2010. A 4-channel 3 Tesla phased array receive coil for awake rhesus monkey fMRI and diffusion MRI experiments. J. Biomed. Sci. Eng. 3, 1085–1092. doi:10.4236/jbise.2010.311141

Kimme, P., Ledin, T., Sjöberg, F., 2007. Dose effect of sevoflurane and isoflurane anesthetics on cortical blood flow during controlled hypotension in the pig. Acta Anaesthesiol. Scand. 51, 607–613. doi:10.1111/j.1399-6576.2007.01281.x

Kolster, H., Janssens, T., Orban, G.A., Vanduffel, W., 2014. The retinotopic organization of macaque occipitotemporal cortex anterior to V4 and caudoventral to the middle temporal (MT) cluster. J. Neurosci. 34, 10168–91. doi:10.1523/JNEUROSCI.3288-13.2014

Konomi, T., Fujiyoshi, K., Hikishima, K., Komaki, Y., Tsuji, O., Okano, H.J., Toyama, Y., Okano, H., Nakamura, M., 2012. Conditions for quantitative evaluation of injured spinal cord by in vivo diffusion tensor imaging and tractography: Preclinical longitudinal study in common marmosets. Neuroimage 63, 1841–1853. doi:10.1016/j.neuroimage.2012.08.040

Lavdas, I., Behan, K.C., Papadaki, A., McRobbie, D.W., Aboagye, E.O., 2013. A phantom for diffusion-weighted MRI (DW-MRI). J. Magn. Reson. Imaging 38, 173–179. doi:10.1002/jmri.23950

Le Bihan, D., 1988. Intravoxel incoherent motion imaging using steady-state free precession. Magn. Reson. Med. 7, 346–351. doi:10.1002/mrm.1910070312

Le Bihan, D., Breton, E., Lallemand, D., Grenier, P., Cabanis, E., Laval-Jeantet, M., 1986. MR imaging of intravoxel incoherent motions: application to diffusion and perfusion in neurologic disorders. Radiology 161, 401–407. doi:10.1148/radiology.161.2.3763909

Le Bihan, D., Johansen-Berg, H., 2012. Diffusion MRI at 25: Exploring brain tissue structure and function. Neuroimage 61, 324–341. doi:10.1016/j.neuroimage.2011.11.006

Li, C.X., Patel, S., Auerbach, E.J., Zhang, X., 2013. Dose-dependent effect of isoflurane on regional cerebral blood flow in anesthetized macaque monkeys. Neurosci. Lett. 541, 58–62. doi:10.1016/j.neulet.2013.02.007

Li, Z., Pipe, J.G., Lee, C.Y., Debbins, J.P., Karis, J.P., Huo, D., 2011. X-PROP: A fast and robust diffusion-weighted propeller technique. Magn. Reson. Med. 66, 341–347. doi:10.1002/mrm.23033

Liu, C., Bammer, R., Kim, D., Moseley, M.E., 2004. Self-navigated interleaved spiral (SNAILS): Application to high-resolution diffusion tensor imaging. Magn. Reson. Med. 52, 1388–1396. doi:10.1002/mrm.20288

Liu, W., Zhao, X., Ma, Y., Tang, X., Gao, J.H., 2016. DWI using navigated interleaved multishot EPI with realigned GRAPPA reconstruction. Magn. Reson. Med. 75, 280–286. doi:10.1002/mrm.25586

Liu, X., Zhu, T., Gu, T., Zhong, J., 2009. A practical approach to in vivo high-resolution diffusion tensor imaging of rhesus monkeys on a 3-T human scanner. Magn. Reson. Imaging 27, 335–346. doi:10.1016/j.mri.2008.07.004

Mansfield, P., 1977. Multi-planar image formation using NMR spin echoes. J. Phys. C Solid State Phys. 10, L55–L58. doi:10.1088/0022-3719/10/3/004

Masamoto, K., Fukuda, M., Vazquez, A., Kim, S.G., 2009. Dose-dependent effect of isoflurane on neurovascular coupling in rat cerebral cortex. Eur. J. Neurosci. 30, 242–250. doi:10.1111/j.1460-9568.2009.06812.x

McNab, J.A., Gallichan, D., Miller, K.L., 2010. 3D steady-state diffusion-weighted imaging with trajectory using radially batched internal navigator echoes (TURBINE). Magn. Reson. Med. 63, 235–242. doi:10.1002/mrm.22183

McNab, J.A., Miller, K.L., 2010. Steady-state diffusion-weighted imaging: Theory, acquisition and analysis. NMR Biomed. 23, 781–793. doi:10.1002/nbm.1509

McNab, J.A., Polimeni, J.R., Wang, R., Augustinack, J.C., Fujimoto, K., Stevens, A., Janssens, T., Farivar, R., Folkerth, R.D., Vanduffel, W., Wald, L.L., 2013. Surface based analysis of diffusion orientation for identifying architectonic domains in the in vivo human cortex. Neuroimage 69, 87–100. doi:10.1016/j.neuroimage.2012.11.065

Miller, K.L., Pauly, J.M., 2003. Nonlinear phase correction for navigated diffusion imaging. Magn. Reson. Med. 50, 343–353. doi:10.1002/mrm.10531

Mori, S., Crain, B.J., Chacko, V.P., van Zijl, P.C., 1999. Three-dimensional tracking of axonal projections in the brain by magnetic resonance imaging. Ann. Neurol. 45, 265–9. doi:10.1002/1531-8249(199902)45:2<265::AID-ANA21>3.0.CO;2-3

Moseley, M.E., Cohen, Y., Kucharczyk, J., Mintorovitch, J., Asgari, H.S., Wendland, M.F., Tsuruda, J., Norman, D., 1990a. Diffusion-weighted MR imaging of anisotropic water diffusion in cat central nervous system. Radiology 176, 439–445. doi:10.1148/radiology.176.2.2367658

Moseley, M.E., Cohen, Y., Mintorovitch, J., Chileuitt, L., Shimizu, H., Kucharczyk, J., Wendland, M.F., Weinstein, P.R., 1990b. Early detection of regional cerebral ischemia in cats: comparison of diffusion- and T2-weighted MRI and spectroscopy. Magn. Reson. Med. 14, 330–46.

Nunes, R.G., Jezzard, P., Clare, S., 2005. Investigations on the efficiency of cardiac-gated methods for the acquisition of diffusion-weighted images. J. Magn. Reson. 177, 102–110. doi:10.1016/j.jmr.2005.07.005

Oishi, K., Huang, H., Yoshioka, T., Ying, S.H., Zee, D.S., Zilles, K., Amunts, K., Woods, R., Toga, A.W., Pike, G.B., Rosa-Neto, P., Evans, A.C., van Zijl, P.C.M., Mazziotta, J.C., Mori, S., 2011. Superficially Located White Matter Structures Commonly Seen in the Human and the Macaque Brain with Diffusion Tensor Imaging. Brain Connect. 1, 37–47. doi:10.1089/brain.2011.0005

Ordidge, R.J., Helpern, J.A., Qing, Z.X., Knight, R.A., Nagesh, V., 1994. Correction of motional

artifacts in diffusion-weighted MR images using navigator echoes. Magn. Reson. Imaging 12, 455–460. doi:10.1016/0730-725X(94)92539-9

Oshima, T., Karasawa, F., Okazaki, Y., Wada, H., Satoh, T., 2003. Effects of sevoflurane on cerebral blood flow and cerebral metabolic rate of oxygen in human beings: a comparison with isoflurane. Eur. J. Anaesthesiol. doi:10.1097/00003643-200307000-00005

Pajevic, S., Pierpaoli, C., 2000. Color Schemes to Represent the Orientation of Anisotropic Tissues From Diffusion Tensor Data: Application To White MAtter Fiber Tract Mapping in the Human Brain, in: Magnetic Resonance in Medicine. p. 2000.

Pierpaoli, C., 2010. Artifacts in diffusion MRI. Diffus. MRI Theory, Methods Appl. … 303–318. doi:10.1093/med/9780195369779.003.0018

Pierpaoli, C., Basser, P.J., 1996. Toward a quantitative assessment of diffusion anisotropy. Magn. Reson. Med. 36, 893–906. doi:10.1002/mrm.1910360612

Pipe, J.G., Farthing, V.G., Forbes, K.P., 2002. Multishot diffusion-weighted FSE using PROPELLER MRI. Magn. Reson. Med. 47, 42–52. doi:10.1002/mrm.10014

Planche, V., Panatier, A., Hiba, B., Ducourneau, E.G., Raffard, G., Dubourdieu, N., Maitre, M., Lesté-Lasserre, T., Brochet, B., Dousset, V., Desmedt, A., Oliet, S.H., Tourdias, T., 2017. Selective dentate gyrus disruption causes memory impairment at the early stage of experimental multiple sclerosis. Brain. Behav. Immun. 60, 240–254. doi:10.1016/j.bbi.2016.11.010

Porter, D.A., Calamante, F., Gadian, D.G., Connelly, A., 1999. The Effect of Residual Nyquist Ghost in Quantitative Echo-Planar Diffusion Imaging 392, 385–392.

Porter, D.A., Heidemann, R.M., 2009. High resolution diffusion-weighted imaging using readout-segmented echo-planar imaging, parallel imaging and a two-dimensional navigator-based reacquisition. Magn. Reson. Med. 62, 468–475. doi:10.1002/mrm.22024

Pruessmann, K.P., Weiger, M., Scheidegger, M.B., Boesiger, P., 1999. SENSE: Sensitivity encoding for fast MRI. Magn. Reson. Med. 42, 952–962. doi:10.1002/(SICI)1522-2594(199911)42:5<952::AID-MRM16>3.0.CO;2-S

Qin, W., Yu, C.S., Zhang, F., Du, X.Y., Jiang, H., Yan, Y.X., Li, K.C., 2009. Effects of echo time on diffusion quantification of brain white matter at 1.5T and 3.0T. Magn. Reson. Med. 61, 755–760. doi:10.1002/mrm.21920

Reese, T.G., Heid, O., Weisskoff, R.M., Wedeen, V.J., 2003. Reduction of eddy-current-induced distortion in diffusion MRI using a twice-refocused spin echo. Magn. Reson. Med. 49, 177–182. doi:10.1002/mrm.10308

Reveley, C., Seth, A.K., Pierpaoli, C., Silva, A.C., Yu, D., Saunders, R.C., Leopold, D. a., Ye, F.Q., 2015. Superficial white matter fiber systems impede detection of long-range cortical connections in diffusion MR tractography. Proc. Natl. Acad. Sci. 201418198. doi:10.1073/pnas.1418198112

Rheault, F., St-onge, E., Sidhu, J., Chenot, Q., Petit, L., Descoteaux, M., 2018. Bundle-Specific Tractography. Sprinher Nat. 129–139.

Schaefer, D.J., Bourland, J.D., Nyenhuis, J.A., 2000. Review of patient safety in time-varying gradient fields. J. Magn. Reson. Imaging 12, 20–9.

Schilling, K., Gao, Y., Stepniewska, I., Choe, A.S., Landman, B.A., Anderson, A.W., 2017. Reproducibility and variation of diffusion measures in the squirrel monkey brain, in vivo and ex vivo. Magn. Reson. Imaging 35, 29–38. doi:10.1016/j.mri.2016.08.015

Schmahmann, J.D., Pandya, D.N., 2006. FIber Pathways of the Brain.

Schuff, N., Woerner, N., Boreta, L., Kornfield, T., Shaw, L.M., Trojanowski, J.Q., Thompson, P.M., Jack, C.R., Weiner, M.W., 2009. MRI of hippocampal volume loss in early Alzheimers disease in relation to ApoE genotype and biomarkers. Brain 132, 1067–1077. doi:10.1093/brain/awp007

Semendeferi, K., Lu, A., Schenker, N., Damasio, H., 2002. Humans and great apes share a large frontal cortex. Nat. Neurosci. 5, 272–276. doi:10.1038/nn814

Setsompop, K., Fan, Q., Stockmann, J., Bilgic, B., Huang, S., Cauley, S.F., Nummenmaa, A., Wang, F., Rathi, Y., Witzel, T., Wald, L.L., 2018. High-resolution in vivo diffusion imaging of the human brain with generalized slice dithered enhanced resolution: Simultaneous multislice (gSlider-SMS). Magn. Reson. Med. 79, 141–151. doi:10.1002/mrm.26653

Shi, Y., Short, S.J., Knickmeyer, R.C., Wang, J., Coe, C.L., Niethammer, M., Gilmore, J.H., Zhu, H., Styner, M.A., 2013. Diffusion tensor imaging-based characterization of brain neurodevelopment in primates. Cereb. Cortex 23, 36–48. doi:10.1093/cercor/bhr372

Skare, S., Andersson, J.L.R., 2001. On the effects of gating in diffusion imaging of the brain using single shot EPI. Magn. Reson. Imaging 19, 1125–1128. doi:10.1016/S0730-725X(01)00415-5

Steele, C.J., Anwander, A., Bazin, P., Trampel, R., Schaefer, A., Turner, R., Ramnani, N., Villringer, A., 2016. Human Cerebellar Sub-millimeter Diffusion Imaging Reveals the Motor and Non-motor Topography of the Dentate Nucleus 1–12. doi:10.1093/cercor/bhw258

Stejskal, E.O., Tanner, J.E., 1965. Spin diffusion measurements: Spin echoes in the presence of a time-dependent field gradient. J. Chem. Phys. 42, 288–292. doi:10.1063/1.1695690

Tounekti, S., Troalen, T., Bihan-Poudec, Y., Froesel, M., Lamberton, F., Ozenne, V., Cléry, J., Richard, N., Descoteaux, M., Ben Hamed, S., Hiba, B., 2018. High-resolution 3D diffusion tensor MRI of anesthetized rhesus macaque brain at 3T. Neuroimage 181, 149–161. doi:10.1016/J.NEUROIMAGE.2018.06.045

Tournier, J.-D., , F. Calamante, and a. C., 2010. Improved probabilistic streamlines tractography by 2 nd order integration over fibre orientation distributions. Ismrm 88, 2010.

Tournier, J.-D., Mori, S., Leemans, A., 2011. Diffusion tensor imaging and beyond. Magn. Reson. Med. 65, 1532–1556. doi:10.1002/mrm.22924

Tournier, J., Calamante, F., Connelly, A., 2012. MRtrix : Diffusion Tractography in Crossing Fiber Regions. doi:10.1002/ima.22005

Tournier, J.D., Calamante, F., Connelly, A., 2007. Robust determination of the fibre orientation distribution in diffusion MRI: Non-negativity constrained super-resolved spherical deconvolution. Neuroimage 35, 1459–1472. doi:10.1016/j.neuroimage.2007.02.016

Tournier, J.D., Calamante, F., Gadian, D.G., Connelly, A., 2004. Direct estimation of the fiber orientation density function from diffusion-weighted MRI data using spherical deconvolution. Neuroimage 23, 1176–1185. doi:10.1016/j.neuroimage.2004.07.037

Tuch, D.S., 2004. Q-ball imaging. Magn. Reson. Med. 52, 1358–1372. doi:10.1002/mrm.20279

Tustison, N.J., Avants, B.B., Cook, P.A., Zheng, Y., Egan, A., Yushkevich, P.A., Gee, J.C., 2010. N4ITK: Improved N3 bias correction. IEEE Trans. Med. Imaging 29, 1310–1320. doi:10.1109/TMI.2010.2046908

Van, A.T., Aksoy, M., Holdsworth, S.J., Kopeinigg, D., Vos, S.B., Bammer, R., 2015. Slab profile encoding (PEN) for minimizing slab boundary artifact in three-dimensional diffusion-weighted multislab acquisition. Magn. Reson. Med. 73, 605–613. doi:10.1002/mrm.25169

Wang, F., Huang, T., Lin, F., Chuang, T., Chen, N., Chung, H., Chen, C., Kwong, K.K., 2005. PROPELLER EPI : An MRI Technique Suitable for Diffusion Tensor Imaging at High Field Strength With Reduced Geometric Distortions 1240, 1232–1240. doi:10.1002/mrm.20677

Wang, H., 2012. Accelerating MRI Data Acquisition Using Parallel Imaging and Compressed Sensing.

Wansapura, J.P., Holland, S.K., Dunn, R.S., Ball, W.S., 1999. NMR relaxation times in the human brain at 3.0 tesla. J. Magn. Reson. Imaging 9, 531–8.

Westin, C.F., Maier, S.E., Mamata, H., Nabavi, A., Jolesz, F.A., Kikinis, R., 2002. Processing and visualization for diffusion tensor MRI. Med. Image Anal. 6, 93–108. doi:10.1016/S1361-8415(02)00053-1

Wey, H.-Y., Phillips, K.A., McKay, D.R., Laird, A.R., Kochunov, P., Davis, M.D., Glahn, D.C., Duong, T.Q., Fox, P.T., 2014. Multi-region hemispheric specialization differentiates human from nonhuman primate brain function. Brain Struct. Funct. 219, 2187–2194. doi:10.1007/s00429-013-0620-9

Wu, W., Koopmans, P.J., Frost, R., Miller, K.L., 2016a. Reducing slab boundary artifacts in three-dimensional multislab diffusion MRI using nonlinear inversion for slab profile encoding (NPEN). Magn. Reson. Med. 76, 1183–1195. doi:10.1002/mrm.26027

Wu, W., Poser, B.A., Douaud, G., Frost, R., In, M.H., Speck, O., Koopmans, P.J., Miller, K.L., 2016b. High-resolution diffusion MRI at 7T using a three-dimensional multi-slab acquisition. Neuroimage 143, 1–14. doi:10.1016/j.neuroimage.2016.08.054

Xue, R., Sawada, M., Goto, S., Hurn, P.D., Traystman, R.J., Van Zijl, P.C.M., Mori, S., 2001. Rapid three-dimensional diffusion MRI facilitates the study of acute stroke in mice. Magn. Reson. Med. 46, 183–188. doi:10.1002/mrm.1174

Yin, D., Valles, F.E., Fiandaca, M.S., Forsayeth, J., Larson, P., Starr, P., Bankiewicz, K.S., 2009. Striatal volume differences between non-human and human primates. J. Neurosci. Methods 176, 200–205. doi:10.1016/j.jneumeth.2008.08.027

Zakszewski, E., Adluru, N., Tromp, D.P.M., Kalin, N., Alexander, A.L., 2014. A diffusion-tensor-based white matter atlas for rhesus macaques. PLoS One 9. doi:10.1371/journal.pone.0107398

Zhang, H., Schneider, T., Wheeler-Kingshott, C.A., Alexander, D.C., 2012. NODDI: Practical in vivo neurite orientation dispersion and density imaging of the human brain. Neuroimage 61, 1000–1016. doi:10.1016/j.neuroimage.2012.03.072

Zhao, L., Madore, B., Panych, L.P., 2005. Reduced field-of-view MRI with two-dimensional spatially-selective RF excitation and UNFOLD. Magn. Reson. Med. 53, 1118–1125. doi:10.1002/mrm.20458

List of publications

Journal paper

***Tounekti, S**., Troalen, T., Bihan-Poudec, Y., Froesel, M., Lamberton, F., Ozenne, V., Cléry, J., Richard, N., Descoteaux, M., Ben Hamed, S., Hiba, B., 2018. High-resolution 3D diffusion tensor MRI of anesthetized rhesus macaque brain at 3T. NeuroImage 181, 149–161. doi:10.1016/J.NEUROIMAGE.2018.06.045*

*Bihan-Poudec, Y., **Tounekti, S***., et al., High-resolution artifact-free diffusion-MRI in anesthetized Rhesus macaque at 3T. In progress.*

Oral communication

***Tounekti S**, Troalen T, Bihan-Poudec Y, Froesel M, Lamberton F, Ozenne V, Richard N, Descoteaux M, Ben Hamed S, Hiba B. In-Vivo Very High-Resolution 3D Diffusion MRI of Macaque Monkey, proceeding of the 34th Annual scientific meeting ESMRMB,2017 October 19-21, Barcelona, Spain.*

Poster communications

*Bihan-Poudec Y, **Tounekti S**, Richard N, Froesel M, Lamberton F, Troalen T, Ben Hamed S, Descoteaux M, Hiba B. In-Vivo Analysis of the Superficial White Matter in the Macaque Brain Using High-resolution Diffusion MRI: preliminary results. Proceeding of the 27th congress of the ISMRM, 2018 June 16-21, Paris, France*

***Tounekti S**, Troalen T, Bihan-Poudec Y, Froesel M, Lamberton F, Ozenne V, Richard N, Descoteaux M, Ben Hamed S, Hiba B. In-Vivo Very High-Resolution 3D Diffusion MRI of Macaque Monkey, proceeding of the 34th Annual scientific meeting ESMRMB,2017 October 19-21, Barcelona, Spain.*

***Tounekti S**, Troalen T, Bihan-Poudec Y, Froesel M, Lamberton F, Ozenne V, Richard N, Descoteaux M, Ben Hamed S, Hiba B. In-Vivo Very High-Resolution 3D Diffusion MRI of Macaque Monkey, pro. of the 3rd congress of the SFRMBM, 2017 Mars 13-15, Bordeaux, France.*

Curriculum vitae

Slimane Tounekti
147 A rue Jean Voillot
69100, Villeurbanne, France
Phone: +337 51 58 27 31
E-mail: slimentounekti88@gmail.com

Education

05/2015 – 01/2019: PhD in Sciences & Health Engineering: NMR Physics and Medical Imaging
Development of high spatial resolution acquisition methods for diffusion MRI (dMRI). Institut des sciences cognitives - Marc Jeannerod (ISCMJ –CNRS), University of Claud Bernard Lyon 1, in collaboration with SIEMENS Healthineers, France

09/2013 – 09/2014: **Research Master's degree in Medical Imaging and Biomedical engineering.**
University of Claud Bernard Lyon 1, Polytech Lyon.

09/2011 – 07/2013: **Professional Master's degree in Biomedical Engineering.**
University of Tunis EL Manar, Higher Institute of Medical Technology.

09/2008 - 07/2011: **License degree in Biomedical Engineering**
University of Tunis EL Manar, Higher Institute of Medical Technology.

Skills

-
- Biomedical engineering and medical imaging physics.
- MR physics and pulse sequence design and implementation: SIEMENS environment :IDEA
  - (EPI-based pulse sequence, DW imaging, parallel imaging (Grappa), echo-navigator)
- Image /MRI data reconstruction (Gadgetron) and Post-processing.
- Neuro-imaging: MR imaging (DTI, fMRI), human and non-human application.
- Computer Science: C, C++, Matlab, Windows, Linux.

Publications

Tounekti, S*., Troalen, T., Bihan-Poudec, Y., Froesel, M., Lamberton, F., Ozenne, V., Cléry, J., Richard, N., Descoteaux, M., Ben Hamed, S., Hiba, B., 2018. High-resolution 3D diffusion tensor MRI of anesthetized rhesus macaque brain at 3T. NeuroImage 181, 149–161. doi:10.1016/J.NEUROIMAGE.2018.06.045*

International *Conferences & workshops*

- *Bihan-Poudec Y,* ***Tounekti S****, Richard N, Froesel M, Lamberton F, Troalen T, Ben Hamed S, Descoteaux M, Hiba B. In-Vivo Analysis of the Superficial White Matter in the Macaque Brain Using High-resolution Diffusion MRI: preliminary results. Poster session, proceeding of the 27th congress of the ISMRM, 2018 June 16-21, Paris, France*
  -

- ***Tounekti S**, Troalen T, Bihan-Poudec Y, Froesel M, Lamberton F, Ozenne V, Richard N, Descoteaux M, Ben Hamed S, Hiba B. In-Vivo Very High-Resolution 3D Diffusion MRI of Macaque Monkey, Oral presentation and e-poster at Diffusion MRI session, proceeding of the 34th Annual scientific meeting ESMRMB,2017 October 19-21, Barcelona, Spain.*
-
- ***Tounekti S**, Troalen T, Bihan-Poudec Y, Froesel M, Lamberton F, Ozenne V, Richard N, Descoteaux M, Ben Hamed S, Hiba B. In-Vivo Very High-Resolution 3D Diffusion MRI of Macaque Monkey, Poster session, proceeding of the 3rd congress of the SFRMBM, 2017 Mars 13-15, Bordeaux, France.*

Internship

04/2015 – 05/2015: *Institut des sciences cognitives- Marc Jeannerod, France (1 month).*
04/2014 – 09/2014: *I3MTO-University of Orleans, France (6 months).*
02/2013 - 07/2013: *Department of nuclear medicine at the national institute of cancerology, Tunisia (6 months).*
02/2011 – 06/2011: *Laboratory of quality control and Technical device: CETIME, Tunis, Tunisia (6 months).*